CHANNEL STATE INFORMATION ACQUISITION FOR ADAPTIVE UNDERWATER ACOUSTIC NETWORKING

by

Hossein Ghannadrezaii

Submitted in partial fulfillment of the requirements
for the degree of Doctor of Philosophy

at

Dalhousie University
Halifax, Nova Scotia
September 2022

To my wife, Najmeh, My parents, and my brother.

Table of Contents

List of Tables

List of Figures

Abstract

This dissertation investigates the design aspects of an adaptive cross-layer architecture to optimize the energy efficiency, the spectral efficiency, and the reliability of underwater acoustic multihop relaying networks by utilizing channel state information (CSI). Specifically, an energy efficient channel-aware routing protocol for reliably relaying data packets, as well as a media access control to maximize the network throughput and maintain connectivity are described. These tasks are approached by predicting CSI using a novel data-driven probabilistic model. As the main contribution, a CSI acquisition approach based on a Markov chain process is proposed that exploits information from the physical environmental conditions, including the tide phase and flow, to improve the accuracy of channel characteristics predictions. Specifically, the method is intended to obtain the channel characteristics, including the gain, delay, Doppler spread, as well as the standard deviation of intrapaths delays in time varying conditions. The correlation between different oceanic processes and the acoustic channel characteristics is investigated to define a set of tide-dependent states corresponding to a particular channel condition. To analyze the impact of flow and surface elevation variations, channel soundings from a 34-day sea trial conducted in Grand Passage, Nova Scotia, are applied to a parametric model of the propagation channel. The probabilistic parametric model forms a data set by characterizing the time varying channel impulse response and by describing the channel tapped-delay structure statistically as a function of the tide phase. The proposed Markov chain is driven by the measured channel data set and predicts the future channel characteristics one tide cycle ahead.

Finally, predicted small-scale statistics are incorporated into an analytical channel model to estimate channel impulse responses in a mobile scenario.

To validate the accuracy of the proposed method, the predicted channel characteristics are compared to the channel measurements obtained in a 566 meters channel in Grand Passage, Nova Scotia, from September 22, 2018, to October 25, 2018.

List of Abbreviations Used

AES	Advanced Encryption Standard
AN	Acoustic Node
AUV	Autonomous Underwater Vehicles
BEB	Binary Exponential Backoff
BER	Bit Error Rate
CTS	Clear to Send
CA	Collision Avoidance
CS	Carrier Sensing
CCC	Common Control Channel
CDMA	Code Division Multiple Access
CIR	Channel Impulse Responses
CP	Cyclic Prefix
CRC	Cyclic Redundancy Check
CSI	Channel State Information
CSMA-CA	Carrier-sense Multiple Access with Collision Avoidance
DIFS	DCF Interframe Spacing
DSP	Digital Signal Processors
ECDH	Elliptic-curve Diffie–Hellman
ECDLP	Elliptic Curve Discrete Logarithm Problem
FAMA	Floor Acquisition Multiple Access
FDMA	Frequency Division Multiple Access
FFT	Fast Fourier transform
FH-BFSK	Frequency-hopping Binary Frequency Shift Keying
FPGA	Field Programmable Gate Array
GA	Global Awareness
HCHF	High Coverage and High Fairness
ICI	Inter-carrier Interference

IFFT	Inverse Fast Fourier Transform
IoUT	Internet of Underwater Things
ISI	Inter symbol Interference
LAC	List of Available Channels
LCCT	List of Confirmed Channels for Transmission
LDRA	Link Degree and Round Based Algorithm
LT-MAC	Location-based TDMA MAC
MAC	Media Access Control
MACA	Multiple Access with Collision Avoidance
NIST	National Institute of Standards and Technology
OFDM	Orthogonal Frequency Division Multiplexing
OFDMA	Orthogonal Frequency-division Multiple Access
PDR	Packet Delivery Ratio
RMS	Root Mean Square
RTS	Ready to Send
RX	Receiver
SSB	Single-sideband
SSP	Sound Speed Profile
TDA-MAC	Transmit Delay Allocation MAC
TDMA	Time Division Multiple Access
TX	Transmitter
UWA	Underwater Acoustic
UWAC	Underwater Acoustic Channel
UWAN	Underwater Acoustic Network
UWG	Underwater Gateways
WA-TDMA	Wave-like Amendment-based TDMA

Acknowledgements

First, I would like to thank my supervisor, Dr. Jean-François Bousquet, for giving me the opportunity to have a journey through my doctoral research program. His continuous help and support allow me to explore a challenging engineering problem with confidence and courage.

I would also thank other members of my supervisory committee, Dr. Jacek Ilow, Dr. David Barclay, for their helpful and constructive comments and contributions on my thesis work. I am also thankful to Dr. Jose Gonzalez-Cueto and James Craig for their supports and advices during my PhD studies and for their great personalities. I am thankful to all the officemates Alireza Karami, Navid Eskandary, Adib Shahabi, Xiao Liu, Afolarine Egbewande and Surinder Singh who shared many insights with me. Thanks also go to other graduate students in UW-Stream lab and in our department.

I'm also thankful to the electrical and computer engineering department administration, especially Nicole Smith for all their supports and help.

Finally, I would like to thank my family for being my backbone specially my wife Najmeh for all the love and support they have provided.

Chapter 1

Introduction

The deep ocean is largely unexplored and is often considered the last frontier on Earth. Deploying underwater acoustic networks (UWANs) has been studied to enable data collection from remote sensors in deep oceans and to facilitate a wide range of underwater sensing and monitoring applications in commercial, scientific, and military sectors.

UWANs can support various offshore industries: in the oil and gas and aquaculture sectors, UWANs can enable exploration, instrument monitoring, pipeline inspection, pollution control, and climate recording. Additionally, acoustic sensors can be deployed in remote ocean areas to monitor subsea activity, such as the presence of vessels, marine life, debris, or seismic activity. To provide more flexibility to the networks, Autonomous Underwater Vehicles (AUVs) can be used to enable dynamically changing networks and offer the ability to perform large-area surveillance using mobile platforms.

The feasibility of most of the above applications requires UWANs to meet certain levels of reliability as well as spectral and energy efficiency. However, UWANs present many challenges from a communications point of view due to the temporal variations of channel characteristics including channels gain, delay and Doppler spread. In an UWAN, the acoustic nodes' (ANs') routing layer, media access control (MAC), and physical layer parameters need to be designed and adapted with respect to time varying channels conditions. The performance of an adaptive network depends on the accurate channel state prediction and reconfiguration capability of the communication stack.

This chapter is organized as follows. Next, in Section 1.1, key challenges and the state-of-art in UWANs will be presented; then, in Section 1.2, the optimization aspects of UWANs using channel adaptation is addressed, and the role of CSI acquisition in adaptation is explained; in Section 1.3, the main contributions of this study

in enabling adaptive UWANs using a practical channel state information (CSI) acquisition scheme is introduced, then, in Section 1.4, the organization of this dissertation is presented.

1.1 Background

To enable underwater communication, acoustic propagation is generally adopted because low-frequency sound can easily travel several kilometers. Modern underwater communication technology was developed during the Second World War for military purposes. One of the first underwater communication systems was the underwater telephone, developed in 1945 in the United States for communicating with submarines [1]. This device used a single-sideband (SSB) suppressed carrier amplitude modulation in the 8 kHz to 11 kHz frequency range and was capable of sending acoustic signals over several kilometers. The availability of compact digital signal processors (DSPs) during the past two decades advanced the development of underwater acoustic communication systems and enabled many modulation methods and techniques developed for radio communications to be adopted for underwater acoustic communications systems [2, 3, 4].

Acoustic waves are not the only means of underwater communication but are the best-known form of long-distance communication in underwater. The high attenuation of radio frequency (RF), optical, and magneto-inductive (MI) signals in seawater leaves acoustic propagation as the only feasible option to transmit underwater signals over distances in excess of one hundred meters. Table 1.1 compares different means of underwater communication.

The acoustic link is cheaper and more practical than cabled or tethered links. However, the acoustic channel features time varying multipath fading, frequency-dependent transmission loss, and high propagation delay, which make it a challenging medium for communication [5].

Multipath arrival greatly affects the acoustic signal as it propagates through the water. By definition, in a multipath channel, signals received at a receiver are the superposition of multiple acoustic waves from different paths. Each path arrives with a unique amplitude, phase, and angle of arrival. For example, Figure 1.1 shows a representation of the rays that combine at the receiver in a shallow environment;

Table 1.1: Comparison of underwater MI, EM, acoustic, and optical communications [3]

Communication mean	Propagation speed	Data rates	Communication ranges	Channel dependency
MI	3×10^7 m/s	$\sim$ Mb/s	10−100 m	Conductivity
RF	3×10^7 m/s	$\sim$ Mb/s	$\leq$ 10 m	Conductivity, multipath
Acoustic	1500 m/s	$\sim$ kb/s	$\sim$ km	Multipath, Doppler, temperature, pressure, salinity, environmental conditions
Optical	3×10^7 m/s	$\sim$ Mb/s	10−100 m	Light scattering, line of sight communication, ambient light noise

when the signal arrives at the receiver by two or more different paths, and when at least one path's length is changing, the non-coherent combination multipaths results in a frequency selective fading channel [6]. Partial cancellation of the signal by itself is formed by frequency-selective fading channel [7].

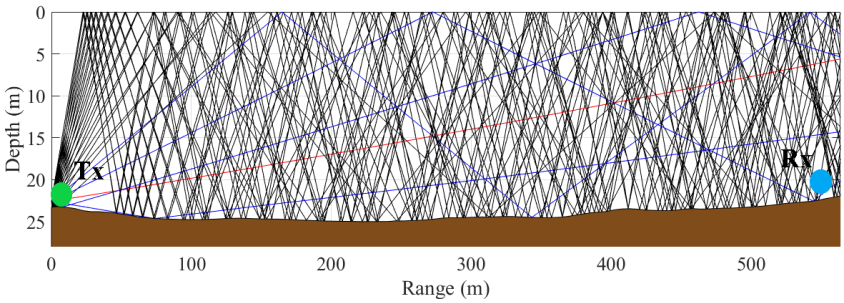

Figure 1.1: Simulation of a 566-meter channel ray traces by Bellhop for a deployment in the Bay of Fundy, Nova Scotia.

The acoustic channel is also subject to time-variance. The time varying fading effect in an acoustic channel can be categorized in two different time scales: large-scale and small-scale fading effects [8].

Large-scale effects are assumed to be slow, long-term trends that impact the locally averaged received signal power, causing it to vary over extended periods ranging from several minutes to hours [9]. Channel variations caused by large-scale phenomena are influenced by changes in sound speed profile, drifting of the transmitter or receiver,

changes in water temperature, and in sea level due to tides [10]. In contrast, we refer to rapid fluctuations of the received signal strength over a very short period of time in the order of a few symbols duration or travel distances in the order of a few wavelengths as a small-scale effect [11]. Small-scale effects are mainly induced by reflection, scattering and motion-induced Doppler shifts of acoustic waves at the surface, bottom, and any surrounding objects. Both multipath propagation, as well as refraction, produce time dispersion in the received signal. This phenomenon also combines with strong physical environmental conditions such as flow and tide which cause significant channel variations.

Figure 1.2 shows a stochastic model of a time varying channel developed in [12], which captures the effect of physical environment variations including tides on channel gain.

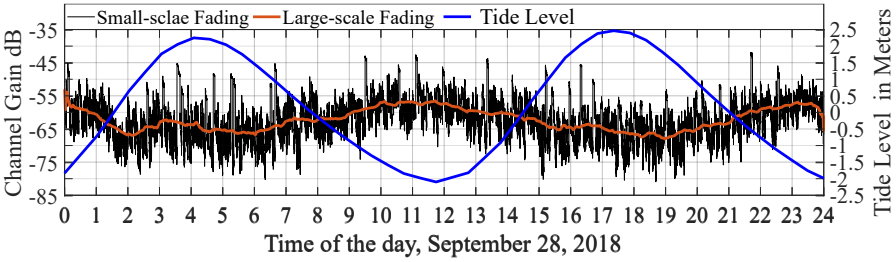

Figure 1.2: Stochastic modelling of Small-scale and Large-scale fading [12].

In addition to challenges imposed by large-scale and small-scale effects, an underwater acoustic channel (UWAC) is severely bandwidth limited due to its frequency-dependent transmission loss. Frequency-dependent transmission loss is primarily due to viscosity and the relaxation of $B(OH)_3$ and $MgSO_4$ present in seawater and imposes significant constraints on the achievable throughput of UWANs [13]. Furthermore, propagation delay in UWACs introduces unique problems in channel access management in multi-user UWANs. Sound propagates underwater at a very low speed of approximately 1500 m/s, when compared to RF in terrestrial communication networks. Because of the properties of the underwater acoustic channel, available networks protocols in terrestrial wireless networks are not fit for UWANs.

With the increased interest in deploying underwater infrastructure, UWANs attracted a lot of attention. UWANs are constituted heterogeneous sensors, including

fixed nodes, AUVs, sink nodes, or surface gateways to collect data for various applications [14]

Many network strategies have been studied for UWANs in recent years. A representative deployment for the UWAN [15] is depicted in Figure. 1.3; it consists of acoustic nodes (ANs) as well as cluster heads that also act as underwater gateways (UWGs). The UWGs relay the underwater sensor data to the surface buoys. Surface buoys are also equipped with a long-range radio or satellite transceiver to communicate with an onshore sink or a surface sink.

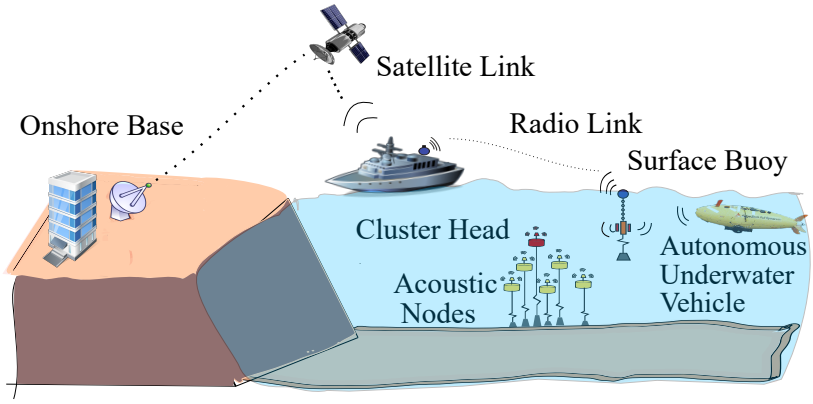

Figure 1.3: Representation of a reference single-hop UWAN architecture [15].

Due to the unique characteristics of acoustic channels, designing reliable and efficient networking protocols, e.g., medium access control (MAC) and routing protocols for UWANs have their unique challenges compared to terrestrial networks.

Some of the major challenges in the design of UWANs are [4]:

- The available bandwidth is severely limited which constrains the exchange of network management packets.

- The underwater channel is severely impaired, especially due to multipath and fading which increases packet loss and re-transmission requests.

- Propagation delay in underwater is five orders of magnitude higher than in radio frequency(RF) terrestrial channels, and extremely variable [16]. High propagation delay increases the channel access waiting time and significantly increases latency.

- High bit error rate (BER) and temporary losses of connectivity (shadow zones) between nodes can be experienced, due to the extreme characteristics of the underwater channel.

- Battery power is limited and usually batteries cannot be recharged. Limited battery magnifies the importance of energy efficient network protocols.

An adaptive communication stack can optimize the reliability, the spectral efficiency and the energy efficiency of UWANs [17] by reconfiguring parameters including the modulation level, the sub-carriers bandwidth, the transmit power, the guard band duration, etc. according to the channel conditions. Adaptability requires precise channel state information (CSI) including channel gain, delay, Doppler spread and multipath structure at the transmitter. Precise CSI acquisition plays an important role in enabling adaptability and improving UWANs' efficiency.

1.2 Problem Statement

The deployment of underwater networks (UWAN) has been attracting significant interest to develop remote underwater sensing and monitoring technologies. Underwater acoustic propagation offers an opportune medium for subsea communication over kilometers.

Specifically, recent coastal development and the use of AUVs in shallow water, where the typical depth is about 10–100 meters, provide new opportunities in various industrial and military sectors. The shallow ocean is an exceedingly complicated place, and temporal channel variations impact the reliability and spectral efficiency of underwater acoustic (UWA) networks. Temporal variations of underwater acoustic channels introduce significant challenges for reliable transmission, channel access control, collision avoidance, and routing in the deployment of UWANs in shallow waters.

The time varying physical oceanographic processes induce amplitude and delay variations in the propagation channel and motion (including surface variations and secondary effects from flow) introduce additional random Doppler frequency shifts. Conventional approaches for reliable underwater communication in time varying fading channels consider the worst-case channel condition to define the physical and

MAC layer parameters leading to inefficient use of spectrum resources and high energy consumption.

The time constants that govern the channel characteristics depend on the underlying physical phenomena. To predict the channel characteristics reliably, it is important to gather information about the time varying physical environmental conditions that influence the channel statistics. The physical environmental factors that govern the UWA channel variations can be categorized in three classes: 1) *a priori* known deterministic physical and geometric conditions including channel depth, range, and bathymetry; 2) slow varying conditions that can be measured in real-time and which are caused by changes in, e.g., sound speed profile, as seasonal water temperate changes, drifting of the transmitter or receiver, as well as changes in sea level due to tides; and 3) random varying oceanic processes such as, surface roughness, random ocean turbulence as well as scattering. These effects can be represented statistically using a small-scale channel model [10].

Knowledge of the physical environment and acoustic channel fading characteristics can be used to adapt physical and MAC layers to channel variations and optimize the spectral and energy efficiency of UWA systems [17]. Specifically, in shallow conditions, the channel characteristics can vary significantly with the tide and flow, emphasizing using a context-aware prediction scheme.

To deploy multiuser networks, channel access and a routing protocol must be defined to meet the UWA channel conditions and communications requirements.

The general aim of this research work is studying design aspects of a cross-layer approach in which UWANs dynamically adapt their communication stack with the time varying characteristics of the channel [18]. Accurate predictions of channel state information (CSI) at the transmitter are crucial to design a cross-layer acoustic communication system.

To enable an adaptive underwater network, three main objectives are defined in this work:

1. Define and demonstrate through simulation a routing algorithm to extend the range of the network with minimal energy consumption.

2. Define and demonstrate through simulation a protocol to allow spectrally efficient sharing of the resources in a network.

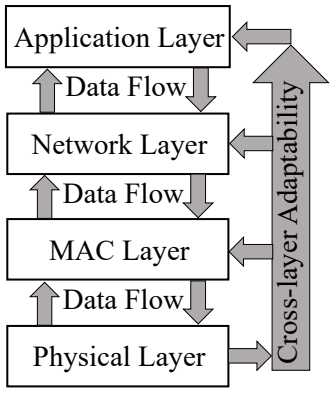

Figure 1.4: Cross-layer Architecture.

3. Define an algorithm to predict in real-time the channel characteristics between the nodes given a scarce set of measurements, and a priori known environmental conditions.

1.3 Contributions

Three major contributions are highlighted in this thesis.

As a first contribution, a network architecture is proposed for UWANs in Chapter 3. Here, an energy-efficient flooding routing protocol is defined in Section 3.2.1 for exchanging network control messages, and a channel-aware multihop relaying routing is introduced for data transmission in Section 3.2.2. Next, to maximize resource allocations and ensure connectivity between the relays, a channel-aware MAC layer is proposed to share the acoustic resources while avoiding collisions within the network. The proposed channel-aware routing protocols optimize reliability and energy efficiency, and the proposed MAC scheme maximizes channel utilization and ensures connectivity in the UWAN framework. The work described in Chapter 3 contains material presented at the following conferences and published in the Computer and Telecommunications Networking Journal by Elsevier:

- H. Ghannadrezaii, J-F Bousquet, "Maximizing Network Coverage in a Multichannel Short-range Underwater Acoustic Sensor Network", Computer Networks, Volume 160, 4 September 2019, Pages 1-10.

- H. Ghannadrezaii, J-F Bousquet, "FHSS-BFSK Janus-Based protocol for Underwater Hybrid Cellular-Ad hoc Network", "2018 CMOS Congress", 10-14 Jun 2018, Halifax, Canada.

- H. Ghannadrezaii, J-F Bousquet, "Securing Janus-Based Flooding Routing Protocol for Underwater Acoustic Networks", "OCEAN 2018", October 22 – 25, 2018, Charleston, USA.

The second contribution of this study is to provide an accurate modeling solution for CSI in an environment with strong tidal currents. The proposed statistical data analysis from a sea trial in Grand Passage implies that the complex random surface process induced by the physical environmental conditions governs the fast-changing channel characteristic. Our proposed CSI acquisition model takes into account the tide level to identify different channel states. Specifically, in each state, the channel is characterized statistically using key parameters, including gain, delay, Doppler spread, and variance of intrapath delays. Considering different states for the channel optimizes prediction accuracy and reduces model error.

Toward this goal, first, the role of the intrapaths statistics on the channel characteristics is reviewed. Then, the impact of surface elevation variations on the path statistics is identified. A data set from experimental data, including the large data set obtained over a 34-day sea trial channel-sounding data set, is compressed to generate a parametric model of the channel. For this purpose, real channel estimations extracted from a set of probing sequences are used.

The work described in Chapter 4 contains material presented at the following conferences and is under review in the IEEE Journal of Oceanic Engineering:

- J. MacDonald, H. Ghannadrezaii, JF. Bousquet, D. Barclay "Analysis of the Impact of Flow on the Underwater Acoustic Channel", Oceans 2021.

- H. Ghannadrezaii, J-F Bousquet, "Channel Quality Prediction for Adaptive Underwater Acoustic Communication", Ucomms 2020, Lerici, Italy, September 2020.

- H. Ghannadrezaii, J-F Bousquet, "Cross-layer Design for Software-defined Underwater Acoustic Networking", "OCEANS 2019", Marseille, France.

As a third contribution, a novel multi-layer Markov process is used to predict the channel characteristics in different tide phases. Each layer of the proposed Markov chain predicts the channel gain, delay, Doppler spread, and intrapaths statistics in one tide phase. Compared to other proposed models, the significance of this model is context awareness, which takes into account the tide phase and considers 25 different phases for the channel during 24 hours. By tracking the deterministic physical environmental conditions to define different phases, the prediction model has achieved significant accuracy. The predicted small-scale statistics will be incorporated into a large-scale analytical model to find the channel state information (CSI) at least one travel time ahead of transmission.

To validate the accuracy of the proposed method, the predicted channel characteristics are compared to the channel measurements obtained in a 566 meters channel in Grand Passage, Nova Scotia.

Finally, a methodology to estimate the CSI for a mobile AUV is presented. Here, a channel tracking model is developed, which incorporates data-driven small-scale statistics into an analytical channel model to estimate the channel impulse responses (CIRs). The communication performance of the estimated channel is evaluated for 24 hours for an OFDM link between a fixed node and a mobile AUV node. The BER performance of the acoustic link is demonstrated in different signal-to-noise ratios.

The work described in Chapter 5 contains materials that is currently under internal review for the following publication:

- H. Ghannadrezaii, J-F Bousquet "Channel State Information Acquisition for Adaptive Underwater Acoustic Communication", IEEE Journal of Oceanic Engineering, May 2022.

- H. Ghannadrezaii, J-F Bousquet, "Performance Evaluation of Acoustic Link in High flow Tidal Environment ", Computer Networks, September 2022.

1.4 Outline of Dissertation

This dissertation is organized as follows. In Chapter 2, a detailed review of key aspects of UWAN is provided. Then in Chapter 3, a Media Access Control (MAC) protocol and a channel-aware multihop relaying routing protocol are proposed to

optimize reliability and energy efficiency in UWANs. The proposed MAC protocol ensures that ANs within the transmitting range of each other do not utilize the same frequency channels and are allocated at least one channel to maintain network connectivity. In Chapter 4 the impact of specific physical environment processes on a statistical channel model is presented, and a parametric data-driven model is used to statistically characterize the channel power delay profile in different tide phases. In Chapter 5, a Markov process is presented that predicts the channel characteristics in future tide phases. Here a channel simulator is presented that estimates the CIRs for a mobile AUV by incorporating the small-scale channel statistics; finally, in Chapter 6, conclusions are presented.

Chapter 2

An Adaptive Cross-Layer Design for Underwater Acoustic Networking

Over the past decade, new adaptive wireless technologies such as Software Defined Networks [19] and Adaptive 5G [20, 21] have been successfully utilized and have improved the spectral and energy efficiency of terrestrial networks. However, challenges in UWAC, inlcuding the time varying frequency selective fading and the frequency dependant transmission loss has thwarted the widescale development of UWANs. Indeed, conventional UWANs remain spectrally inefficient with low reliability and high energy consumption [22, 23]. The temporal variation of the underwater acoustic channel emphasizes the importance of adaptive underwater communication stacks. Particularly, the lower layers, including the physical layer, the MAC layer and the routing layer should be adaptable to the time varying channel conditions [17].

Various physical, routing and media access control schemes for UWANs have been proposed for over a decade now [24, 25, 26]. Among all the solutions, cross layer designs that can exploit the channel information [27] received the most attention.

In this chapter, first in Section 2.1, my proposed cross-layer design is described; then, in Section 2.2, an acoustic channel transfer function will be reviewed and the CSI parameters of interest will be described; in Section 2.3, key modulation techniques to enable reliable transmission underwater are presented, and the role of CSI to optimize the physical layer is shown; then in Section 2.4 the current state-of-the-art in channel aware MAC for will be presented and the existing network architectures to enable multihop relaying will be reviewed; finally in Section 2.5, Janus protocol to enable interoperability among different nodes are briefly reviewed.

2.1 Cross-layer Service Optimization

Cross-layer design is defined by exchanging information between layers for optimum use of network resources and achieving high adaptability. In cross-layer design, each

layer is characterized by a few key input variables and control settings. The input variables are passed to other layers to determine the best adaptation rules for their control settings with regard to the current network and channel status [28]. Cross-layer design is usually formulated as an optimization problem, with optimization variables and constraints from multiple layers. Solving the optimization problem provides the optimal values for the control settings in the layers.

Cross-layer approaches to optimize power consumption and spectral efficiency have been discussed in recent years [29, 30].

In this work, a cross-layer service, as shown in Figure 2.1 is considered to optimize each layer. The finite state design approach to re-configurable parameters in each layer enables each layer to change from one state to another in response to a channel state and reduce the cross-layer service computation complexity to a lookup table. However, the set of configurable variable states should be derived and defined concerning the application's objective function and channel states.

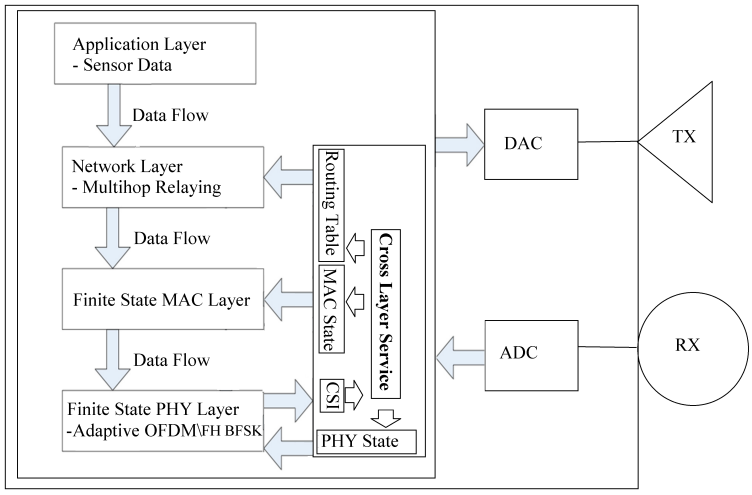

Figure 2.1: Cross-layer Service re-configures layers dynamically using acquired CSI and preset states according to user application.

The cross-layer service optimization consists of three elements: an objective function, a set of configurable variables, and a set of constraints. They are defined as follows:

1. The **objective function** is defined to maximize the bit rate or to minimize the energy per bit consumption while maintaining a target BER. The objective

function is defined according to the communication link requirement. Depending on the network application, maximization of the bit rate can outweigh the minimization of the energy per bit consumption or vice versa. A trade-off is defined based on the network application. In this work, two use cases are defined:

(a) Data collection sensor networks that can be applied in the oil and gas industry, for ocean pollution monitoring and for aquaculture; this application requires to maintain a modest transmission bit rate and is defined to minimize the overall energy consumption per bit for a target BER to increase battery usage.

(b) High throughput data streaming communication like voice or video transmission application need relatively high end-to-end bit rate, without constraint on energy efficiency.

2. The **set of constraints** are imposed by the time varying channel conditions and by the equipment capabilities. The channel conditions impose a set of constraints, for example, the channel's delay spread, gain, and Doppler spread. Additionally, constraints imposed by equipment are defined based on the manufacturer operating frequency and bandwidth, maximum transmit power, hydrophone sensitivity and battery life.

3. The **set of configurable variables** in the physical, MAC layer and routing layer that are updated according to the constraints to optimize the objective function.

   The OFDM physical layer's design parameters include sub-carrier bandwidth, number of subcarriers, inverse fast Fourier transform (IFFT)/fast Fourier transform (FFT) block size, CP size, symbol rate, symbol duration, modulation level, code rate, guard interval, and transmitting power. To satisfy the channel constraints to have a reliable transmission for example in OFDM systems, the cyclic prefix (CP) length needs to be larger than the maximum excess delay of the channel. As defined in [31], maximum excess delay, is the relative time difference between the first signal component arriving at the receiver to the last component whose power level is above some threshold. If this information is

not available, the worst-case channel condition is used for system design, which makes the CP a significant portion of the transmitted data. One way to increase the spectral efficiency is to adapt the length of the CP to the changing multipath conditions, which requires channel excess delay knowledge [32].

In multihop UWANs, the physical layer, the MAC protocol, and the relaying design schemes can influence the network throughput and energy efficiency.

Channel conditions which the CSI represents, play the main role in defining constraints. Following, we will review UWAC time varying characteristics.

2.2 Acoustic Communication Channel Model and Properties

In this section, we review underwater acoustic channel and characterize CSI. Firstly, the channel transfer function will be represented and then the frequency and time dispersion will be characterized, secondly, the impact of time-variance on channel properties including channel gain, delay spread, Doppler spread and coherence bandwidth will be described.

Acoustic Channel Transfer Function

The UWAC is characterized by a transmission loss that mainly depends on absorption, distance, signal frequency, temperature and pressure [33].

One of the widely used model for absorption is the Thorp's formula described in [34] and is expressed as

$$\alpha(f) = A_1 P_1 \frac{f_1 f^2}{{f_1}^2 + f^2} + A_2 P_2 \frac{A_2}{P_2} \frac{f_2 f^2}{{f_2}^2 f^2} + A_3 P_3 f^3 \quad \text{dB/km} \tag{2.1}$$

where $\alpha(f)$ is the absorption as a function of frequency and f is the signal frequency in kHz. The coefficients A_1 to A_3 and P_1 to P_3 represent the effects of water temperature and pressure respectively and f_1 and f_2 are the relaxation frequencies of boric acid and magnesium.

Transmission loss increases with range and frequency, limiting the useful bandwidth. Bandwidth limitation and spectral efficiency is a considerable limitation on design of UWAN and determines the range and data-rate of an acoustic link.

The sound speed, c, is another decisive parameter in acoustic propagation which is a function of temperature, salinity, and pressure. In seawater it ranges between 1450 m/s and 1570 m/s [35]. We can calculate the speed of UWA waves (denoted by c) empirically as

$$\begin{aligned} c = 1448.96 + 4.591T - 5.304 \times 10^{-2}T^2 + 2.374 \times 10^{-4}T^3 + 1.340(S-35) \\ + 1.630 \times 10^{-2}z + 1.675 \times 10^{-7}z^2 - 1.025 \times 10^{-2}T(S-35) - 7.139 \times 10^{-13}Tz^3 \ \text{ m/s} \end{aligned} \tag{2.2}$$

where T, S, and z denote the temperature in Celsius, the salinity in parts per thousand, and the depth in meters, respectively [36].

The sound speed profile (SSP) shown in Figure 2.2 is a representative SSP measured throughout the experiments on the South shore of Nova Scotia during the DalComms1 sea trial in July 2017. This result shows the variability in the SSP as a function of depth [37]. Generally, the largest sound speed variations happen near the surface, where the daily heating and cooling, precipitation, and the wind affect the mixed layer temperature, salinity, and depth [34]. In a shallow water environment, a large portion of the water column may be affected by the SSP variations, increasing the complexity of the time varying channel model.

The transfer function of a time varying channel between the transmitter and receiver at a particular discrete-time realization $t \in T_n$ can be described by [6]

$$H(f,t) = \sum_p h_p(t)\tilde{\gamma}_p(f,t)e^{-j2\pi f\tau_p(t)}, \tag{2.3}$$

where $h_p(t)$ is the large-scale gain, $\tau_p(t)$ is the large-scale delay and $\gamma_p(f,t)$ is the overall small-scale fading coefficient of path p. The time varying large-scale gain of path p is defined as

$$h_p(t) = \bar{h}_P \frac{1}{\sqrt{(1+\frac{\Delta l_p(t)}{\bar{l}_p})^k \alpha_p(f)^{\Delta l_p(t)}}}, \tag{2.4}$$

where in (2.4) , $\bar{h}_p$ is the nominal path gain and $\Delta l_p(t) = l_p(t) - \bar{l}_p$ describes the variations of the path length in unit of meter. Accordingly, $l_p(t)$ is the large-scale path length and $\bar{l}_p$ represents the nominal path length, $\alpha_p(f)$ is the absorption loss

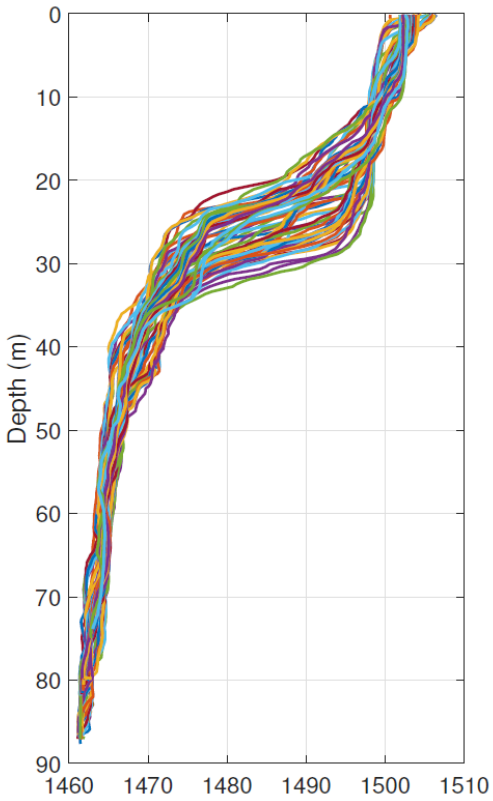

Figure 2.2: 70 SSP measured throughout the experiments in the south shore of Nova Scotia during the DalComms1 sea trial between 26-28 July 2017 [37].

coefficient for path p within the signal frequency which can be obtained in dB/km using Thorp's empirical formula, and k is the spreading factor [38, 36].

The large-scale delay of path p, $\tau_p(t)$, in the channel realization $t \in [0, T]$ can be modelled as

$$\tau_p(t) = \bar{\tau_p} - \int_{x=0}^{t} a_{vp}(x)dx, \tag{2.5}$$

where $\bar{\tau_p}$ is the nominal delay of path p and an additional term $\int_{x=0}^{t} a_v(x)dx$ describes the overall vehicular or drifting motion at the time of the observation [5].

The system motion modelled by a linear Doppler scaling factor $a_v(t)$ [13] corresponds to the linear path length variation with equivalent speed v_{dp} longitudinal to the propagation path. The linear Doppler scaling factor is defined as

$$a_{vp}(t) = \frac{v_{dp}(t)}{\bar{c}_p}. \tag{2.6}$$

Here, $\bar{c}_p$ is the average speed that is experienced by acoustic waves in path p. As acoustic waves travel in different water depth and temperature layers, it experiences different speeds, and waves of sound always bend toward the region of lower propagation speed, obeying Snell's law.

For a scenario involving a mobile transmitter or receiver, the relative speed v_{dp} associated to the path p can be defined as

$$v_{dp} = v_{td}\cos(\theta_p - \theta_{td}) - v_{rd}\cos(\theta_p + \theta_{rd}). \tag{2.7}$$

Note that v_{td} is the transmitter vehicular speed in the direction of θ_{td} with respect to the horizontal point toward the receiver, and v_{rd} is the receivers vehicular speed in the direction of θ_{rd} with respect to the horizontal point toward the transmitter. Also, θ_P is the grazing angle associated with the p^{th} propagation path [6].

Parameters in the commonly used Equation (2.3) have been categorized into three types; nominal channel parameters, large-scale parameters, and small scale parameters.

The nominal path length $\bar{l}_p$ can be calculated using a ray-tracing algorithm such as Bellhop [34]. The slow varying large-scale parameters focus on characterizing channel variations that are influenced by changes in sound speed profile, drifting of transmitter/ receiver, changes in water temperature, and sea level, e.g., due to tides or currents. Correspondingly, the fast varying small-scale parameters focus on statistical characterization of random effects such as scattering, refraction, and motion/ flow-induced Doppler that influence the instantaneous channel response [16].

While nominal and large-scale channel models can provide useful channel state information for adaptive power control applications, they do not offer accurate CSI estimates to mitigate frequency selective fading. Random small-scale effects, including random scattering and motion/ displacement induced Doppler, are the key factors responsible for fast variations of the channel frequency response during a communication transaction.

Following the small-scale fading coefficient will be characterized and the correlation between intra-paths statistics and small-scale fading properties will be explained.

Small-scale Fading Characterisation

Small-scale effect including scattering and motion-induced Doppler shifting are the key factors which are responsible for fast variations of the channel frequency response during a communication transaction.

For each path p at a time realization of t, $\tilde{\gamma}_p(f,t)$ is the overall path small-scale fading coefficient that can be modelled by

$$\tilde{\gamma}_p(f,t) = \gamma_p(f,t)e^{j2\pi a_p f t}, \tag{2.8}$$

where $\gamma_p(f,t)$ is small-scale path coefficient and a_p is the overall Doppler scaling factor for path p which captures the relative motion between the transmitter and the receiver.

Three types of motion influence the Doppler factor: 1) unintentional transmitter/receiver motion, i.e., drifting, which induces a_{dp} a drifting Doppler scaling factor; 2) intentional transmitter/receiver motion, i.e., vehicular motion, which induces vehicular Doppler scaling factor a_v ; and 3) waves, i.e., surface motion, which induces surface Doppler scaling factor a_{sp} as expressed in [6].

A channel path can be assumed as a bundle of intra paths and according to the ray theory the transmitted signal in the path can be assumed as a cluster of rays [39], where $h_{p,i}$ are intra paths or micropaths small-scale gains and $\tau_{p,i} = \tau_p + \delta_{\tau_{p,i}}$ are the intra-paths small scale delays. The intrapaths delays are random variables with distribution of $\delta\tau_{p,i}$ which accounts for the random placement of scattering points within scattering fields in the surface, bottom or any other object in the propagation path.

Accordingly, the small-scale fading coefficient of path p can be expressed as

$$\gamma_p(f) = \gamma_{p,0} + \sum_{i\geq 1} \gamma_{p,i} e^{-j2\pi f \delta_{\tau_{p,i}}} \tag{2.9}$$

where $\gamma_{p,0}$ represents the relative coefficient of the stable path with $\delta_{\tau p,0} = 0$.

In general small scale coefficient $\gamma_p(f)$ has a complex Gaussian distribution with mean $\bar{\gamma}_p(f)$ and variance of $2\sigma_P^2(f)$. While the $\bar{\gamma}_p(f)$capture location uncertainty, the $2\sigma_P^2(f)$ are influenced by the changing environmental conditions (e.g., surface

roughness that changes with the wind/wave activity). Both sets of parameters can thus change over prolonged intervals of time.

The path statistics in Equation 2.9 including $\bar{\gamma}_p(f)$ and $2\sigma_P^2(f)$ can be determined experimentally if the intra-path delays distribution of $\delta_{\tau_{p,i}}$ and intrapaths gain $h_{p,i}$ statistics are known.

Finding the intrapaths delays structure and their impact on the channel frequency response is one of the main objectives of this research. One of the potential techniques to find statistical property of the intra paths delays is fitting the intrapath delays samples to a Gaussian distribution to find variance of intrapath delays distribution which will be discussed in detail in Chapter 4

2.2.1 Channel State Information Representation

The channel quality can be expressed in term of set of parameters which are addressed here as the CSI. The channel quality depends heavily on the channel gain, delay and Doppler spread [16].

Following we will discuss these parameters and acquire them analytically from channel transfer function.

Channel Gain: Since the channel $H(f, t_n),\ t_n \in T$ is frequency selective, the overall channel instantaneous gain $G(t_n)$ over the band width B at time t_n can be calculated from

$$G(t_n) = \frac{1}{B}\int_{f_0}^{f_0+B} |H(f, t_n)|^2 df, \tag{2.10}$$

By averaging the instantaneous channel gain over longer large-scale interval $t \in [0, T]$ or several seconds we can obtain large-scale channel gain

$$G = E\{g(t)\} \tag{2.11}$$

Delay Spread: The delay spread is used to measure the channel time dispersion in multipath environment, often defined as the time between the first significant path arrival and the last significant path arrival. Delay spread imposed by multipaths has a significant impact on intersymbol interference (ISI). The delay spread leads to time dispersion and frequency-selective fading. The time dispersive properties of wide

band multipath channels are most commonly quantified by their mean excess delay $\bar{\tau}$ and RMS delay spread τ_{RMS}. The mean excess delay is the first moment of the power delay profile. Each cluster of arrivals has different dispersion properties. We can define the RMS delay spread τ_{RMS} for cluster p as

$$\tau_{\text{RMS}_p} = \sqrt{\bar{\tau_p^2} - (\bar{\tau_p})^2}, \tag{2.12}$$

where

$$\bar{\tau_p^2} = \frac{\sum_i {h_{p,i}}^2 \tau_p, i^2}{\sum_i {h_{p,i}}^2}, \tag{2.13}$$

and

$$\bar{\tau_p} = \frac{\sum_i {h_{p,i}}^2 \tau_{p,i}}{\sum_i {h_{p,i}}^2}, \tag{2.14}$$

where $h_{p,i}$ is the gain of intra-paths within cluster p.

The maximum excess delay of the power delay profile for path p is defined to be the time delay during which multipath energy falls to X dB below the maximum. The maximum excess delay can be written as $\tau_{p,x} - \tau_{p,0}$, where $\tau_{p,0}$ is the first arriving signal and is the maximum delay at which a multipath component is within X dB of the strongest arriving multipath signal.

Time and Frequency Correlation of the Channel: In addition to the frequency selectivity of the channel, time-variance impacts the statistics over time. The correlation of the scattering coefficients $\gamma(f)$ over the time of Δt is described by

$$R_p(f, \Delta t) = E\{\gamma_p(f, t + \Delta t)\gamma_q^*(t)\}. \tag{2.15}$$

As explained in [6], the correlation of the channel over time is related to the effective Doppler spread of a path. The Doppler spread is a parameter that describes the frequency dispersion of acoustic channel. Doppler spread imposes inter-carrier interference (ICI) and is an impairment well known to degrade performance of Orthogonal Frequency Division Multiplexing (OFDM) transmissions. Effective Doppler spread of a path characterized by the small-scale coefficient $\gamma_p(f, t)$ using

$$E\{\gamma_p(f, t + \Delta t)\gamma_q^*(t)\} \approx 2\sigma_p^2(f)e^{-\pi B_p(f)\Delta t}, \tag{2.16}$$

where

$$B_P(f) = (2\pi f \sigma_{\delta p})^2 B_{\delta p}. \tag{2.17}$$

In (2.17), $B_p(f)$ is the effective Doppler bandwidth or Doppler spread of the path coefficient $\gamma_p(f,t)$. Also, $B_{\delta p}$ is the 3-dB bandwidth of the power spectral density (PSD) of the intra-path distribution of $\delta_{\tau_{p,i}}(t)$. Moreover, $\sigma^2_{\delta_p}$ is the variance of the intra-path distribution $\delta_{\tau_{p,i}}(t)$. The approximation is valid for $\Delta t << 1/B_{\delta_p}$. Note that, as such, the frequency correlation of the small-scale path coefficient depends on Doppler spread of the path coefficient $\gamma_p(f,t)$ and variance of paths.

Figure 2.3 shows time and frequency dispersion of an acoustic channel.

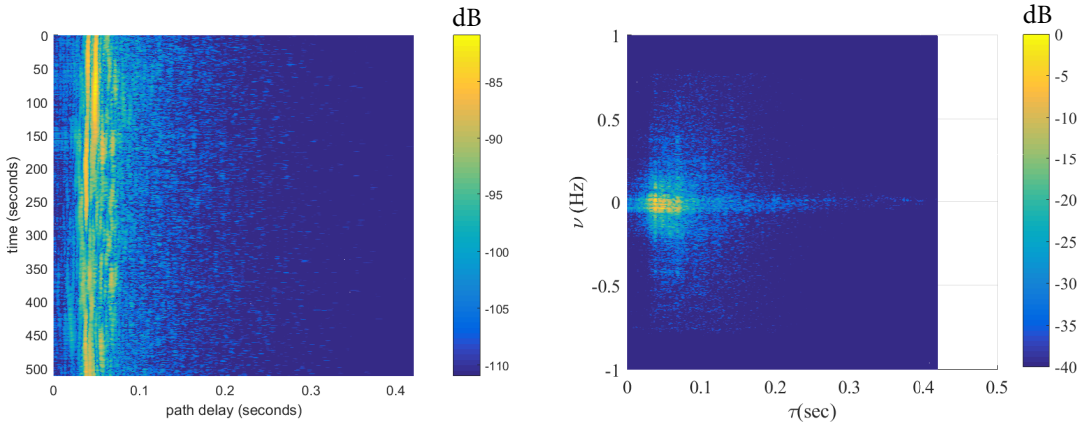

(a) Channel impulse response evolution of a 1 km acoustic channel over six minutes.

(b) Delay-Doppler dispersion of a 1 km acoustic channel over six minutes.

Figure 2.3: Dispersion of a 1 km acoustic channel in time and frequency, UW-STREAM Lab Seaport Deployments, Halifax, NS., 2015.

Coherence Bandwidth: Analogous to the delay spread parameters in the time domain, the coherence bandwidth is used to characterize the channel in the frequency domain. The RMS delay spread and coherence bandwidth are inversely proportional to one another.

While the delay spread is a natural phenomenon caused by reflected and scattered propagation paths in the acoustic channel, the coherence bandwidth, is a defined relation derived from the rms delay spread. The coherence bandwidth, can be derived from the RMS delay spread and channel frequency correlation. Coherence bandwidth is a statistical measure of the range of frequencies over which the channel can be

considered "flat".

This is an important parameter in defining subcarriers bandwidth in an OFDM system.

The analytic issue of coherence bandwidth was first studied by Jakes [40], where by assuming homogeneous scattering, the coherence bandwidth of a channel is inversely proportional to its RMS delay spread as expressed by

$$B_c \propto \frac{1}{\tau_{\mathrm{RMS}}}, \tag{2.18}$$

where τ_{RMS} denotes the RMS delay spread.

However, based on experimental data, Rappaport and Lee modified Jakes' formula to obtain a formula for coherence bandwidth which was initially developed for Wide-Sense Stationary (WSS) frequency-nonselective (narrowband) Rayleigh fading channels by

If the coherence bandwidth is defined as the bandwidth over which the frequency correlation function is above 0.9, then the coherence bandwidth is approximately

$$B_c \approx \frac{1}{50\tau_{\mathrm{RMS}}}, \ for\ \eta_0 = 0.9 \tag{2.19}$$

This formula resembles the original one by Jakes except a different scaling factor, which depends on the preset CSI level η_0 for frequency correlation.

If the definition is relaxed so that the frequency correlation function is above 0.5. then the coherence bandwidth is approximately

$$B_c \approx \frac{1}{5\tau_{\mathrm{RMS}}}, \ for\ \eta_0 = 0.5 \tag{2.20}$$

Assuming a WSS rayleigh fading for a wide band underwater acoustic channel is not a valid assumption and B_c should be calculated from the measured base band channel impulse responses (CIRs). The coherence bandwidth B_c can be calculated as the width of spaced frequency correlation function, $R_p(\Delta f, t)$ at a given threshold η_T [41].

Frequency correlation function is a key function involved in expressing a channel quality over the proposed transmission bandwidth. If there is significant degradation in this correlation, time varying signal distortion and time varying ISI will occur [42].

The frequency correlation of the small-scale path coefficients is described by the function

$$\begin{aligned}\eta = R_p(\Delta f, t) &= E\{\gamma_p(f+\Delta f, t)\gamma_q^*(t)\} \\ &= E\{[\gamma_p(f+\Delta f) - \bar{\gamma}(f+\Delta f)][\gamma_p(f) - \bar{\gamma_p}(f)]^*\}\end{aligned} \tag{2.21}$$

2.3 Adaptive Physical Layer in Underwater acoustic Networks

The deployment of underwater networks with reliable, energy efficient and low latency communication links is key to enable the deployment of remote underwater sensing and monitoring instruments [12]. For reliable and energy efficient UWANs, several cross-layer optimizations have been proposed to configure the physical layer of individual nodes. This section presents common physical layer and signal modulation techniques that are most frequently employed in UWA communication systems and suggests an adaptive approach based on OFDM physical layer. In general the proposed modulations for UWA communication systems can be classified in two categories: non-coherent and noherent modulation, as will be explained here.

Non-coherent modulation

By definition, for a non-coherent digital modulation technique, there is no need for the two carriers (at the transmitter and receiver) to be phase aligned.

In UWA communication systems non-coherent detection of frequency shift keying (FSK) signals has been used widely for channels exhibiting rapid phase variation such as the long and medium range shallow water channels. To overcome the intersymbol interference (ISI) the noncoherent systems employ signal design with guard times which are inserted between successive pulses to ensure that all the reverberation will vanish before each subsequent pulse is to be received. The insertion of guard times results in a reduction of the available data throughput. In addition, due to the fact that fading is correlated among frequencies separated by less than the coherence bandwidth (the inverse of the multipath spread), it is desired that only those frequency channels separated by more than this amount be used at the same time. This

requirement also reduces the system efficiency. Noncoherent FSK is a good solution for applications where moderate data rates and robust performance are required [43].

In underwater communication systems, FSK has been extended to include frequency hopping (FH). Specifically, FH-BFSK has been selected for its robustness in harsh UW acoustic propagation environment and for its simplicity of implementation [44]. FH-BFSK is a non-coherent physical encoding technique, and is already used in commercially-produced modems. It is also robust to packet collision, supporting a degree of multiple simultaneous access that is valuable in a simple protocol with a limited medium access control complexity [45].

Frequency hopping spreads the signal in frequency and time to mitigate the effects of the variable multipath. The hopping pattern must be known at the transmitter and receiver to spread and despread the signal. Figure 2.4 shows an example of frequency hopping for BFSK modulation. The green symbols are transmitted at the different sub-carrier frequencies according to a pre-defined hopping sequence. T_c is the hop period during which the carrier frequency stays constant. T is the symbol period, T_b is the bit period, W is the spread bandwidth, W_d is the symbol bandwidth, and in this example there are $L = 4$ frequency hopping levels, between which the carrier switches. By increasing the frequency hopping levels' counts, and reducing the hop period, constrained on the bandwidth, robustness against eavesdropping is improved [46].

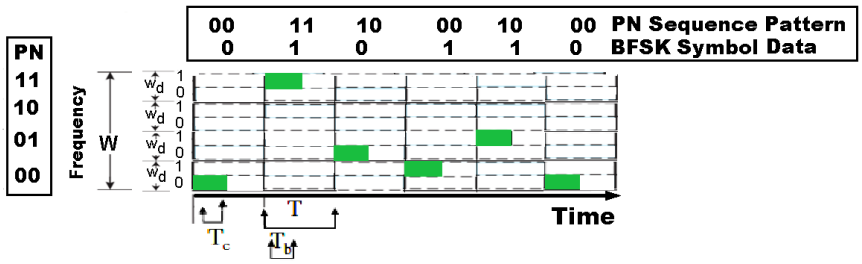

Figure 2.4: Frequency Hopping in FH-BFSK system.

Let's define the FSK output waveform as

$$s_d(t) = A\cos(2\pi(f_0 + 0.5(b_i + 1)\Delta f)t), \quad \text{for} \quad iT_b < t < (i+1)T_b, \tag{2.22}$$

where f_0 is the carrier frequency, Δf is the separation between the FSK sub-carriers,

b_i is the i^{th} bit, and T is the duration of the single bit.

Then, the upconverted output of the FH-FSK system given a hop frequency f_i for bit index i is equal to

$$p(t) = \mathbb{R}\{A\cos(2\pi(f_0 + 0.5(b_i + 1)\Delta f)t)\exp(2\pi f_i t)\} \tag{2.23}$$

When the signal is received at the receiver, the original bit value b_i can be recovered by following the reverse process, as long as the sender and the receiver are synchronized with respect to the pseudo-noise sequence [47].

A key parameter to achieve reliable non-coherent communication in a highly distorting environment is such that the symbol time must be much greater than the multipath delay spread, τ_{RMS}. In FH-BFSK systems, the tone duration should be longer than the delay spread. This results in narrow frequency bands, which are subject to frequency selective fading. To minimize the sensitivity to Doppler shift, a wider frequency bin, larger than the expected Doppler shift estimation should be used. This minimizes the frequency selective fading but causes inter-symbol interference unless a sufficient guard time is considered in the signal design. Also BER increases due to frequency collision, as a small number of frequency bins are available. The performance of FH-FSK clearly depends on the multipath delay spread and the ability to estimate the Doppler shift. Despite its robustness, an FH-BFSK system has poor bandwidth and power efficiency [48].

Coherent modulation

Over the past decades, phase-coherent modulation techniques such as phase-shift keying (PSK) and quadrature amplitude modulations (QAM) have attracted a lot of attention to increase the bandwidth efficiency of UWA communication systems. While phase-coherent modulations are bandwidth-efficient methods and have successfully been tested on a variety of channels. However, in some applications, unpredictable motion of the receiver and transmitter, as well as changes in the transmission medium, cause severe phase fluctuations. This is the main reason coherent communications are often not considered feasible [49]. One of the widely used coherent modulations in UWA communication is OFDM system.

Orthogonal Frequency Division Multiplexing

An OFDM signal contains a sum of subcarriers that are phase shift keying (PSK) or quadrature amplitude modulation (QAM) modulation. Each parallel data transmission is modulated by different carrier frequencies using modulations such as PSK or QAM scheme. Also to reduce the complexity of OFDM implementation, the IFFT and FFT are employed to replace the banks of sinusoidal generator for the modulation and demodulation. In general, an OFDM system at least contains the function of parallel transmission, signal mapping and IFFT/FFT. Figure 2.5 illustrates the block diagram of a discrete-time FFT-based OFDM systems model

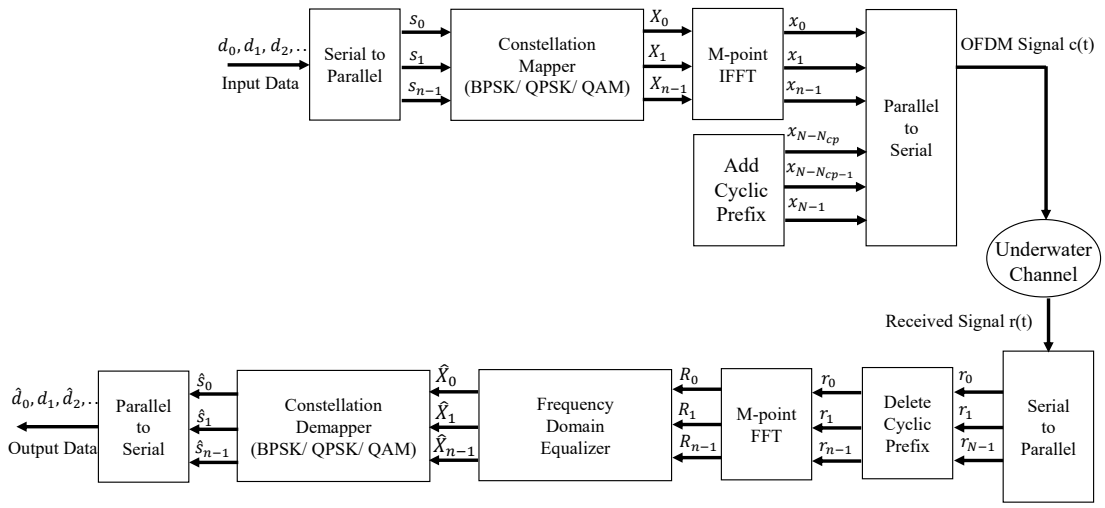

Figure 2.5: Block Diagram of an OFDM system [7].

The input binary information $d_0, d_1, \cdots$ is converted from serial to parallel and then modulated, for example, using PSK/QAM. The parallel data is converted to N parallel symbols, which are applied to an IFFT. The last N_{cp} outputs of the IFFT are pre-pended at the end of the vector. This is the cyclic prefix. With a cyclic prefix, the complete OFDM symbol $c(t)$ is transmitted over a discrete-time channel. At the receiver, the received data $r_0, r_1, \cdots, r_{N-1}$ are converted from serial to parallel, and the cyclic prefix is deleted. Next, after the parallel $r_0, r_1, \cdots, r_{n-1}$ is retrieved by a FFT block. The OFDM Frequency Domain Equalizer block equalizes the OFDM data using channel estimates [50, 51] and, then, $\hat{X}_0, \hat{X}_1, \cdots$ demapped with corresponding

scheme to obtain the estimated data [52] and finally converted from parallel to serial data $\hat{d}_0, \hat{d}_1, \cdots$ as output data.

Over the last two decades OFDM systems have been widely studied for use in UWA communication because of their high bandwidth efficiency and robustness to channels that exhibit long delay spreads and frequency selectivity [53]. However, OFDM systems are known to be sensitive to the UWAC time varying conditions and their performance depends on the accuracy of transmitters knowledge from the channel. Specifically, motion-induced random Doppler frequency shifts result in nonuniform frequency shift across the signal bandwidth and impose inter-carrier interference (ICI). Also, the delay spread in a time varying channel leads to time dispersion result in inter-symbol interference (ISI) and frequency-selective fading. To mitigate the channel impairments on OFDM systems performance adaptable OFDM systems has been studied.

In [13], the design aspects for adaptive modulation based on OFDM for underwater acoustic (UWA) communications are explored. The authors investigated the possibility of predicting a UWA channel at least one travel time ahead. The Matching Pursuit algorithm is used to identify path coefficients. Then, assuming that the channel is predicted one travel time ahead, expressions for the BER of each subcarrier are obtained. From these expressions, a set of thresholds is obtained that determine the modulation level and the power needed on each subcarrier to maximize the throughput while keeping the average BER at a target level. Spectrum efficient adaptive schemes are also applied to allocate the modulation and the power across the OFDM subcarriers. Energy efficiency has been studied widely in recent years for OFDM systems [54, 55, 56]. In [57], for each node, the physical layer parameters are adjusted to optimize the average transmission energy per bit in the network. In order to improve energy efficiency, the CSI can be used at the transmitter to optimize the power efficiency.

2.3.1 Adaptive OFDM Based Physical Layer

An acoustic channel can impact an OFDM system performance by imposing frequency dependant transmission loss, intersymbol interference (ISI) and intercarrier interference (ICI).

The main advantage of OFDM over single-carrier schemes is its ability to cope with severe channel conditions. At the physical layer, it is possible to increase the the number of useful information bits delivered by reducing the cyclic prefix (CP) length or guard bands in OFDM systems or improve the power efficiency by decreasing the transmission power when the channel condition allows.

In OFDM systems, the cyclic prefix (CP) length needs to be larger than the maximum excess delay of the channel. If this information is not available, the worst-case channel condition is used for system design, which makes the CP a significant portion of the transmitted data. One way to increase the spectral efficiency is to adapt the length of the CP to the changing multipath conditions, which requires channel excess delay knowledge [32].

The OFDM physical layer design parameters include sub-carrier bandwidth, number of subcarriers, cyclic prefix size, symbol rate, symbol duration, modulation level, code rate, guard interval, presence of pilot tones, and transmitting power.

An OFDM system can simply redefine the number of carriers, i.e., the size of the FFT or cyclic prefix size to mitigate ISI [8]. Also, FFT-based processing is computationally efficient to implement OFDM. Which makes it a good candidate to be employed in adaptive underwater acoustic system [58, 59, 60].

An adaptive OFDM system can utilize CSI to mitigate the frequency selectivity effect of channel in the physical layer. Accordingly the following conditions need to be considered in OFDM signal design:

- The symbol duration T_s must be chosen such that $T_s << 1/\nu_{RMS}$, where ν_{RMS} is the channel Doppler spread. The symbol duration should be kept smaller than the minimum channel coherence time.

- The sub-carrier separation is generally designed such that $\Delta f << 1/\nu_{RMS}$.

- The OFDM cyclic prefix duration $T_{CP} \geq \tau_{RMS}$ to prevent ISI due to delay spread

- $T_{CP}\Delta f << 1$ for spectral efficiency improvement.

Most of the objective functions that have been considered for adaptive communication can be roughly divided into two categories: i) very robust, low rate modulations

reaching a rate in the order of hundreds of bits/s, exploiting long-lasting symbols and various types of spread spectrum modulations; ii) high data rate modulations for short/medium distance connections, reaching nominal data rates of hundreds of kbit/s [61]. For the first category FH-BFSK attracted many attentions and is used as a standard in Janus [62, 63, 64]. In the second category of solutions which trying to achieve higher spectral efficiency, OFDM modulation has emerged as a promising solution for UWA communications [65] and attracted a lot of attentions for its adaptation capabilities [66, 5, 67]. Both of these approaches have capabilities to be used in multi-user networks and adapt to channel impairments.

2.4 Adaptive Multihop UWAN

There have been extensive works to investigate multiple users and relay deployment problems in underwater acoustic networks from different perspectives, e.g., energy efficiency, reliability and latency. Over the past twenty years, various UWAN topologies and protocols have been proposed. In the UWAN, the challenges related to long end-to-end latency, high energy consumption, dynamic network topology and short network lifetime are much more important that in conventional terrestrial networks.

To realize a high data rate, energy-efficient end-to-end communication link over large areas spanning several square kilometers, more recently, the emphasis has shifted toward multi-hop relaying networking as a means to provide wider area coverage [68]. Here, we focus on underwater distributed multi-hop scenarios. A multi-hop peer-to-peer network is formed by establishing communication links only between neighboring nodes. Messages are transferred from source to destination by hopping packets from node to node [69]. Deploying relays to shorten the hop distance can expand the effective bandwidth and reduce the transmit power of each hop [70].

Figure 2.6 depicts a distributed multihop relaying topology for data collections scenarios where nodes can be deployed in a relatively large area, and supported by a surface sink node.

Following, we will review the currently proposed MAC and multihop relaying schemes for UWANs.

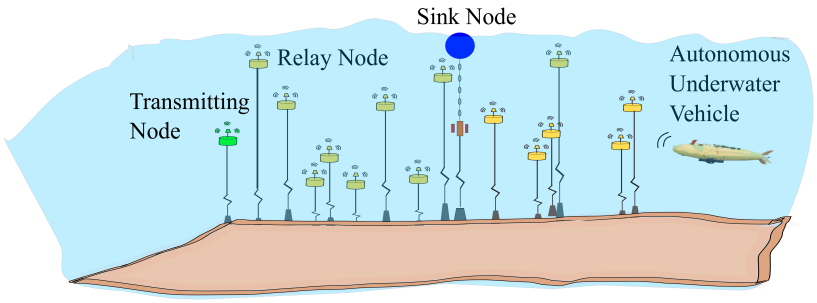

Figure 2.6: Illustration of a distributed underwater network topology.

2.4.1 Media Access Control in UWAN

In this section we will review multiple access methods for UWANs and then suggest a framework to use CSI in an adaptive OFDM-Based MAC for network nodes in data collection applications.

One of the main challenges to enable UWA networking is to design an efficient MAC protocol tailored to the harsh underwater acoustic environment.

Various MAC protocols are proposed for energy and channel utilization optimization [71, 72].

A general classification of MAC protocols proposed for UWANs is presented in Figure 2.7.

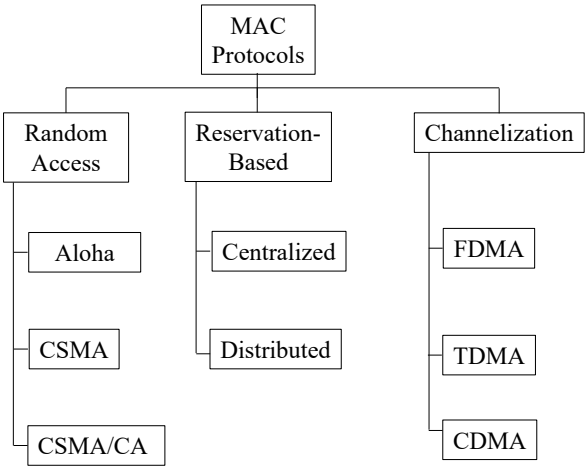

Figure 2.7: General classification of MAC protocols [4].

.

With regards to the MAC protocol, initially, random access based solutions such

as Slotted-ALOHA were adopted [73]. In a centralized topology, the sink node coordinates and provides access to the channel with the multiple users. A slotted Aloha MAC suits centralized topologies because of its low collision probability and high throughput. Centralized channel access management and synchronization by a cluster head has low complexity and energy dissipation, many challenges arise with such an architecture. As such, when there is excessive nodes, the cluster head sub-net run out of channel access time-slots and some nodes within the cluster head's can get access to the channel. Alternatively, in self-organized ad hoc networks, to access the media, the unslotted Aloha MAC with Carrier-sense multiple access with collision avoidance (CSMA-CA) mechanism can be considered by the UWA nodes. In Ad hoc networks Unslotted Aloha is preferred because it is scalable and does not require handshaking and global synchronization. However, the distributed channel access methods are usually more complex and required excessive controlling messages within the network to reserve a channel and avoid collision [74] The throughput of Slotted-ALOHA can be improved by introducing a guard time. In [75] two variants of Aloha are designed with collision avoidance capability to achieve a better performance.

Since random access-based approaches cannot effectively avoid collisions in distributed networks, some studies have explored reservation based or handshake- based MAC with contention. In order to improve the energy efficiency some floor acquisition multiple access (FAMA) schemes proposed which combines both carrier sensing (CS) and a ready to send (RTS)/ clear to send (CTS) exchange between the source and receiver prior to data transmission [76]. Multiple Access with Collision Avoidance (MACA) based protocols also studies for long propagation delay networks [77].

Channelization is a conventional method for multiple access control. The most common channelization methods are time division multiple access (TDMA), code division multiple access (CDMA) and frequency division multiple access (FDMA). There are many TDMA-based MAC protocols that jointly use other MAC mechanisms such as scheduling and reservation in a multi-hop network. For example, for time slot allocation, the WA-TDMA (Wave-like Amendment-based TDMA) [78] starts allocation from the central node to outward nodes in a form of wave-like proliferation to shorten network initialization time. In comparison, with the LT-MAC (Location-based TDMA MAC) [79] for a stationary meshed UWAN, each node circulates the

transmission permission according to a pre-determined sequence to shorten waiting time. Time slot assignment depends on the positions of related nodes. Slot length is decided dynamically according to traffic loads of the local node and its neighbors.

Other techniques have also been proposed combining TDMA on multi-hop networks. Transmit Delay Allocation MAC (TDA-MAC) and Accelerated TDA-MAC (ATDA-MAC) are capable of providing TDMA-based channel access to the network nodes without the need for centralized clock synchronization[80]. However, a large protocol overheard is generated to spread position and traffic load information. A relatively high propagation delay, long time guards and large signaling overhead [81] disputes the usefulness of TDMA particularly for networks covering vast areas.

As an alternative to TDMA, several proposals try to take advantages of the features of CDMA. In [82] a CDMA (using chaotic codes) relies on a closed-loop strategy based on measurements sent back by the receivers. Each receiver periodically collects information on the channel state. This information is then provided to the neighbors by transmitting short ACK/NACK messages. A MAC protocol jointly using CSMA/CA and CDMA is discussed in [83] for a star-topology, aimed at simultaneous transmissions without using RTS/CTS to avoid long handshaking delay. The power control required with CDMA usually implies a star topology with a single base-station receiver, rather than an arbitrary distributed topology. Also, CDMA suffers from severe channel reverberation that may lead to degradation of the code correlation properties.

An orthogonal frequency-division multiple access (OFDMA) based MAC protocol named G-MAC proposed in [84] which leverages dynamic sub-channel allocation and transmission power adjustment. G-MAC is a multichannel MAC protocol dedicated for using in underwater centralized networks, which aims to maximize the network's goodput. To solve the optimal problem, G-MAC allows for concurrent data transmissions by applying Nash equilibrium to allocate transmission subchannel and related power adjustment. The convergence of the iterative process is arguable, especially in time varying environment.

Despite all the efforts in recent years to design underwater networking protocols and establishing a reliable and low latency end-to-end link from the underwater acoustic node to the surface sink nodes, the inherent characteristics of the multipath

underwater acoustic channel, including its time-variance and its long propagation delay as well as limited battery and limited bandwidth introduces important challenges.

Although OFDMA based MAC have been described, there are only a few studies that have been conducted to predict signal propagation and channel properties from the transmitter to the receiver and utilize this information in adaptive underwater acoustic OFDM signal generation and networking [66]. Filling this gap is the primary motivation of this study.

To enable adaptable OFDMA based MAC a metric is required to optimize the MAC layer. The available bandwidth for underwater acoustic (UWA) communication and networks is very limited, and frequency reuse is one of the important techniques to improve spectrum efficiency and system capacity. However, the long propagation delay and limited bandwidth of UWACs, the contention based algorithms with handshaking and random access-based MAC protocols do not perform efficiently. Using a collision-free frequency reuse approach is therefore considered to achieve high performance by avoiding the collisions at the MAC layer. Graph coloring techniques are promising technique to achieve as many concurrent conflict-free transmissions as possible in any two-hop neighbourhood as will be described in Section 3.3.

In the MAC layer, the network throughput can be increased by maximizing the channel utilization, and the useful information bits increases by avoiding packet loss in collisions.

The power control can also be combined by frequency reuse to limit the carrier sense range mitigate interference in multiple access problem. Figure 2.8 shows a graph coloring scheme with adaptive power control to allocate sub-carrier in OFDM-based networks using the predicted CSI.

2.4.2 Efficient Multihop Relaying in UWAN

In the UWAN, the challenges related to long end-to-end latency, high energy consumption, dynamic network topology and short network lifetime are much more important that in conventional terrestrial networks. There have been extensive works to investigate relay deployment problems in underwater acoustic networks from different perspectives, e.g., energy efficiency, reliability and latency.

The topologies to interconnect underwater acoustic nodes can be categorized based

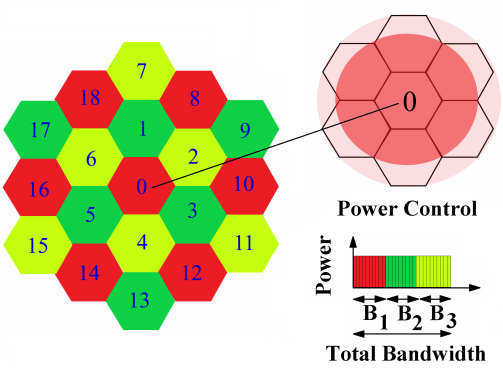

Figure 2.8: Frequency reuse based on Graph colouring to assign sub carriers accompanied by power control to avoid interference in multihop relaying.

on three categories: centralized, distributed, and multihop relaying [85].

In a centralized topology the covered area is limited and all the traffic goes through the cluster head node. As such, when there is excessive traffic, when the channel quality is poor or when the cluster head node is unavailable, the cluster head sub-net becomes unresponsive and all the nodes within the cluster head's coverage lose their connection.

A fully connected distributed peer-to-peer topology can also be used that provides peer-to-peer links between every node of the network. Such a topology eliminates the need for routing. However, the output power needed for communicating with widely separated nodes is excessive. Also, a node that is trying to send packets to a far-end node can interfere with a neighboring node.

Multihop relaying networks are formed by establishing communication links only between neighboring nodes and messages are transferred from source to destination by hopping packets from node to node. Multihop networks can cover relatively larger areas since the network range is determined by the number of nodes rather than the individual acoustic nodes.

However, as the number of hops increases, the packet delay also increases and special attention should be given to applications that are sensitive to delays. Selecting the minimum number of hops in relaying can save energy, and selecting relays with better link quality will increase the reliability and avoid retransmissions.

Flooding routing and relay selection protocols have been studied extensively. EFlood described in [86] is a broadcast protocol where a node immediately re-transmits

a received packet unless it is a duplicate. In EFlood, a node waits for a random duration before forwarding the packet. This random time depends on the network topology and on the packet transmission delay. As demonstrated in [86] the flooding-based protocol with multiple alternative paths can improve the packet delivery ratio (PDR) and latency in harsh underwater environment [46] compared to peer-to-peer relaying protocols. However in flooding based protocols more nodes forward packets and their overall energy consumption are significantly higher than peer-to-peer relaying protocols.

Recently, several proposals have adopted OFDMA for UWANs. The main issues addressed for OFDMA include sub-channel allocation, adaptability and energy efficiency. In [87] an OFDMA MAC which employs a joint relay selection and power allocation based on the handshake mechanism in a multi-hop network. Accordingly, a Particle Swarm Optimization algorithm is used to allocate the power on all sub-channels of each node; to reduce the network energy consumption while obtaining a large network throughput. Priority is set for each one-hop node according to the delay information. The authors considered propagation delay and energy efficiency for optimization, however the channel condition is not taken into consideration.

Among all the solutions, one that stands out in terms of overall remarkable performance is the Channel-aware Routing Protocol (CARP), using link quality information for successful data delivery to the sink[88]. Nodes are selected as relays based on their link quality, hop count and residual energy. CARP utilizes a channel reservation mechanism such as RTS/CTS for channel access and for selecting packet relays (cross layer design). For this reason, while being reliable and limiting packet collisions, it incurs noticeable latency. Also, in networks with high traffic, nodes often fail to obtain rights to access the channel, which results in low packet delivery ratio.

To improve energy efficiency, several routing protocols [89] have been proposed to seek the shortest path to forward data.

An adaptive clustering algorithm for multi-hop UWANs is proposed in [90] to optimize the energy consumption in an OFDM network with the coverage area of 10×10 km^2 with 50 nodes. The proposed energy optimization clustering algorithm scheme considers multiple factors, such as the number of neighbor nodes, the residual energy of each node, the motion of the nodes caused by the ocean currents, and the distance

between the sink node and each underwater node. However, channel impairments are not taken into account, and only the absorption coefficient and aggregate of ambient noise are considered in the channel model.

In comparison, in [88] a channel-aware routing protocol (CARP) is proposed to exploit channel quality information for data forwarding. However, because the channel is time-variant, the routing protocol must be re-trained at a frequent interval. To predict the conditions between the nodes in a UWAN, a real-time ray-tracing channel simulator can be embedded on the nodes as was described in [67]. However, it is well known that channel simulators have limited reliability, particularly in shallow time-variant environments.

In [91], network nodes obtain the channel quality by attempting different relay options over time. The packets are re-transmitted until they are received successfully, and a reinforcement learning approach is used to select the best forwarding relay. However, the re-transmissions may cause excessive spectrum usage as well as significant energy consumption. Furthermore, the link quality may change with time, and the optimization process may never converge.

An adaptive Deep Q-Network-based energy- and latency-aware routing protocol to prolong network lifetimes in UWANs proposed in [92]. However, here also the channel time varying conditions are not addressed, and the reward-based learning algorithm is based on iterative training. The convergence and performance of iterative algorithms in time varying environments are disputable. Due to variant nature of UWAC, it is important to define an adaptable communication stack, such that the physical layer , and the medium access control can adapt to channel and topology varying conditions.

2.5 A Review on Janus Protocol for Interoperability

To break the interoperability barrier and enable collaborative underwater communications, the Janus baseline packet structure, which is a NATO standard for digital underwater communications is introduced. Using a standardized protocol enables communication and packet forwarding among heterogeneous nodes [62]. As defined in the standard [63], the packet contains 64 bits, consisting of a 34-bit application data block (ADB) that is determined by the acoustic node. The ADB first 8 bits are for channel reservation and beacon and the remaining 26 ADB bits are node data.

The packet is assembled according to the bit allocation shown in Figure 2.9.

Protocol Version	Mobility Flag	Scheduling Bit	Tx/Rx	Forward Capability	User Class	Application Type	Repetition	ADB		CRC
								Reserved or Repeat interval	Node Information	
4	1	1	1	1	8	6	1	7	26	8

Figure 2.9: Janus Packet Bits 1 to 64.

A Janus baseline packet can also be complemented by a cargo section of arbitrary length. The system also employs a 1/2 rate convolutional encoder [93] that is applied to the 64 bits of Janus packet and is intended to combat the channel multipath interference as well as fading. Prior to encoding, 8 zeros are added to the data to flush the encoder, which will be discarded at the receiver. The total number of symbols output by the 1/2 rate convolutional encoder then becomes $2\times(64 + 8) = 144$ [64]. A fixed preamble of 32 chips is employed for detection and synchronization. As such, altogether a Janus packet comprises 176 chips. So, each packet duration is equal to 2,288 msec without the optional cargo.

2.6 Summary

In this chapter, adaptive cross-layer design for UWA has been discussed. First, a cross-layer design is defined for optimum network resource use and high adaptability. Then, underwater acoustic channel characteristics and CSI definition are presented in the second Section. The third Section presents the common physical layer and signal modulation techniques most frequently employed in UWA communication systems. The fourth Section reviewed multiple access methods for UWANs and proposed a framework to use CSI in adaptive OFDM-Based network nodes. Finally, in the last Section, Janus baseline packet structure is reviewed as a NATO standard protocol for digital underwater communications.

Chapter 3

Routing and Channel Allocation in Multihop Relaying Network

The temporal and spatial variations of UWA channels, particularly in shallow water, necessitate the design of dedicated network protocols for UWANs. To enable underwater acoustic networking, it is important to design the communication stack to be adaptable to time varying channel conditions. Although there is a significant amount of work has been performed in recent years towards the deployment of UWANs, there is still a gap that needs to be filled to address the routing and media access control problems in UWANs.

In this chapter, first in Section 3.1, a network architecture for adaptive multihop UWANs is proposed. Then in Section 3.2 an optimized flooding routing protocol to exchange network control messages and a channel-aware routing protocol to relay data packets are proposed. Then in Section 3.3 a channel-aware MAC scheme is proposed to allocate available channels while avoiding collision and maintaining connectivity within the multihop relaying network.

3.1 An Architecture for Adaptive Multihop UWANs

In this section, an architecture for the proposed UWAN is described. Typically, a clustered topology in which acoustic nodes are interconnected to a sink node is suggested for UWANs [15, 94, 95]. Instead, in this work, within each cluster a distributed multi-hop network topology is assumed to extend the network coverage and includes multiple fixed and mobile acoustic nodes. Similarly, each cluster of nodes is supported by a sink node. The significance of the proposed model is considering the acoustic link quality and the minimum re-transmissions as a benchmark for relay selection in multi-hop relaying. In the proposed network, it is assumed that each node knows its depth, as well as the sea bottom bathymetry. Also, the local sound speed profile (SSP) is available at each node.

The proposed communication system structure requires two phases for communication. First, an initial network control phase that provides a *priori* knowledge about the topology and potential routes to the nodes in the cluster. The network control phase is initiated by a beacon signal from the sink node. Second, a data transmission phase in which multi-hop relaying is used to forward data packets from the transmitter node to the sink node. Figure 3.1 illustrates the two network communication phases.

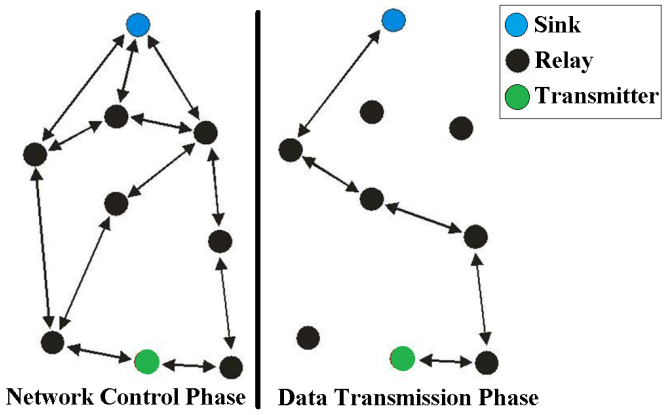

Figure 3.1: Illustration of control and data transmission phases.

In the network control phase, each AN acquires *priori* knowledge about the network using periodic beacon signals. These beacons are discovery messages and are initiated to broadcast from the sink node to train a channel prediction model at each receiving node. Using a beacon forwarding strategy described in [96], each receiving relay node piggybacks its ID on the received beacon and broadcasts it again. The network discovery beacons are short messages which are broadcast using the flooding routing protocol [46].

As illustrated in Figure 3.1, during the network control phase a discovery message is forwarded from the sink node to all cluster nodes through relay nodes. The discovery messages provide each node the information about its neighbors. As such each node can learn about the existence of the possible routes to the sink node by reading the sink node's ID in the received beacons. The beacons can also be used to obtain information about the location of the different nodes.

It is also assumed that the physical environment parameters are available at each node. Then, each AN estimates the channel impulse response to its next one-hop

relays using a built-in Bellhop software and stores in memory a channel samples window of the most recent channel impulse impulses, this will be described in 5.3. Specifically, each transmitter node i) simulates the channel condition of its one-hop relay nodes, and ii) weighs each link to its one-hop neighbors, as will be explained in Section 5. Then, the transmitter node selects the optimal next hop relay according to the highest channel quality weight to send its data packets.

3.2 Multihop Relaying in UWAN

Multihop relaying [97] is considered the preferred network topology to cover large areas underwater, but the efficiency and practicality of the provided solutions are questionable. In this section, two multihop relaying schemes are proposed for UWANs. First, in Section 3.2.1, the design approach for a proposed Optimized Flooding Routing Algorithm is to achieve high reliability while optimizing energy compared to similar approaches. Second, in Section 3.2.2, a multihop channel-aware relaying scheme is suggested, which considers the link quality as a metric for relay selection.

3.2.1 Optimized Flooding Routing Algorithm

The main challenge for a collaborative routing design in an UWAN is to obtain a high packet delivery ratio (PDR) with low end-to-end latency and energy per bit consumption.

Flooding-based routing protocols have attracted a lot of attention as a reliable solution for multi-hop UWAN due to their low latency and high packet delivery ratio (PDR) [46]. In this section, a flooding routing algorithm is described to optimize the PDR without excessive packet relaying to save energy.

In Figure 3.2, an illustration of the flooding routing in the ad hoc mode where a packet is forwarded from the source to the destination node by broadcasting through multiple relay nodes is illustrated.

To manage the routing, each node has a unique 8-bit identifier included in the packet's header. The source and relay nodes that forward the packet fill this field with their own identifier. The packet's intended destination node is also specified by a second 8-bit identifier, which is intended to be left unchanged during the routing. Furthermore, a 5-bit packet index is included to indicate the number of consecutive

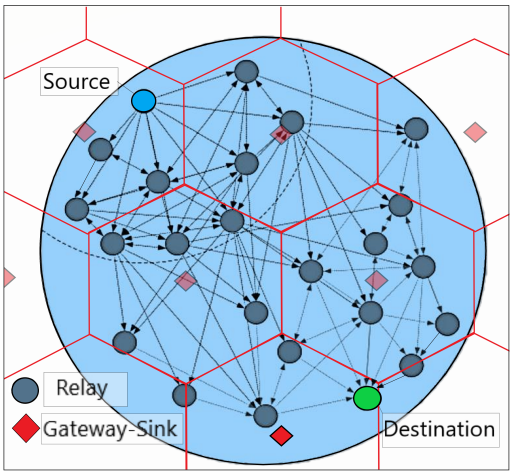

Figure 3.2: Flooding Routing in Ad hoc mode Topology.

transmitted packets, and is reset after every 32 cycles. To avoid excessive packet forwarding in the network a 3-bit local hop counter H_r is also defined at relay r. The size of local hop counter depends on the distance between two relay and destination nodes in the network and relay's acoustic transmission range, as will be explained later. These 22 bits are added to the Janus packet optional user defined cargo, thus increasing the original 64-bit packet size by 34%.

To calculate the local hop count, each node has a location table in its memory that stores its estimated distances from other nodes in the network. This information is updated every T_D seconds, depending on the velocity of the mobile nodes.

When a source node has data to send and the sink node is out of reach, it sends the packets to the ad hoc mode MAC layer to format the header and manage access to the media.

The relay node r buffers its incoming packets and classifies them by their sequence number and sorts according to their maximum received signal strength. The relay node accepts packets for $T_r = R_T/v$ seconds after receiving the first packet, where R_T is its maximum transmission range and v is the speed of sound. After a timeout T_r is expired, the relay node decodes the first packets in each class and detects the CRC errors. If itself was not the intended destination, it acts as a relay node and sends them to the MAC layer. Otherwise, it stops relaying and returns the ACK beacon. Before forwarding the packets, the relay node senses the channel. If it is available, then it broadcasts a beacon to notify the neighbors about channel reservation. This

beacon is also an acknowledge for the received packets and includes their sequence numbers. If the previous relay node $r-1$ does not receive the ACK of a sent packet after a timeout of $T_{ACK} = 2((n+1) - i_{th}) \cdot (R_T/v)$ seconds, it resends the i_{th} packet again for a maximum 3 times. Once an ACK is received by relay node $r-1$, the buffers can be discarded from the received packets.

To implement the routing algorithm, we use the fact that, for a given arc between a source and destination node, the maximum area covered is when the arc length is equal to that of a half circle. Then, to maintain network connectivity in the area using the minimum number of hops, a local hop count is calculated based on the length of the arc of a semicircle. The semicircle diameter is the distance between the source and destination node. At each relay r, the local hop count H_r is calculated as

$$H_r = \left\lceil \frac{\pi \cdot D_r}{2R_T} \right\rceil, \tag{3.1}$$

where D_r is the Euclidean distance between the relay and destination,$\lceil \cdots \rceil$ is the ceiling math operator, and R_T is the transmission range.

For the first hop, $r = 1$ and the repetition flag as defined in the Janus packet cargo is cleared while the forwarding capability flag is set to one. After sensing the channel availability, the source node broadcasts an ad hoc mode demand beacon to its neighbors to reserve the channel. Then, after a configuration back-off time of T_c, the source node sends its packets. If the channel is occupied, the source node will make a second attempt after a channel back off time-out according to a backoff mechanism [98]. When a relay node r receives a packet, it checks the forwarding capability and repetition flags. When the forwarding capability is set, the relay r is allowed to forward the packet. The cleared repetition flag indicates that the packet is sent from the source node. In this scenario, the relay node can override the waiting time for receiving relayed copies. Also, the relay node checks the destination ID and calculates its distance D_r to the destination node to find its local hop count from Eq. (3.1).

Specifically, relay node i extracts H_{r-i} from the packet received from the previous relay $r-1$, then calculates $H_{r-i} \cdot R_T$ and compares it to its own D_r. If $D_r < (H_{r-i} \cdot R_T)$, then the relay r updates H_r using its D_r from Eq. 3.1, sets the repetition flag and clears the forwarding flag. Otherwise the forwarding flag remains set. After setting

the flags and reserving the channel, the relay node broadcasts the packet.

If a relay node receives a packet with a cleared forwarding flag and $D_r > (H_{r-i} \cdot R_T)$ or $H_{r-i} = 0$, it stops broadcasting the packet. Also, if $D_r < (H_{r-i} \cdot R_T)$, the node increments H_{r-i} by one and broadcasts the packet with the forwarding flag cleared. Next the performance of the presented algorithm to save energy and avoiding excessive packets forwarding will be evaluated by simulation .

Optimized Flooding Routing Simulation

In Figure 3.3 a simulation of the proposed flooding routing algorithm is illustrated. In this setting 40 nodes are randomly distributed in a 100 by 100 kilometers area. The Euclidean distance between the source and destination nodes is D_S= 62.45 km and the acoustic transmission range is assumed to be R_T= 20 km. From Eq. (3.1), the initial local hop is calculated to be five and it is updated as explained in each relay node until relaying converges to the destination. As shown in Figure 3.3 the relay nodes which are further from the destination compared to their previous relays clear the forwarding flag so that when the packet is forwarded away from the destination, the relaying is terminated. In this example, the packet is forwarded 71 times in the network by 28 nodes including the source and destination. Compared to common flooding routing where packets are forwarded 100 times by 37 nodes in the same conditions, this algorithm performed 29% better in term of reducing the forwarding times for the packet in the network and 24% better to reduce the number of participating relay nodes.

The multi-cast relaying mechanism required for flooding, significantly raises the energy demand. Also, excessive packet broadcasting increases the probability of collisions.

3.2.2 Channel Aware Relay Selection

The channel-aware routing protocols [88] are another promising routing scheme that exploits channel quality information for data forwarding.

The ANs are equipped with an out-of-band beacon generator to send discovery messages and busy tones. The network coverage is extended using multi-hop relaying between the ANs. When a transmitter node has packets to send after a collision

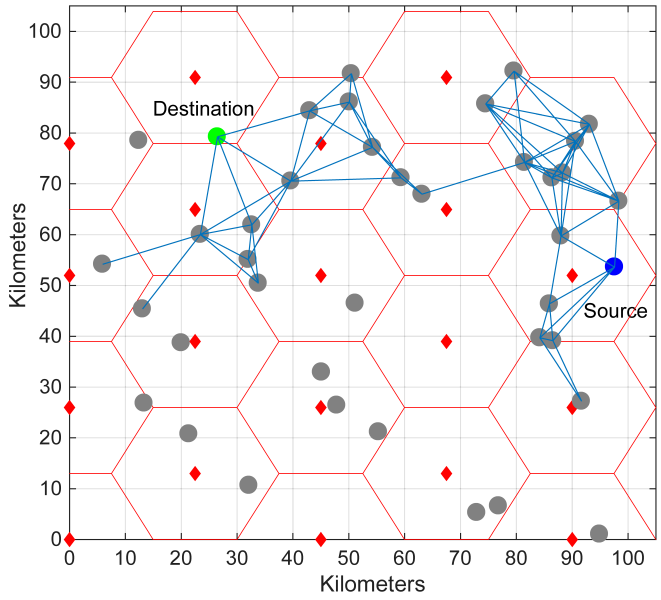

Figure 3.3: Optimized flooding routing model simulation.

detection backoff time T_L [99], it reserves the channel using a silence request to its neighbors and forwards its packets by sending them to its optimum neighbor relay node. The nodes are assumed to perform the synchronization based on a synchronization pattern taken from the received signal. The synchronization algorithm are assumed based on the correlation principle [100].

The varying ocean environment as well as differences in temperature, salinity and pressure for different water depth levels cause the acoustic rays to refract, which results changes in their path lengths. Accordingly, a time varying mutipath fading channel that is accompanied with large delay spread and Doppler spread is formed.

As shown in the following Chapter 4, an analytical channel model tracks channel variations in shallow water. Then, the overall gain and root mean square (RMS) probability density function for a channel between two neighbor nodes will be calculated.

The communication quality of the acoustic channel varies with time, as a consequence of the large-scale temporal variation in underwater acoustic channels.

These variations makes the end-to-end transmission paths unstable. To define the quality of an acoustic channel for underwater communication we use the channel gain and the RMS delay spread as the figure of merit. By using the a channel prediction

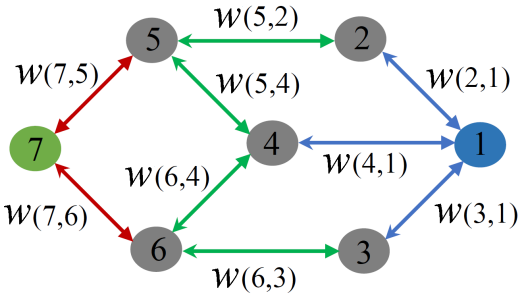

Figure 3.4: Illustration of a network routing using channel quality.

scheme which will be expianed in Section 5, the channel's state between a transmitter and next hop relays can be predicted to obtain channel quality.

In this application, the transmitter node i predicts the channel quality to each of its neighbors according to the posterior channel predictions, specifically using a channel characteristics scheme which will be explained in detail in Section 5, the channel gain and τ_{RMS} for each link $n \in (1, ..., N)$ will be predicted, where N is the number of its neighbors. Here the channel quality is defined using a weighting factor $W_{i,n}$ that takes into account the most probable channel gain and RMS delay spread values.The weighting factor is calculated as:

$$w_{(i,n)} = \frac{G(i,n)}{\tau_{RMS}(i,n)} \tag{3.2}$$

where $G(i,n)$ is the predicted channel's gain of the link n for the transmitter node i and $\tau_{RMS}(i,n)$ is the predicted channel RMS delay spread of the link n for the transmitter node i.

Specifically, each transmitter node i) simulates the channel condition of its one-hop relay nodes, and ii) weighs each link to its one-hop neighbors.

The routing optimization problem in Figure 3.4 can be mapped into a bidirectional graph G(V, E,W) where where V=(1, 2, 3, 4, 5, 6, 7) is the set of relaying nodes, E are set of peer to peer links between nodes and W is the local weighting factor of each edge. The multihop relaying optimization objective function can be defined based on the metric such as end-to-end delay, energy per bit consumption and packet delivery ratio.

$$W = \begin{bmatrix} 0 & ... & w(1,7) \\ ... & ... & ... \\ w(7,1) & ... & 0 \end{bmatrix} \tag{3.3}$$

3.3 A MAC Scheme to Maintain Connectivity and Fair Channel Allocation

In this section, a novel distributed scheme, the High Coverage and High Fairness (HCHF) algorithm, is proposed which employs a graph coloring technique to deal with interference [101]. HCHF improves the network coverage by ensuring that each transmitter-receiver pair can acquire at least one channel without sacrificing the entire network spectrum utilization efficiency. This ensures connectivity throughout the network and thus enables packet forwarding and routing between multiple nodes. To optimize the use of the sparse spectral resources, a channel sharing strategy among users will be developed to optimize the network connectivity and throughput.

In this work, the network path connectivity is guaranteed by ensuring that all transmitter-receiver pairs obtain access to at least one channel. Coverage, defined as the number of connected cognitive acoustic pairs, as well as fairness, defined as the number of pairs which obtain at least one channel, are two key figures of merit used to assess the performance.

The algorithm proposed here is intended to model and solve channel allocation problem in dense UWAN with high spectrum usage demand while dealing with interference. The network is intended to support the internet of underwater things (IoUT) and it can be expected that up to a few hundred sensor nodes with different purposes will be deployed in a target area spanning 10 km^2.

Also, practical issues such as collision avoidance and the hidden terminal problem will be taken into consideration during the design of the HCHF protocol, and will be presented.

3.3.1 Model of Control and Data Channels

In this section, firstly, a proposed multi-carrier multiple access channel allocation technique is described. Secondly, the use of the Janus protocol to enable the control

channel is described, third, the control packets and exchange procedure are defined. Fourthly, a graph model to obtain the interference matrix among neighbor nodes will be described. Fifthly, the channel allocation algorithm using the graph model is proposed.

Common Control Channel

To solve the channel allocation problem within a cluster subnet. A dense short-range UWAN considered with K ANs where each node is identified by an ID from $[1, 2, \cdots, K]$. It is assumed that a limited available spectrum is divided into M orthogonal equal bandwidth channels, presented as $[1, 2, \cdots, M]$ and $M << K$. Moreover, one common control channel (CCC) is dedicated for the exchange of the network management controlling messages. The CCC should be the most reliable local channel for exchanging MAC packets among the neighbor ANs. Note that channel allocation for peer-to-peer communication between two neighbor relays is considered in this work.

It is assumed that each AN can send and receive on all channels. Every node is aware of the local CCC and listens to this channel when it has no data to send or receive. To decrease the hardware complexity each node is equipped with a single wideband transceiver front-end that can dynamically switch between the CCC and available data channels. Further, each node is equipped with an inexpensive out-of-band tone device which can broadcast and receive busy tone signals. As explained in [102, 103] this allows each node to simultaneously broadcast and receive busy tone signals to solve the multichannel hidden terminal problem for nodes with single transceiver described in [104]. It is expected that high-quality filters shall serve to mitigate self-interference. The use of the busy tone to handle the hidden terminal problem will be explained in Section 3.3.1.

For the proposed network under study, there are several TX-RX pairs in the network that intend to utilize the available channels. The location of the nodes and the channel condition may vary with time and the goal is to optimally assign the channels to the TX-RX pairs in terms of spectrum utilization, coverage, and fairness at any given time.

To model the channel allocation algorithm, every node x that is within the transmission range R_T of the node y is considered a neighbor node of y. Therefore, two

nodes do not interfere with each other if their distance is larger than a range R_T, where R_T is considered to represent the radius of a circular transmission range from each node [105].

For a reliable network modelling, it is important to evaluate the channel transmission loss. As explained in [6], the channel amplitude is impacted by a large scale transmission loss (that can be assessed using ray tracing simulators for example) added to a small-scale variation because of the non-coherence addition of multipath arrivals. Generally, the small-scale variation of the amplitude is modelled as a Rician distribution, or in the extreme case as a Rayleigh distribution [23, 106]. Assuming a Rayleigh fading channel, a rule of thumb is to add 30 dB to the transmission loss to account for extreme small scale variation.

It is also important to consider the coherence time for underwater acoustic channels [107] which is defined as

$$\tau_c = \sqrt{\frac{9}{16\pi f_d^2}} \approx \frac{0.423}{f_d} \approx \frac{0.423}{a f_c}. \tag{3.4}$$

where f_d is the Doppler spread, f_c is the carrier frequency, and a is the Doppler scaling factor. As explained in [108], a stationary underwater acoustic system may experience unintentional motion at 0.5 m/s (1 knot), which would account for $a = 3 \times 10^{-4}$. In contrast an autonomous underwater vehicle (AUV) moving at several meters per second, Doppler factor a will be on the order of 10^{-3}. In fact, it has been reported in [10, 109] that the coherence time is on the order of 100 milliseconds in fixed conditions, while the channel between mobile vehicles can experience a channel coherence time on the order of a few milliseconds. It is assumed that the sound speed c in the water column between the transmitters and receivers has a constant velocity of $c = 1500$ m/s. The propagation delay, $T_p = R/c$, for the expected transmission range, $R = 500$ meters between the nodes will be about 334 msec.

Since underwater transmission is slow, the packet duration is often longer than the channel coherence time. For this purpose, in this work it is assumed that the physical layer is resilient to Doppler fading within the transmission of packets. The frequency-hopping binary frequency shift keying (FH-BFSK) is studied in this work, the binary information is represented using different frequency tones. As will be demonstrated, since the coherence time is greater than a few milliseconds, the channel is expected to

stay relatively constant during the transmission of the individual tones. Transmission of acoustic signals will be described in the next section.

Using FH-BFSK for Control Channel

In this work, an UWAN is considered in which 10 distinct 2-kHz channels are defined over a total frequency range between 10.5 kHz and 30.5 kHz. For mobile AUVs where $a = 10^{-3}$, the maximum Doppler shift, which is defined as $f_d = a \times f_c$, is less than $\pm$ 30.5 Hz [110] at $f_c = 29.5$ kHz. To mitigate the maximum Doppler shift a guard band of 77 Hz is considered between the channels.

The duration of each individual tone is called chip duration C_d. Using (3.4), for mobile AUVs with a maximum speed of 7 knots, tone signals with a maximum chip duration of $C_d \approx$ 14 msec can be sent.

In this work, we define the hopping rate to be equal to the symbol rate, as such the chip duration is C_d and is also equal to the symbol duration. Thirteen orthogonal tones are mapped in evenly-spaced tone pairs that span the acoustic frequency bandwidth of 2-kHz of each channel, and each frequency slot width is $F_{sw} = B_w/26$. Effectively, each chip duration is $C_d = 26/B_w$, or $C_d = 13$ msec. Figure 3.5 shows a time-frequency representation of a generic Janus packet for one channel.

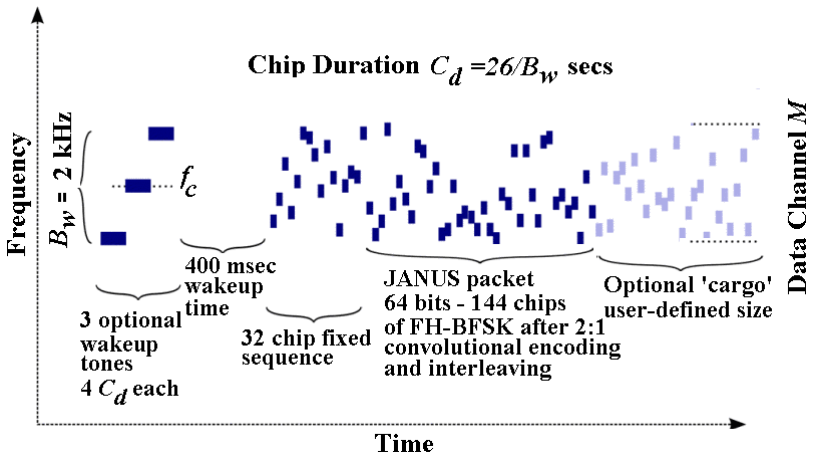

Figure 3.5: The Janus signal for control channel in a time-frequency plot [63]

The proposed FH-BFSK system signal specifications for the control channel are summarized in Table 3.1.

Table 3.1: FH BFSK Signal Specifications

Parameter	**Value**
Number of Channels, M	10
Number of sub carriers in each channel, M_{sub}	26
Sub carriers frequency slot width, F_{sw}	77 Hz
Modulation order,	2
Chip Time, C_d	13 msec
Bits per Symbol, k	1 bpS
Packet Duration , P_s	2,288 msec

Control Packets & Protocol

As described in [62] Collision Avoidance (CA) via Binary Exponential Backoff (BEB) with Global Awareness (GA) consists of an in-band energy detector used to access the CCC. Transmitters are required to sense the CCC before transmission of controlling packets for a minimum of twice the length of an encoded basic controlling packet plus the propagation delay. The control packets are smaller than the data packets and are defined by a 4-bits packet type, an 8-bit node ID and a 12-bit payload. Data corruption is detected by an 8-bit cyclic redundancy check (CRC) which is appended to the packet. These 32 bits with 8 zeros amount to $2 \times (32+8)+32 = 112$ chips after encoding and assuming a fixed preamble of 32 chips. Accordingly, the CCC sensing will last for a DCF interframe spacing (DIFS) equal to $2 \times 112 \times C_d + T_p$ seconds, where T_p is packet propagation delay.

If the CCC is busy when a transmitter intends to transmit, the transmitter continues to sample windows of duration equal to $16 \times C_d$ until the CCC is deemed no longer busy. The transmitter then applies a BEB: it transmits in the next slot with probability $1/(D+1)$, where $D = 2^C - 1$ and C is the number of potential transmissions slots the transmitter has counted in the backoff process in which there has been at least one busy window (C is initialized with $C = 1$). If the transmitter does not transmit in the first available slot, it continues to sample 16 chip windows to detect if the CCC is busy during the next slot. The node increments C by one (but only once per slot) if this is the case at any point during the slot, up to a maximum of $C = 8$. Once the TX node finds the CCC available to transmit its message, C is re-initialized to $C = 1$. If C reaches 8, the attempt to transmit that packet is abandoned.

To allocate the available channels, each TX node senses its surrounding acoustic environment within its range R_T to create a list of available channels (LAC) [111].

The LAC is used by the TX and RX nodes such that they are informed about their individual available channels. In this process, the TX node sends a Request to Send (RTS) packet to the RX node over the CCC. The RTS includes the TX node's LAC list. If the RX node successfully receives the RTS packet and it has at least one free channel for communication, then the RX node replies instantly with a Clear to Send (CTS) over the CCC. The CTS packet is a short message including a clear to send flag for TX node and a backoff time for RX node's neighbors to avoid hidden terminal problem [112].

By receiving the RTS packet at the RX, the RX compares it with the channel states in its LAC. These channel states are represented by a $1 \times M$ vector that consists of binary elements indicating availability. Then, the receiver identifies the common elements of the received RTS channel vector and the corresponding elements of its own LAC channel vector. This results in a List of Confirmed Channels for Transmission (LCCT) which is created at the RX node [113].

The LCCT is also a $1 \times M$ vector in which each element is a binary value representing the available common data channels between the TX and RX nodes. The LCCT is sent by the RX to the TX node. When the TX node receives the LCCT packet from the RX node, it broadcasts this packet to its neighbors on the local CCC to inform them about the data channels that this TX -RX pair wishes to use. After computing and sharing the LCCT information for all TX-RX pairs, the nodes must use the LCCTs to compete for data channels.

For a TX-RX pair i, a matrix $\mathbf{L}_i$ is computed where the j^{th} row of the $\mathbf{L}_i$ matrix is the LCCT of the j^{th} TX-RX neighboring pair to the i^{th} pair. Thus $\mathbf{L}_i$ is a matrix of size $N_i \times M$ where N_i is the number of TX-RX pairs in the neighborhood of pair i.

The proposed MAC layer protocol does not require global synchronization among the ANs, and the contention access mechanism over the local CCC between the neighbors is based on the aforementioned BEB protocol for the Janus Underwater Communications Standard [22].

The packet exchange in the initial phase of a channel allocation process is depicted in Figure 3.6. The MAC protocol proposed employs three control packets : RTS, CTS, LCCT, as well as and the busy tone beacon. The duration of the data frame is T_{max}, its optimal size, depends on the load of the nodes and is heavily influenced by the

BER [68].

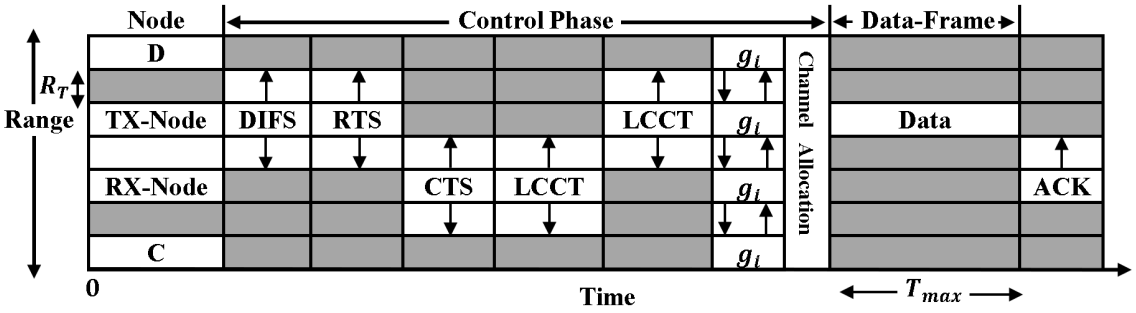

Figure 3.6: Representation of the packet exchange between neighbor nodes. The RX node and Node D are in the transmission range of the TX node while the TX node and Node C are in transmission range of the RX node.

The purpose for the RTS/CTS packets includes (i) reserving the CCC and (ii) solving the hidden terminal problem by making the neighbor nodes aware of an upcoming transmission. Then, the LCCT handshake serves to synchronize the vacant channel information between each TX-RX pair and to prevent collisions between the ANs. Also, it ensures that the TX and RX nodes use the same set of vacant channels for data communication. After the initial negotiation phase is completed, the TX-RX pairs exchange a cost value g_i computed by the proposed algorithm, to assign the available channels to the TX-RX pairs with the lowest cost value. This will be detailed in Section 3.3.1. After assigning the data channel, the transmitter starts sending data over the data channel. While the TX and RX nodes transducers are busy sending and receiving on the data channel, their busy tone beacon generator broadcasts a periodic pulse to inform their neighbors that they are busy on the data channel; this prevents the multichannel hidden terminal problem. Figure 3.7 illustrates the busy tone beacon generated by nodes A and B while communicating on Data Channel 1.

The channel access time during the control phase consists of a negotiation phase and a channel allocation which occurs on CCC. The overall end-to-end latency will be the time between the packet generation and the time of its correct delivery at the destination which includes the channel access time and propagation delay.

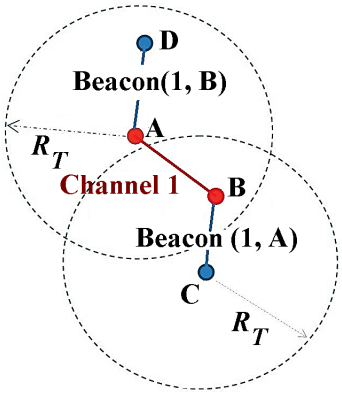

Figure 3.7: The busy tone beacon ensures that Nodes D and C do not send RTS packets to Node A and B while they are communicating on Channel 1.

Graph Model of the Network

In this work the proposed algorithm utilizes the knowledge of the topology and channel sensing to minimize interference among TX-RX pairs during channel allocation. The local relationship between neighbor pairs and their available channels can be simplified into a graph model in which the vertices are TX-RX pairs and the edges represent interference among them. A set of available channels is assigned to each vertex which corresponds to its LCCT. Clearly, if two vertices are connected by an edge, they cannot both access the same channel simultaneously.

Figure 3.8 illustrates a network in which there are five vertices to represent five TX-RX pairs. There are three channels: A, B and C which are opportunistically available for the AN pairs. Due to the sharing agreements, channels that are unavailable, e.g. shadow zones [114], cannot be utilized by ANs within their interference range (labeled I, II, III and IV). Each pair may access a different set of available channels. As shown in Figure 3.8, channels A, B, and C are available for pair 1; channels A and C are available for pair 2, and so on for the rest of the pairs. Note that Figure 3.8 depicts the network status at a fixed time instant.

The model proposed identifies the interference in the network, such that channels cannot be occupied by two neighbor nodes simultaneously. An undirected graph G is used, and represented by $G = (V, E, L)$, where $V = \{v_1, v_1, \ldots, v_N\}$ is the set of vertices representing the TX-RX pairs, E is the set of edges representing interference among neighbor pairs and L is the set of available channels. We use an $N \times N$ matrix

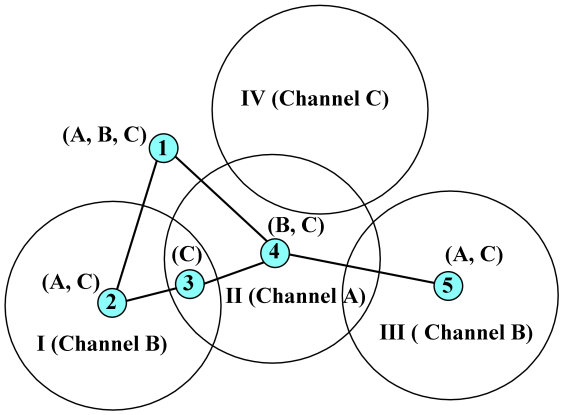

Figure 3.8: Illustration of a neighboring pair's interference using the interference graph.

E to formulate the edge status, where N is the number of TX-RX pairs. At index (i, j) the edge status e_{ij} between two TX-RX pairs i and j is assigned 1 when vertices i and j are neighbors, otherwise it is equal to 0. Based on this definition, G is an undirected graph and effectively the interference matrix will be symmetric. The set of available channels for various pairs are stored in a global $N \times M$ matrix **L**, where at index (i, k), $l_{ik} = 1$ if the channel k is available for the TX-RX pair i and $l_{ik} = 0$ indicates that it is not available. Recall that N is the number of TX-RX neighbor pairs and M is the number of channels. In other words, the i^{th} row represents the LCCT of the i^{th} TX-RX pair. Note that the local matrix $\mathbf{L}_i$ for the TX-RX pair i is a sub-matrix of **L** which contains only those rows of **L** that are corresponding to pair i neighbors.

We denote the set of assigned channels in the entire network by an $N \times M$ matrix **S**, where at index (i, k), $s_{ik} = 1$ if the channel k is allocated to the pair i, otherwise, $s_{ik} = 0$. The i^{th} row of the matrix **S** represents the channels which are allocated to i^{th} pair by the channel allocation algorithm.

The performance metrics of the allocation algorithm can be measured and formulated in terms of **S** and **L**. Similarly to a technique developed in [101], the goal is to maximize the network spectrum utilization S_U defined as

$$\max\left(S_U\right) = \max\left(\sum_{i=1}^{N}\sum_{k=1}^{M} s_{ik}\right) \tag{3.5}$$

subject to

$$s_{ik} \leq l_{ik}, s_{ik} \in 0, 1 \text{ and } s_{ik}s_{jk}e_{ij} = 0.$$

Note that N is the total number of TX-RX pairs and M is the number of channels. Then, for all pairs $i = \{1, \cdots, N\}$ and channels $k = \{1, \cdots, M\}$. Accordingly the optimization variable in the spectrum utilization problem is the number of utilized channels or summation of s_{ik}. The algorithm is also subject to the following fairness and coverage conditions:

1. The channel allocation between all the network pairs should have minimum variance σ^2, where $\sigma^2 = \text{var}(\gamma)$ and channel allocation in the entire network is $\gamma_{1\times N} = [\gamma_1, \gamma_2, \cdots, \gamma_N]$ where γ_i is number of channels allocated to pair i, i.e.

$$\gamma_i = \sum_{k=1}^{M} s_{ik}. \tag{3.6}$$

2. The coverage constraints for pair i are such that $1 \leq \gamma_i$ for all $i = 1 \cdots N$. This guarantees that each pair obtains at least one channel.

In the next section an allocation algorithm which can satisfy the above constraints is proposed. For this purpose, the fairness, the coverage, the channel assignment overhead and network utilization ratio are used as figure of merits.

High Coverage and High Fairness Resource Allocation

In this section, a distributed algorithm that attempts to maximize the network throughput is proposed. The algorithm also ensures allocation of a minimum of one data channel for each TX-RX pairs. The HCHF parameters and variables are summarized in Table 3.2.

The HCHF algorithm is described in six steps as follows:

1. First, each TX-RX pair i acquires its List of Confirmed Channels for Transmission (LCCT) and stores it in its LCCT_i vector.

   To ease the computations, the $N_i \times M$ interference matrix $\mathbf{IM}_i$ is defined and is calculated by applying a logical AND operation between the pair i's LCCT_i vector and every $j \in N_i$ neighbor's LCCT_j vector. The set of available channels

Table 3.2: Parameters for the HCHF Algorithm

R_T	Acoustic nodes transmission range
LAC	$1 \times M$ vector, List of Available Channels
RTS	Request To Send packet
CTS	Clear To Send packet
DIFS	The time duration for which a TX node senses CCC
N_i	Number of TX-RX pairs in the neighborhood of pair i
$\mathrm{LCCT_i}$	$1 \times M$ vector, List of Confirmed Channels for Transmission in which the available common channels between TX and RX nodes are shown by 1 and the rest of channels by 0
$\mathbf{L}_i$	$N_i \times M$ matrix, rows of matrix $\mathbf{L}_i$ is composed of the channels which are available for TX-RX pair i neighbors, e.g. j^{th} row of matrix $\mathbf{L}_i$ is the $\mathrm{LCCT_j}$ of TX-RX pair j^{th} which is in the neighborhood of pair i
T_{max}	Maximum packet duration
C_d	Chip duration
$\mathbf{S}$	$N \times M$ matrix of the entire network channels allocation
γ_i	Number of the channels obtained by pair i
σ^2	Variance of allocated channels to TX-RX pairs
$\mathbf{IM_i}$	$N_i \times M$ interference matrix for pair i
p_i	$1 \times M$ vector of non-contention channels of pair i. It is the set of available channels in the LCCT that cannot be used by neighbors
q_i	$1 \times M$ vector of available channels in LCCT that require contention with the neighbors to be acquired by pair i
$x_i(k)$	Number of neighbors for TX-RX pair i on channel k
g_i	the cost value of pair i to own at least one channel
μ_i	Channel possession threshold, $1 \leq \mu_i \leq \mathrm{sum(LCCT_i)}$, constrains minimum and maximum channels acquisition

in the $\mathrm{LCCT_i}$ that cannot be used by neighbors are called the set of non-contention channels p_i. These channels can be easily identified by considering the zero columns of $\mathbf{IM}_i$ and the corresponding nonzero elements of $\mathrm{LCCT_i}$. Specifically, for each channel of $k \in M$, $p_i(k)$ is set to 1 if the k^{th} column of $\mathbf{IM}_i$ is zero and the k^{th} column of $\mathrm{LCCT_i}$ is equal to 1.

The $1 \times M$ vector p_i initially represents the set of available channels that can be used by the TX-RX pair of i without needing any contention with its neighbors. During the allocation process, as a new channel is assigned to the TX-RX pair i, its corresponding element in p_i is set to 1. As such, at any time, the sum of elements of p_i, γ_i, represents the number of assigned channels to the TX-RX pair i, and as such $\gamma_i = \mathrm{sum}(p_i)$.

Also, for each TX-RX pair i, a $1 \times M$ vector q_i is defined. The vector q_i represents the available channels in the TX-RX pair's $\mathrm{LCCT_i}$ that are common between neighbors. In other words, these are channels that are contentious for assignment between the neighbors. This vector is obtained by comparing the nonzero elements of $\mathrm{LCCT_i}$ with the nonzero columns of $\mathbf{IM}_i$. Effectively,

$$\mathrm{LCCT_i} - p_i = q_i \tag{3.7}$$

The minimum required and maximum allowable number of channels for each TX-RX pair i is set by a threshold μ_i, where $1 \leq \mu_i \leq \mathrm{sum}(\mathrm{LCCT_i})$, and is initialized with $\mu_i = 1$. As such, acquiring at least one data channel is attempted for each TX-RX pair. The threshold μ_i is increased by one if for all $j \in N_i$ neighbors of pair i, $\mu_i < \gamma_j$ or if neighbors of pair i do not have any available channels in their q_j to assign. The TX-RX pair i initiates a negotiation with its neighbors for the channel assignment until there is no channel available in q_i or the threshold μ_i reaches it maximum equal to $\mathrm{sum}(\mathrm{LCCT_i})$. It should be noted that negotiation is only required between neighbors who have interference on certain channels. Furthermore, avoiding network congestion should be considered during the deployment such that the number of neighbors should always be less than the available channels $N_i < M$.

2. Considering that all packet exchanges occur only among neighbors, the following

procedure continues until no available channel can be found to assign for the i^{th} TX-RX pairs' q_i vector:

For each TX-RX pair i with $x_i(k)$ neighbors on a particular channel with $k \in (1, \cdots, M)$, the probability that it is assigned the channel k will be $1/(x_i(k)+1)$. The parameter $x_i(k)$ can be obtained as the sum of the elements of the k^{th} column of $\mathbf{IM_i}$. For each pair i, this probability is calculated to obtain at least one channel. Then g_i, which is defined as the cost value for pair i to obtain at least one channel, is expressed as

$$g_i = 1 - \prod_{\substack{k=1, \\ x_i(k)>0}}^{k=M} \left(1 - \frac{1}{x_i(k)+1}\right) \tag{3.8}$$

As demonstrated in (3.8), it is assumed that the probability of obtaining a given channel is independent of the probability of obtaining other channels.

3. Next, for the j^{th} neighbor of pair i, if the total number of possessed contention free channels are less than the threshold of μ_i (i.e. the sum of the p_i elements is smaller that μ_i) and channel k is available to assign their q_j vector, then all neighbor pairs exchange their g_j values and continue to step 4 otherwise if the sum of the p_i elements is greater or equal to μ_i the pair j give up the petition.

4. After receiving the g_j values from all the neighboring pairs $j \in N_i$, each TX-RX pair i decides if it has the minimum value among the g_j of its neighbors. If so, it selects the available channel with the lowest number, which is identified as the channel k in its contention channel list. It also announces itself and its selected channel to the neighbors by broadcasting a *Channel Allocation* message over the local CCC containing a vector of assigned channels to TX-RX pair i. If two or more pairs have the same values of g_j, the deadlock can be broken by assigning the channel to the pair with the smaller ID. Note that the lowest channel index or node ID is used as a criterion for selection in the algorithm.

5. If the channel k is taken by the pair i, then it sets $p_i(k) = 1$. To avoid reallocation of the channel k to the pair i, this channel is removed from the list of available channels with a contention with pair i, i.e., $q_i(k) = 0$. Then, the

neighboring pairs that interfere with pair i on channel k remove the allocated channel k from their list of available channels with contention. Specifically, $p_j(k)$ is cleared to 0 for all neighbors of the TX-RX pair i.

6. All neighbor pairs update their interference matrices of $\mathbf{IM_i}$ and contention matrices of q_i. Then, until the sum of their assigned channels in p_i reaches the threshold μ_i, the algorithm iterates between steps 2-5. If all pairs reach the threshold of μ_i and there are still some channels in the contention matrix of some pairs, then the threshold variable of μ_i increments by 1 and steps 2-5 are repeated. Otherwise the algorithm ends. Consequently, when the contention matrices of all pairs become empty the allocation algorithm is terminated.

The allocation algorithm is summarized in Algorithm 1. Next, in Section 3.3.1, the algorithm is applied to a realistic underwater deployment.

Resource Allocation Simulation Results

In this section the performance of the proposed HCHF distributed channel allocation scheme is compared with conventional channel allocation techniques in the UWAN framework.

Figure 3.9 illustrates the two-dimensional topology of a distributed network. In this simulation, a maximum of 144 ANs are randomly distributed in a dense area of 2.5×2.5 kilometers to represent a future IoUT application. The total number of available channels are $M = 10$. Each channel occupies an equal bandwidth of 2-kHz between 10.5 kHz and 30.5 kHz. The authors in [115] observe that the probability of establishing an acoustic link in which the SNR is less or equal to a threshold δ is affected by various ambient factors, e.g. shadow zones. In this network model, it is assumed that channels may intermittently be in shadow zones. Here the ratio of number of reliable channels over the total number of channels is assumed to be $\lambda = 0.9$ in different hexagonal areas.

To manage the up-link communication to the surface and effectively reduce the nodes' manufacturing cost and battery supply, UWGs with cellular coverage are demonstrated in Figure 3.9. Initially, UWGs are primary users and have priority to acquire the most reliable channel with highest SNR among $M = 10$ channels. The

1: Initialization: Define the LAC $\forall$ node $\in K$;

Define $LCCT_i$ $\forall$ TX-RX$_i$ $\in N$;

for $i = 1$ *to* N_i **do**
  $\mathbf{L}_i(i,:) = LCCT_i$;
end

for $i = 1$ *to* N_i **do**
  for $j = 1$ *to* N_i **do**
    $\mathbf{IM_i(j,:)} = LCCT_i \ AND \ \mathbf{L}_i(j,:)$
  end
end

for $i = 1$ *to* N_i **do**
  for $j = 1$ *to* M **do**
    if $\mathbf{IM_i}(:,j) = 0 \ AND \ LCCT_i(j) = 1$ **then**
      $p_i(j) = 1$
    end
    if $\mathbf{IM_i}(:,j) \neq 0 \ AND \ LCCT_i(j) = 1$ **then**
      $q_i(j) = 1$
    end
  end
end

2: **while** $q_i = 0 \ OR \ LCCT_i(:) = 0$ **do**
  for $i = 1$ *to* N_i **do**
    for $k = 1$ *to* M **do**
      $x_i(k)$=sum $[\mathbf{IM_i}(:,k)]$
    end
    $g_i(k) = 1 - \prod_{\substack{k=1, \\ x_i(k)>0}}^{k=M} \left(1 - \frac{1}{x_i(k)+1}\right)$
  end
end

3: Exchange g_i AND μ_i

4: **for** $k = 1$ *to* M **do**
  if $sum\ (p_i) < \mu_j \ and \ q_i(k) = 1 \ and \ g_i < min(g_j)$ **then**
    $p_i(k) = 1, \ q_i(k) = 0, \ \forall j \ \in \ N_i$ **then** $q_j(k) = 0$
  end
  if $sum\ (p_i) < \mu_j \ and \ q_i(k) = 1$
  $and \ g_i = \ min(g_j) \ and \ i < j$ **then**
    $p_i(k) = 1, \ q_i(k) = 0, \forall j \ \in \ N_i$ **then** $q_j(k) = 0$
  end
end

5: update interference and contention matrices

6: **if** $\forall j \ \in N_i, \ \forall \ k \in \ M \ sum(p_j) = \mu_i \ and \ sum\ (q_j(k)) \ \neq \ 0$ **then**
  $\mu_i = \mu_i + 1$ and continue form step 2 ;
else
  exit;
end

Algorithm 1: Pseudo-code for HCHF algorithm

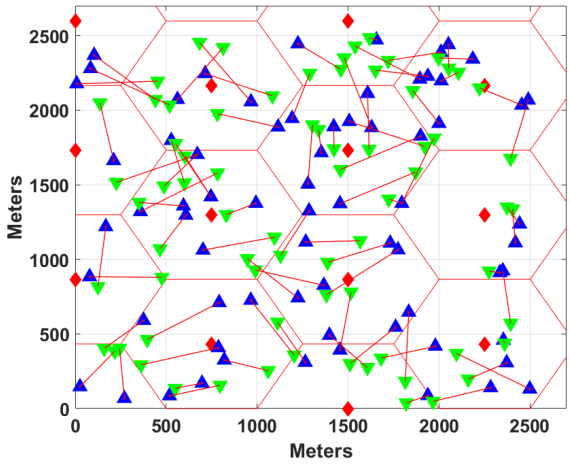

Figure 3.9: Two-dimensional illustration of a network consisting of 72 TX-RX pairs. Green triangles are TX nodes and blue triangles are RX nodes, lines between TX-RX pairs show the corresponding communication links. Red diamonds are UWGs.

UWGs' selected channel is dedicated to communications between ANs and UWGs so it can not be assigned to peer-to-peer communications between ANs. As such, its access scheme is the same as for the CCC. The rest of the 8 available channels can be apportioned among ANs collaboratively.

To represent the propagation conditions, the maximum transmission range of the ANs is approximated to be 500 meters. The proposed algorithm performance is compared with other algorithms by gradually increasing the number of participating ANs from 10 to 144 nodes. In each setting, the allocation algorithm runs one hundred times for randomly scattered nodes, and for each, a new observation of available channels is defined between the ANs. The performance of the algorithms is averaged over one hundred iterations to nullify the impact of the nodes' random scattering on the output of the algorithm.

The Greedy, Random and Link Degree and Round Based Algorithm (LDRA) algorithms [116] are compared with the HCHF algorithm in terms of channel utilization, fairness, network coverage among ANs and allocation process overhead which is measured by averaging the number of controlling packets that are exchanged by each TX-RX pair of ANs during the allocation process.

Figure 3.10 represents the channel utilization, defined as the total number of channels assigned to the TX-RX pairs in the entire network. As expected, the Greedy

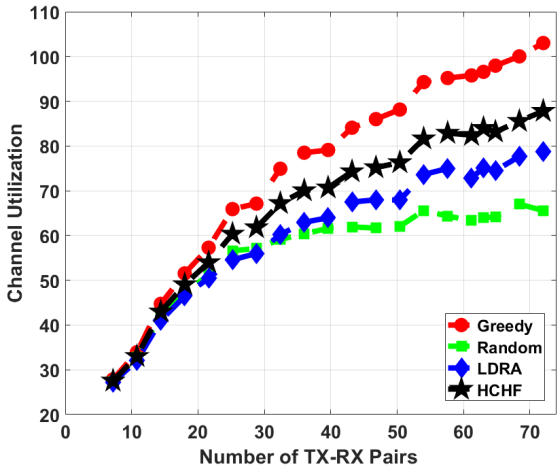

Figure 3.10: Channel utilization of the TX-RX pairs defined as the total number of channels allocated to TX-RX pairs.

algorithm approach can allocate the maximum number of available channels among these algorithms.The Greedy method, in which the channels are allocated to pairs with better conditions, provides the best network utilization. Note that all algorithms perform very differently when the channel demand is increasing. However, in lower AN traffic, they have very similar performance, because there is less contention among the ANs. Note that the R_T can directly affect interference among ANs. Decreasing the R_T decreases the interference. Therefore, it increases the possibility of more allocations and provides a better utilization for all algorithms. However, for a small acoustic range, it will result in network disconnectivity among ANs which is not desired. The simulation results indicate that the HCHF algorithm has a better utilization performance in comparison to the random algorithm and LDRA. The reason is that HCHF attempts to manage fairness without sacrificing the network utilization.

Next, the standard deviation of allocated channels to the TX-RX pairs is used as a metric for comparing the fairness of the allocation algorithms. A large standard deviation means that there is a significant gap between the numbers of channels allocated among different pairs. Figure 3.11 shows that the standard-deviation parameter of HCHF is lower than that of other allocation algorithms. The Greedy algorithm has the highest standard-deviation, and as such, it is very unfair. By increasing the number of TX-RX pairs, the variance of allocations in the HCHF algorithm is converging to its minimum, though from Figure 3.10 it can be seen that HCHF algorithm

channel utilization is high.

The number of TX-RX pairs that have received at least one channel, where the channel possession threshold is $\mu = 1$, is another metric that is used to evaluate coverage. This parameter is also an indication of the network connectivity in multihop relaying scenarios. Figure 3.12 shows the number of TX-RX pairs which have received a minimum of one channel out of all the TX-RX pairs in the network. As can be observed, HCHF can cover the maximum number of ANs.

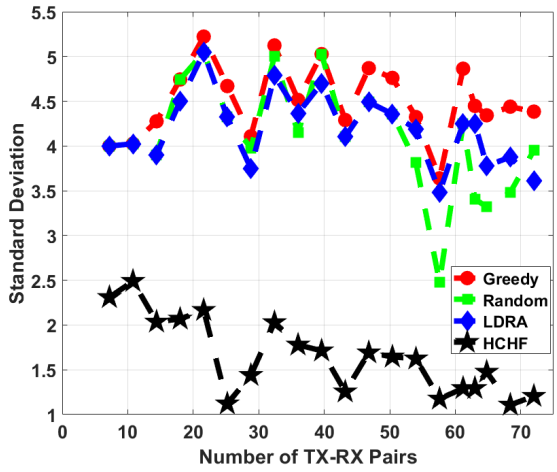

Figure 3.11: Evaluation of the standard deviation of allocated channels.

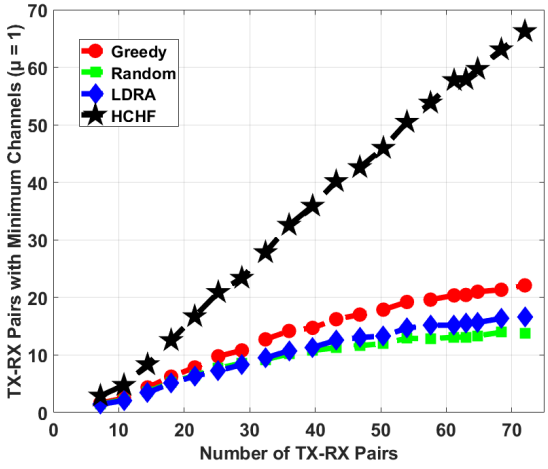

Figure 3.12: Evaluation of the network coverage.

The control packets overhead is defined as the average number of signalling packets transmitted by each TX-RX Pairs to its neighbors during the control phase. In

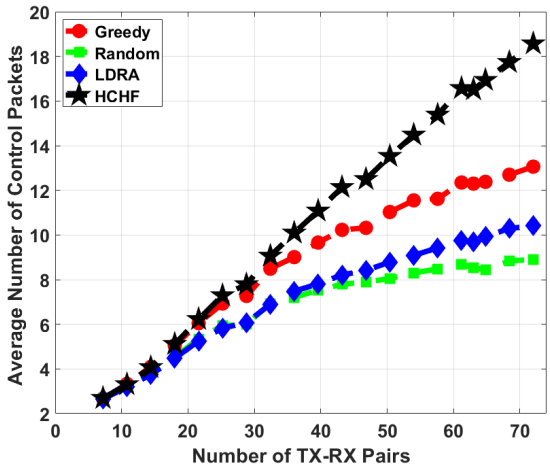

Figure 3.13: Evaluation of average number of control packets submitted by each TX-RX pair during the control phase.

Figure 3.13, the average number of exchanged packets per each TX-RX pair is shown for different algorithms. As the network density increases, the number of neighbor nodes on all the channels increases which imposes more interference on the network. Consequently, to solve the channel assignment problem and avoid collision more controlling packets are needed. It is important to find an optimum network density to avoid excessive congestion and keep the number of controlling packets as low as possible because more controlling packets results in more energy consumption and extreme delay. From Figure 3.13 it can be seen that the control packets overhead distance between HCHF and the other algorithms overshoots when the number of TX-RX pairs in the network exceeds more than 50 TX-RX pairs. In this set-up, a maximum density of 100 ANs per 2.5 $\times$ 2.5 kilometers or 16 ANs per km^2 can be considered as the optimum network density where the HCHF performs efficiently.

3.4 Summary

This chapter first introduces an energy-efficient flooding routing protocol for exchanging network control messages and a channel-aware multihop relaying routing for data transmission. The proposed channel-aware multihop relaying uses a weighting factor based on the predicted CSI to select the optimal next-hop relay. Next, a new distributed channel allocation algorithm for UWANs called HCHF has been described.

The proposed HCHF employs graph coloring for modeling interference constraints among the ANs. The HCHF algorithm ensures that the ANs within the transmitting range of each other do not utilize the same frequency channels and allocates the channels to ANs in a way that allows at least one channel to be assigned to each TX-RX pair. The performance of HCHF algorithm has been compared to that of three existing distributed channel allocation algorithms: the Greedy, Random, and LDRA algorithms. The simulations indicate that HCHF surpasses other algorithms in terms of fairness since it tries to allocate at least one channel to each node. The greedy algorithm tends to maximize channel utilization by sacrificing fairness. The random algorithm has a low throughput, and LDRA offers lower throughput and fairness. It is shown that the improved channel utilization and fairness provided by HCHF are constrained by the overhead of the control packets. Finally, for a reliable and efficient channel assignment in UWANs, an optimum network density should be taken into account to avoid excessive overhead, energy consumption, and access delay on the CCC.

Chapter 4

Statistical Characterization of Underwater Acoustic Channel

This chapter demonstrates the impact of surface elevation variation as a key physical phenomenon on underwater acoustic channel statistics. First a channel model for shallow water environment where tide variations causes flow variations is introduced in Section 4.1; then, in Section 4.2, the model is enhanced by including small-scale statistics imposed by surface elevation variations; in Section 4.3, a data driven parametric model is proposed that quantify the statistical properties of channel characteristics; finally, in Section 4.4, using the sea trials data set the correlation between the surface elevation variations and channel characteristics is evaluated.

4.1 Analytical Channel Model

4.1.1 Large-scale Time Varying Channel Model

In this section, a channel model based on the model in [6] is developed to represent a high-flow shallow environment and takes into account tidal flow. A deployment between a fixed acoustic source and acoustic recorders held in the Bay of Fundy for 34 days will serve as a use case to the channel model.

As per [11], a time varying multipath acoustic channel impulse response is expressed as

$$h(\tau, t) = \sum_{p=1}^{P} h_p(t)\delta(\tau - \tau_p(t)) \tag{4.1}$$

where $h_p(t)$ is the large-scale amplitude, P is the total number of distinctive propagation paths and $\tau_p(t)$ is the large-scale delay for path p. As first observed in [117], the path amplitudes and delays vary with time: their instantaneous value depends on the distance traveled as well as the physics of propagation, including Snell's law, the channel geometry, the bathymetry composition and sound speed profile [118].

The time varying large-scale gain of path p derived in [6] is expressed as

$$h_p(t) = \overline{h}_P \frac{1}{\sqrt{\left(1 + \frac{\Delta l_p(t)}{l_p}\right)^k \alpha_p(f)^{\Delta l_p(t)}}}, \tag{4.2}$$

where $\bar{h}_p$ is the nominal path gain and $\Delta l_p(t) = l_p(t) - \bar{l}_p$ describes the variations of the path length in unit of meter. Accordingly, $l_p(t)$ is the large-scale path length and $\bar{l}_p$ represents the nominal path length, $\alpha_p(f)$ is the absorption loss coefficient for path p within the signal frequency in dB/km, and k is the spreading factor [38].

Assuming no reverberation, the nominal path length $\bar{l}_p$ can be calculated using a ray-tracing algorithm such as Bellhop [34]. Figure 4.1 represents the dominant nominal paths and Figure 4.2 represents the transmission loss, obtained using Bellhop, representative of a deployment scenario in the Bay of Fundy, Nova Scotia.

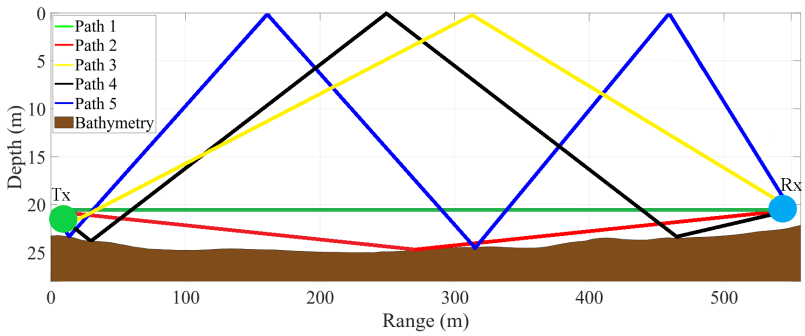

Figure 4.1: Nominal dominant paths between the transmitter and the receiver representing a 566 meter channel in Bay of Fundy. The transmitter is fixed at the depth of 20.5 m and receiver's hydrophones are fixed at 22 m.

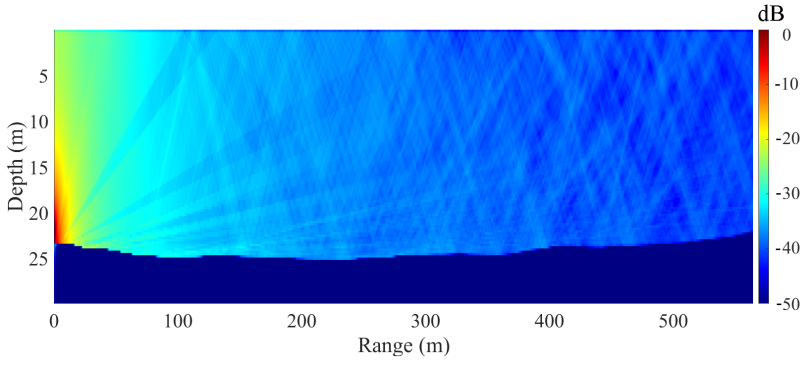

Figure 4.2: Illustration of a 566 meter nominal channel gain (dB) using Bellhop.

For path p of a channel in a mobile system, assuming a nominal delay $\bar{\tau_p} = \bar{l}_p/\bar{c}$ at time $t = 0$, the large-scale delay of path p, $\tau_p(t_0)$ at time t_0 can be defined as

$$\tau_p(t_0) = \bar{\tau_p} - \int_{t=0}^{t_0} a_v(t)dt, \tag{4.3}$$

where $\bar{c}$ is the average sound speed experienced by path p while traveling from transmitter to receiver. The term $\int_{t=0}^{t_0} a_v(t)dt$ describes the delay due to the overall motion during an observation period of t_0 seconds corresponding to few seconds or several symbols transmission. The system motion induced Doppler scaling factor is modelled by $a_v(t)$ [13] corresponds to the linear path length variation with equivalent receiver's linear drifting speed of v_{dp} longitudinal to the propagation path. The linear Doppler scaling factor is defined as

$$a_v(t) = \frac{v_{dp}(t)}{\bar{c}} \tag{4.4}$$

For the scenario involving a mobile transmitter or receiver as depicted in Figure 4.3 the relative speed v_{dp} associated to the path p is

$$v_{dp} = v_{td}\cos(\theta_p - \theta_{td}) - v_{rd}\cos(\theta_p + \theta_{rd}) \tag{4.5}$$

Note that v_{td} is the transmitter vehicular speed in the direction of θ_{td} with respect to the horizontal point toward the receiver, and v_{rd} is the receivers vehicular speed in the direction of θ_{rd} with respect to the horizontal point toward the transmitter. Also, θ_P is the grazing angle associated with the p^{th} propagation path [6].

In a high flow environment, let's define a nominal sound propagation velocity $\bar{c}$ that is approximately constant as a function of depth and range, a mean flow speed c_f parallel to the propagation channel that varies as a function of tide phase, and a turbulent flow component c_t that is range and depth dependent. Then, assuming no reverberation, the travel time $\bar{\tau_P}$ for the line of sight (LOS) between the transmitter and the receiver situated at a distance d from the receiver is defined as

$$\bar{\tau_p} = \frac{\bar{l_p}}{\bar{c} + c_f + \mathrm{E}[c_t]}, \tag{4.6}$$

where $\mathrm{E}[\cdot]$ is the mean operator. The turbulent flow induces a variability in the time of arrival for each transmission between the transmitter and receiver. This phenomena

will be studied in Section 4.3. It will be demonstrated using measurements that the flow induces significant transmission loss variations as well as delay spread variations on the propagation channel.

Next, the small-scale fading coefficient will be characterized with intrapaths statistics and the small-scale fading properties will be explained.

4.1.2 Small-scale Fast Fading Channel Model

Scattering and refractions from the sea surface produce small-scale fading variations and play a key role in the randomness and short coherence time of the channel; these conditions impose rapid fluctuations in the received signal strength over a very short period of time [11]. In this section, random small-scale path coefficients will be reviewed.

To extend the large-scale model to a small-scale model in a discreet time-domain, each dominant path is assumed as a bundle of intrapaths within a limited scattering field. The transmitted signal can be assumed as rays that are received in clusters of arrivals with a mean propagation delay of τ_p [39].The different phenomena that can cause small-scale effects are relative motion in the channel, including surface and bottom variations and scattering from surface and objects. To study small-scale time varying acoustic channel characterization, we adopt the time varying transfer function of the channel $H(f,t)$ between a mobile transmitter and a receiver in a typical UWA channel as derived in [38].

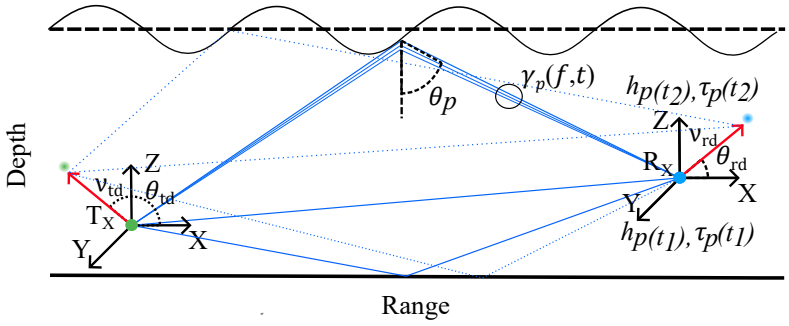

Figure 4.3: Channel geometry between a transmitter and a receiver.

Figure 4.3 depicts a snapshot of a time varying multipath channel between two mobile nodes at a particular discrete-time observation $t \in T$. The channel time

varying transfer function can be expressed as [38]

$$\begin{aligned} H(f,t) &= \sum_{p}\sum_{i} h_{p,i} e^{-j2\pi f \tau_{p,i}}, \\ &= \sum_{p} h_p(t) e^{-j2\pi f \tau_p(t)} \gamma_p(f,t) e^{-j2\pi f a_{flow}(t)}. \end{aligned} \tag{4.7}$$

where $h_{p,i}$ is the gain of intrapaths within cluster p, and $\tau_{p,i} = \tau_p + \delta_{\tau_{p,i}}$ are the intrapaths small-scale delays. The small-scale fading is characterized over the signal bandwidth using the random fading coefficient $\gamma_p(f,t)$ for cluster p as introduced in [10]. We assume that all the signal energy in path p is scattered into N intrapaths where $c_{p,i}$ are intrapaths small-scale coefficients, $\sum_{i=1}^{N} |c_{p,i}| = 1$. Accordingly, the small-scale fading coefficient of path p can be expressed as

$$\gamma_p(f,t) = \sum_{i \geq 1} c_{p,i} e^{-j2\pi f \delta_{\tau_{p,i}}}, \tag{4.8}$$

The distribution of random small-scale path coefficient $\gamma_p(f)$ during the period of Δt depends on intrapaths random scattering coefficients and delays which are influenced by environmental conditions such as surface roughness and flow.

In Section 4.3, probability density functions (PDFs) of intrapaths gain $h_{p,i}$ and relative delay $\delta_{\tau_{p,i}}$ will be obtained from the channel measurements in Grand passage, Nova Scotia. Statistical properties of intrapaths amplitude $c_{p,i}$ and phase $2\pi f \delta_{\tau_{p,i}}$ vary in different sea states or tide phases, hence, the fading coefficient statistical properties varies over time.

In a tidal environment, the flow variation induces additional small-scale variations. The non-linear Doppler scaling factor $a_{flow}(t)$ describes the motions imposed on the channel in high flow environment during different tide phases. An empirical relationship between the tide height in different tide phases Δh, and flow velocity can be calculated empirically to estimate the non linear Doppler scaling factor linearly in discrete tide phases. A polynomial fit to the measured flow and Δh can estimate the coefficients a_2, a_1 and a_0 of the mean flow, c_f [119].

$$c_f = -a_2 \Delta h^2 + a_1 \Delta h + a_0. \tag{4.9}$$

$$a_{flow} = \frac{c_f}{\bar{c}} \tag{4.10}$$

4.1.3 Quantifying the Channel Characteristics

In this section, the procedure to extract the time varying CSI characteristics from a sequence of CIRs is reviewed. Note that the CIRs can be obtained by simulation or through measurements.

To calculate the channel gain over a bandwidth B, the sequence of CIRs are obtained at discrete time intervals t_n, each with duration of Δt seconds. Considering the frequency selective channel transfer function $H(f, t_n)$ at time $t_n \in T$ and $T = \{t_0, t_1, \cdots, t_k\}$, the instantaneous channel gain $g(t_n)$ at time realization t_n can be calculated from

$$g(t_n) = \frac{1}{B} \int_{f_0}^{f_0+B} |H(f, t_n)|^2 df, \tag{4.11}$$

By averaging the instantaneous channel gain over longer large-scale interval $t \in [0, t_n]$ or several seconds we can obtain large-scale channel gain

$$G = E\{g(t)\} \tag{4.12}$$

The time dispersive properties of wide band multipath channels are most commonly quantified by their mean excess delay $\bar{\tau}$ and root mean square (RMS) of delay spread τ_{RMS}. Each cluster of arrivals has different dispersion properties. We can define the RMS delay spread τ_{RMS} for cluster path p as

$$\tau_{\text{RMS}_p} = \sqrt{\bar{\tau_p^2} - (\bar{\tau_p})^2}, \tag{4.13}$$

where

$$\bar{\tau_p^2} = \frac{\sum_i {h_{p,i}}^2 \tau_{p,}, i^2}{\sum_i {h_{p,i}}^2} \quad , \quad \bar{\tau_p} = \frac{\sum_i {h_{p,i}}^2 \tau_{p,i}}{\sum_i {h_{p,i}}^2}, \tag{4.14}$$

The maximum excess delay of the power delay profile for path p is defined to be the time delay during which multipath energy falls to X dB below the maximum. The maximum excess delay can be written as $\tau_{p,n} - \tau_{p,0}$, where $\tau_{p,0}$ is the first arrival and $\tau_{p,n}$ is the last intrapath and all n intrapaths gain are within X dB of the strongest arrival

gain. For the rest of this paper the RMS delay spread term is simply abbreviated to delay spread.

As explained in [6], by assuming a Gaussian distribution for $\delta_{\tau_{p,i}(t)}$ which obeys a first order autoregressive process (AR-1)

$$\delta_{\tau_{p,i}(t+\Delta t)} = e^{-\pi B_{\delta p}\Delta t}\delta_{\tau_{(p,i)}(t)} + \omega_{\delta_{\tau_{p,i}}}(t) \tag{4.15}$$

where $B_{\delta p}$ is 3-dB width of the PSD of $\delta_{\tau_{p,i}(t)}$ and $\omega_{\delta_{\tau_{p,i}}}(t)$ is Gaussian distributed with zero mean, the effective Doppler spread of each path p can be approximated by standard deviation of intrapaths delay, represented by σ_{δ_p} and $B_{\delta p}$.

$$B_p(f) = (2\pi f\sigma_{\delta p})^2 B_{\delta p}, \tag{4.16}$$

which implies that the Doppler bandwidth for cluster p is proportional to variance of intrapaths delays.

The channel model variables are summarized in Table 4.1. Next, the effect of surface elevation variations in variance of intrapaths statistics will be demonstrated.

Table 4.1: Summary of small-scale fading variables

Variable	**Definition**
$h_p(t)$	Time varying large-scale path gain
$h_{p,i}$	Small-scale intrapath gain
$\tau_p(t)$	Time varying large-scale delays
$\tau_{p,i}(t)$	Small-scale intrapath delays
$\gamma_p(f,t)$	Small-scale path coefficient
$\delta_{\tau_{p,i}}(t)$	The path p relative random intrapath delays with standard deviation of $\sigma_{\delta p}$
$c_p(f,t)$	The path p intrapath Small-scale path coefficient
$B_{\delta p}$	3 dB width of the PSD of path p intra-path delays
$B_p(f)$	The effective Doppler spread or Doppler bandwidth of a path P

4.2 Influence of Surface Elevation

Surface elevation variations are among the leading environmental parameters that contribute to the small-scale effect and rapid fluctuations of the UWA signal in a

short period of time on the order of tens of milliseconds [120]. Various factors can cause sea surface roughness; the gravity effect can form standing waves; tidal flow can cause sinusoidal waves [121]; wind can induce breaking waves with Rayleigh elevation variation distribution [122]. Also, turbulence generated by shear flow can roughen the water surfaces [123] and outweigh wind-dependent elevation variation.

Understanding the correlation between time-evolving sea surface variations and channel characteristics presents an efficient approach for predicting CSI. There are two well-known theoretical methods for calculating acoustic scattering from rough surfaces. One is based on the small roughness perturbation approximation or Rayleigh-Rice approximation [124] and the other is based on Kirchhoff or physical optics approximation [125]. The perturbation approach is valid when root-mean-square (rms) of surface height (trough to crest) is small compared to the acoustic wave length $h/\lambda < 1$. On the contrary the Kirchhoff approximation is generally assumed for surfaces on which the scattering field curvature radius is larger compared to acoustic signal wavelength, $h/\lambda > 1$ and applicable to moderate-to-high frequency acoustic signals [126].

Next, the role of surface elevation variation on the intrapaths delays and scatterings coefficients statistics is demonstrated. In order to obtain statistics of intrapath delays and scattering coefficients, we use a ray-tracing approach and Kirchhoff approximation for acoustic scattering from rough surfaces.

Intrapath Delays Statistics

According to the rough surface scattering theory [127], roughness and time varying properties of ocean surface cause variation in the length of the intrapaths scattered from the surface. In this work, the surface wave height is assumed to be a wide-sense stationery process during a sea state which lasts for a prolonged period spanning several minutes or one tide phase. The tide period is discretized into 25 different phases and it is assumed that the surface height variance remains relatively constant during each tide phase [128].

During each tide phase, consider Figure 4.4 where point A is the nominal flat ocean surface level at $z = 0$, $f(x, t)$ is the surface variation process and the distance l_p corresponds to the nominal length of the path p. It is assumed that at a snapshot

in time, the point A' is $\Delta z = f(x,t) \cdot \mathbf{z}$ meter lower than A in the vertical direction from which the intrapath i is scattered.

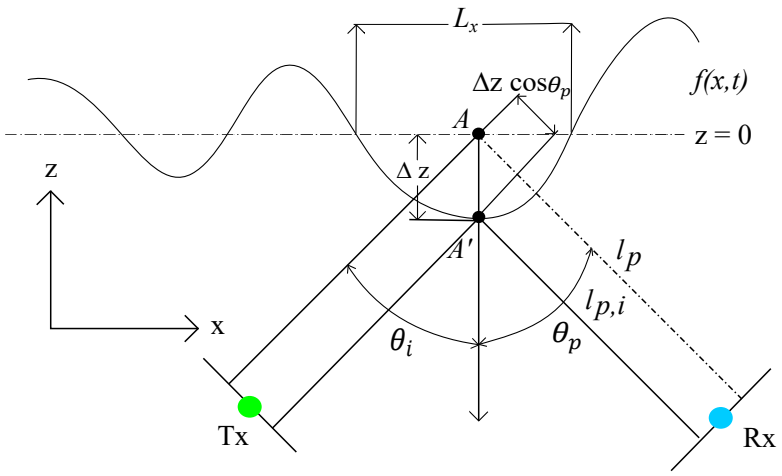

Figure 4.4: Path length variation approximation.

Both spatial and temporal variations from the nominal reflecting point A cause fluctuation in the intrapath length, $l_{p,i}$. The path length variations $l_{p,i}$ at a given moment can be approximated by

$$\Delta l_{p,i} = (l_p - l_{p,i}) = 2 \times \Delta z \cos\theta_p, \tag{4.17}$$

where θ_p is the grazing angle of the p_{th} path.

During one tide cycle (12 hours and 25 minutes) the envelope of a single sine surface wave in the presence of narrowband Gaussian noise has approximated by a Rayleigh-Rice distribution [129]. However, as will be shown by tide analysis in Section 4.4, during a single tide phase (approximately 30 minutes), when the surface process consists of a large number of randomly phased sine waves and Gaussian noise, the sums of their in-phase and quadrature components are nearly Gaussian random variables. Hence, during our defined tide phase the ocean surface height variation process $z = f(x,t)$ can be modeled by a Gaussian process [130], where $f(x,t)$ is the surface process function with scattering field of L and scattering points intervals of Δx.

Thus, using the Gaussian PDF of the random surface elevation with the Pierson Moskowitz (PM) spectrum, and the dispersion relation provided in [122] we can

express the PDF of surface elevation variations using

$$p(\Delta z) = \frac{1}{h\sqrt{2\pi}} \exp\left(-\frac{(\Delta z)^2}{2h^2}\right), \tag{4.18}$$

where h is the RMS height of the ocean surface from trough to crest.

The intrapaths delay $\delta\tau_{p,i}$ is a random variable and follows a distribution $p(\delta\tau_{p,i})$ which accounts for the random placement of scattering points within scattering field. Only statistical characteristics of intrapaths scattered from the surface field of L_x are considered here, which account for the majority of small-scale effect. Although, scattering fields can be at the surface, bottom, or any other object in the propagation path, to simplify the model, Gaussian-distributed displacements of scattering points are considered as the cause of Gaussian-distributed intrapath delays. Accordingly, variations in intrapaths propagation delay can be described as

$$\delta_{\tau_{p,i}} = \frac{\Delta l_{p,i}}{\bar{c}} = \Delta z \frac{2 \times \cos\theta_p}{\bar{c}}, \tag{4.19}$$

where $\bar{c}$ is the overall sound speed experienced by the signal along the path p. Thus, the intrapath delay variation probability $p(\delta\tau_{p,i})$ can be defined by the Gaussian PDF defined by

$$p(\delta_{\tau_{p,i}}) = \frac{\bar{c}}{2h\cos\theta_p\sqrt{2\pi}} \exp\left(-\frac{\delta^2_{\tau_{p,i}}\bar{c}^2}{8h^2\cos^2\theta_p}\right). \tag{4.20}$$

The random path length variation caused by the first bounce off the surface is normally distributed, i.e. $\Delta l^1_{p,i} \sim N(\mu_1, \sigma_1^2)$. Assuming that the surface elevation variation for the first bounce and second bounce are uncorrelated, then their sum is also normally distributed with a mean being the sum of the two means, and a variance being the sum of the two variances. This can be extended to n bounces off the surface [131]. When there are n_s bounces off the ocean surface and the scattering points are far from each other and uncorrelated intrapaths propagation delay for path p can be described as

$$\begin{aligned}\delta_{\tau_{p,i}} = \frac{\Delta l^n_{p,i}}{\bar{c}} = \Delta z_1 \frac{2 \times \cos\theta_{p1}}{\bar{c}} + \Delta z_2 \frac{2 \times \cos\theta_{p2}}{\bar{c}} + ... \\ + \Delta z_n \frac{2 \times \cos\theta_{pn_s}}{\bar{c}},\end{aligned} \tag{4.21}$$

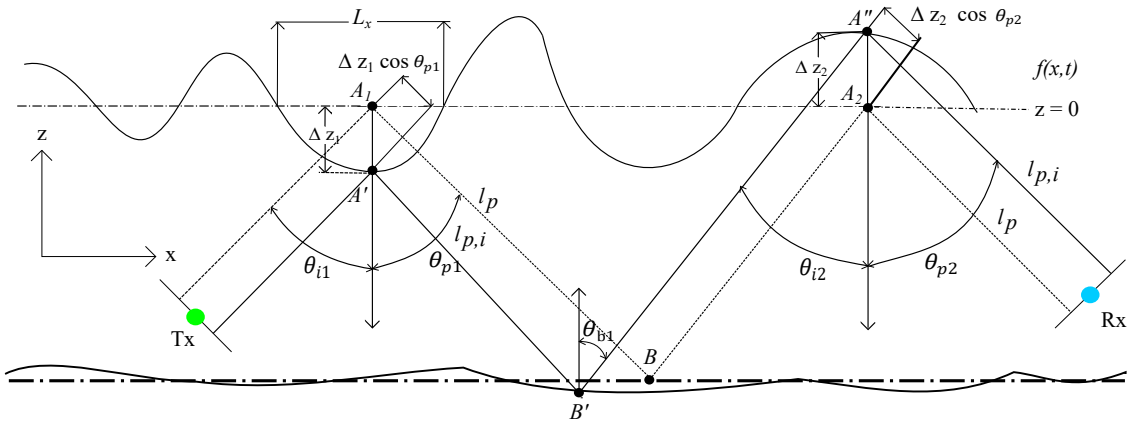

Figure 4.5: Path length variation approximation for modelling of the fluctuation with two bounces off the surface.

where Δz has a zero mean Gaussian distribution with variance $\sigma^2_{\Delta z}$ and the grazing angles are equal to θ_p. Then, the jointly Gaussian distribution of random variables in the right side of (4.21) is Gaussian and the intrapath delays variances is additive. Similarly, by taking into account the bottom variation with the variance of Δb and n_b number of bounces from the bottom with grazing angles of θ_b, the variance of the delay becomes

$$\sigma^2_{\delta_p} = \frac{n_s \sigma^2_{\Delta z}}{\bar{c}^2}(2\cos\theta_p)^2 + \frac{n_b \sigma^2_{\Delta b}}{\bar{c}^2}(2\cos\theta_b)^2, \tag{4.22}$$

where n_s is the number of surface bounces and n_b is the number of bottom bounces along the path p. Note that the bottom variations can be negligible comparing to the surface. Then we have

$$\sigma^2_{\Delta z} = \left[\frac{\sigma_{\delta_p}\bar{c}}{2\cos\theta_p}\right]^2 \tag{4.23}$$

Scattering Coefficients Statistics

Here, we derive the relation between the intrapaths scattering coefficients and surface variations. The intrapaths scattering coefficients $c_{p,i}(t)$ due the time varying ocean surface process $f(x,t)$ in Figure 4.4 can be approximated based on the Kirchhoff approximation (KA) [130, 132] and defined as

$$c_{p,i}(t) = \frac{\sec\theta_i}{L_x} \times \frac{1+\cos\left(\theta_i+\theta_p\right)}{\cos\theta_i+\cos\theta_p} \times \int_{-L_x/2}^{L_x/2} e^{j2\pi f \nu . r(t)} dx, \tag{4.24}$$

where ν is

$$\nu = \frac{N.[(\sin\theta_i - \sin\theta_p)x - (\cos\theta_i + \cos\theta_p).z]}{L_x \bar{c}}, \tag{4.25}$$

and $r(t)$ is defined as

$$r(t) = x \cdot \mathbf{x} + f(x,t) \cdot \mathbf{z}. \tag{4.26}$$

Note that L_x is the length of the scattering field which is usually assumed to be a few times the signal wavelength [6] and $N = L_x/\Delta x$ is the total number of scatterers from the surface. Also, $\mathbf{x}$ and $\mathbf{z}$ are unit vectors along the x- and z-axis, respectively. Assuming $\theta_i = \theta_s$, we can approximate (4.24) as

$$c_{p,i}(t) = \frac{1}{N} e^{j4\pi f cos(\theta_p).\Delta z/\bar{c}}, \tag{4.27}$$

The scattering coefficients $c_{p,i}(t)$ are a random variable with normalized unit power. Since Δz has normal distribution we can infer that $c_{p,i}(t)$ process follows a log-normal distribution.

This demonstrates that the intrapath statistical properties and its correlation to the surface elevation variation can be used to express the channel path p small-scale properties in terms of surface elevation variations in different sea states or tide phases.

In practice the variance of the surface elevation variations and also the angle of θ_p varies by environmental conditions, e.g. tide phases. For a realistic propagation model, the path statistics to determine the small-scale fading coefficient parameters should be inferred from physical phenomena.

Next, we will present a data-driven method to obtain statistics of intrapaths gain and delay profile.

4.3 Experimental Data Analysis Using A Parametric Data-driven Model

This section focuses on a data-driven model to identify the statistical properties of intrapaths and obtain key channel characteristics. First, the experimental setup and

procedure to extract the time varying channel in the unique deployment environment is described in Section 4.3.1. Then, in Section 4.3, a parametric data-driven model [133] is presented, which identifies the channel characteristics and intrapaths statistics. Finally, in Section 4.4, the correlation between the different tide phases and channel characteristics is analyzed.

4.3.1 Deployment Conditions and Probing Sequences

The acoustic recordings and Acoustic Doppler Current Profiler (ADCP) data used in this work were collected by Jasco Applied Sciences during a 34-day measurement campaign from September 22, 2018, to October 26, 2018. As detailed in [134], three acoustic omni-directional recorders and an acoustic projector were deployed at the project sites. The acoustic projector on mooring was a six-inch spherical projector type M18C-6.0 from Geospectrum Technologies. It was mounted above one of the high-flow moorings. The acoustic transmission experiment was carried out in Grand Passage, Nova Scotia, which is a narrow tidal channel with high flow and turbulence.

Figure 4.6 shows a map of the deployment area in Grand Passage. The acoustic projector (SS) is placed on the bottom of Grand Passage at a depth of 23 meters. The receiver sensor arrays are comprised of four omni-directional hydrophones mounted on JASCO Applied Sciences' Autonomous Multichannel Acoustic Recorders (AMAR). The three distances for AMAR A, AMAR B, and AMAR C from the acoustic projector are 76.6, 566, and 1078 meters respectively, as shown in Figure 4.6. Each AMAR samples at a rate of 64 kHz, and the sensors have an effective bandwidth of 32 kHz. The transducer source level (SL) is 180 dB re 1V/μPa, and at the receiver the hydrophone sensitivity is -204 dB re 1V/μPa. The propagation channel between the projector and the receivers is approximately parallel to the direction of flow in the area.

Table 4.2 shows coordinates of the projector and receivers. The bathymetry and transmission loss between the transmitter and the three receivers is shown in Figure 4.7 with a maximum depth of around 23 meters, and a minimum depth of approximately 14 m. The bottom composition in Grand Passage consists of mostly gravel and sand for the first 700 meters between the transmitter and receiver, and beyond this distance, it is composed of glacial till. Note that the transmission loss is

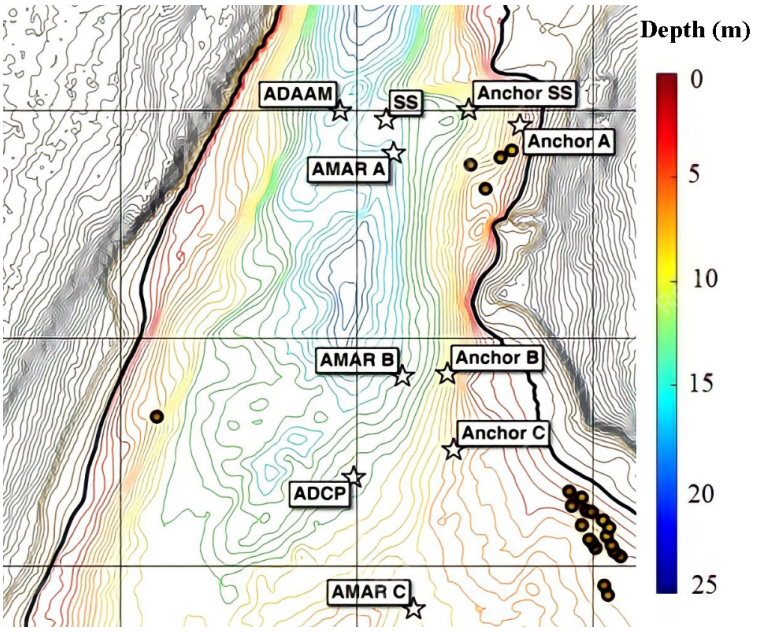

Figure 4.6: Map of Grand Passage deployment showing the depth and location of equipment. The equipment includes an Acoustic Doppler Current Profiler (ADCP) by Dalhousie University; and three Autonomous Multichannel Acoustic Recorders (AMAR's) by Jasco Applied sciences.

simulated using Bellhop's ray-tracing model.

Table 4.2: Projector and hydrophones deployment

	Latitude	Longitude	Depth (m)	Range (m)
SS	44°16.576'N	66°20.323'W	20.5	0
A	44°16.536'N	66°20.309'W	21	76
B	44°16.272'N	66°20.280'W	22	566
C	44°15.998'N	66°20.246'W	11	1078

Since the ADCP flow and pressure measurement data were only recording for 14 days, an extrapolation method performed to quantify the flow and tide height over the entire 34-day sea trial. Linear combinations of sinusoids with unknown amplitudes, frequencies, and phases were fit to the collected tide height data. Accordingly, the best fit function was extrapolated over the 34 day period as shown in Figure 4.8.

The extrapolated flow velocity was calculated from an empirical relationship between the differential tide height Δh as function of discrete-time, sampled every 30 minutes, and the measured velocity. Using a polynomial fit between the measured flow and Δh the mean flow, $\hat{c}_f$, is estimated to be

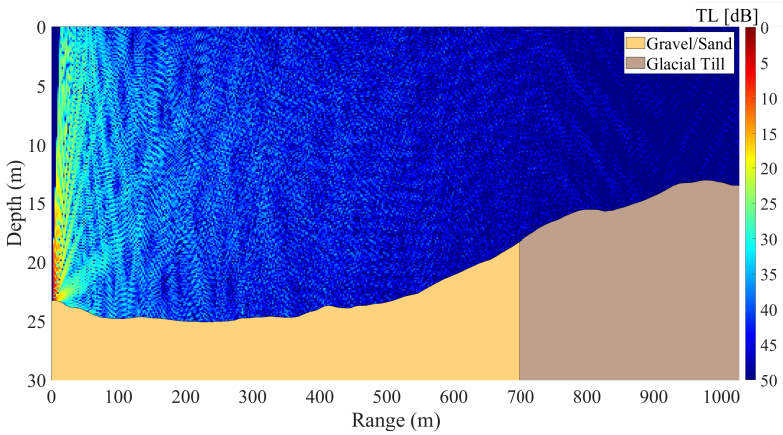

Figure 4.7: Transmission loss and bathymetry in Grand Passage.

$$\hat{c}_f = -29.37\Delta h^2 + 17.17\Delta h + 0.297. \tag{4.28}$$

The best fit flow model is a quadratic function of tide derivative Δh. The extrapolated flow $\hat{c}_f$ and tide variation Δh are calculated over all 34 days, with 83% of the observations falling within the 95% confidence intervals. The tide current velocity is shown in Figure 4.8.

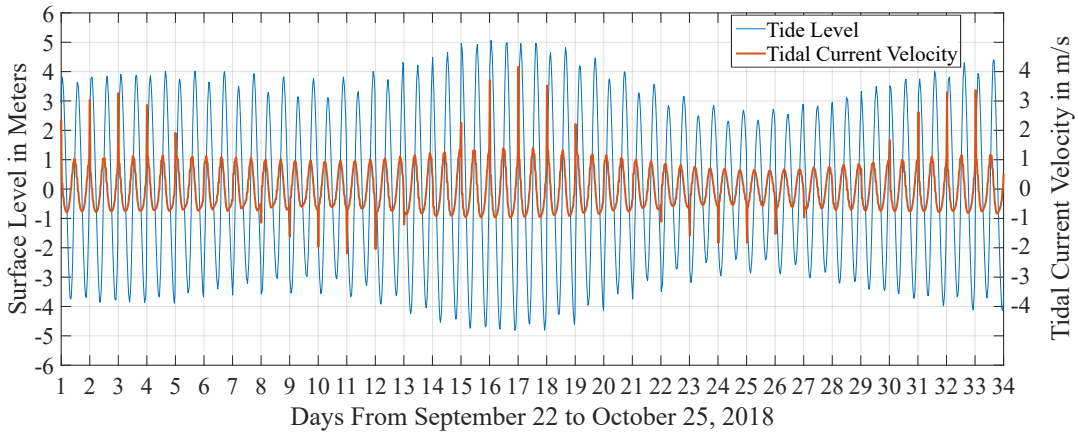

Figure 4.8: Extrapolated tide and flow variation in Grand Passage, Nova Scotia, from Sep. 22, 2018 to Oct. 25, 2018.

During the experiment, the channel was probed at a regular period to obtain the channel conditions over 34 days. Specifically, every thirty minutes, the sound projector emitted a sequence of known signatures, which were recorded at the three receivers. A set of probing sequences spanning a broad frequency range between

8-16 kHz was transmitted. Each probing sequence incorporated nine consecutive one-second linear frequency modulated (LFM) up-chirp tones and nine consecutive one-second LFM down-chirp tones, spanning a bandwidth of 8 kHz, centered at a carrier frequency of 12 kHz as well as four continuous ten-second 8 kHz, 10 kHz, 12.5 kHz, and 16 kHz tones. A 10 second linear up-sweeping frequency modulated pulse from 8-16 kHz and a 10 second linear down-sweeping frequency modulated pulse from 16-8 kHz is also transmitted to study transmission loss. Figure 4.9 shows the received signals at AMAR B in high and low flow in which between approximately 0.6-and and 0.8 seconds, nine consecutive up-chirps are transmitted. Then, between 1 and 1.2 seconds, nine consecutive down-chirps are transmitted.

It should be noted that every 30 minutes, a ferry transports passenger cars between Briar and Long Islands. This ferry produces significant acoustic noise in the channel from its propeller. There is also a large population of marine animals in the area, which includes harbour porpoises, whales, and an occasional orca spotting. Since an acoustic source was deployed for the duration of the trials, a marine assessment was conducted before the trials to ensure that no harm would come to the animals.

After frame synchronization, the channel estimations are determined using the cross-correlation between the transmit and received sequences. The reference LFM up-chirp $x_{up}(t)$ is expressed as

$$x_{up}(t) = e^{-j2\pi\left(\frac{B}{2T_S}t^2 + f_0 t\right)}, \tag{4.29}$$

while the down-chirp $x_{dn}(t)$ is expressed as

$$x_{dn}(t) = e^{j2\pi\left(\frac{B}{2T_S}t^2 - (f_0+B)t\right)} \tag{4.30}$$

The signals $x_{up}(t)$ and $x_{dn}(t)$ are used to cross-correlate with the received LFM signals, $y(t)$. Note that B is the signal bandwidth in Hertz, T_s is the tone duration in seconds, $f_0 = 8$ kHz is the fundamental frequency in Hertz, and t is the signal time in seconds.

The received signal $y(t)$ is cross-correlated with the reference signals $x(t)$ to determine an estimate of the channel impulse response $\hat{h}(\tau)$, expressed as

$$\hat{h}(\tau) = \int_0^{T_s} x(t-\tau)^* y(t) dt \tag{4.31}$$

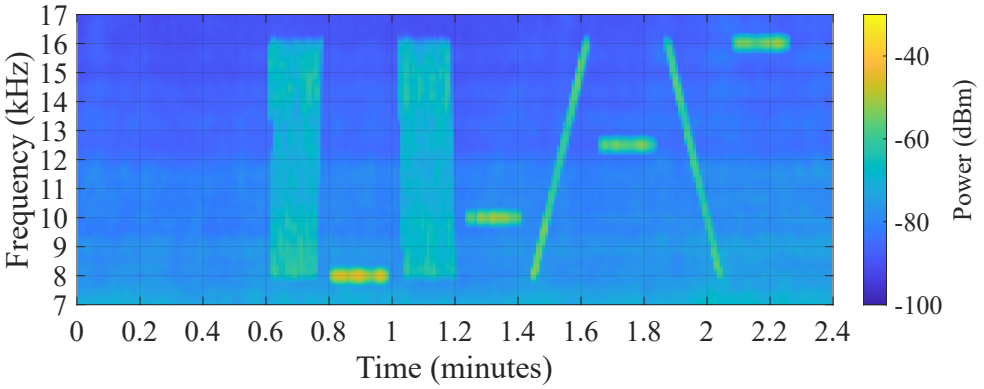

(a) AMAR B at low flow.

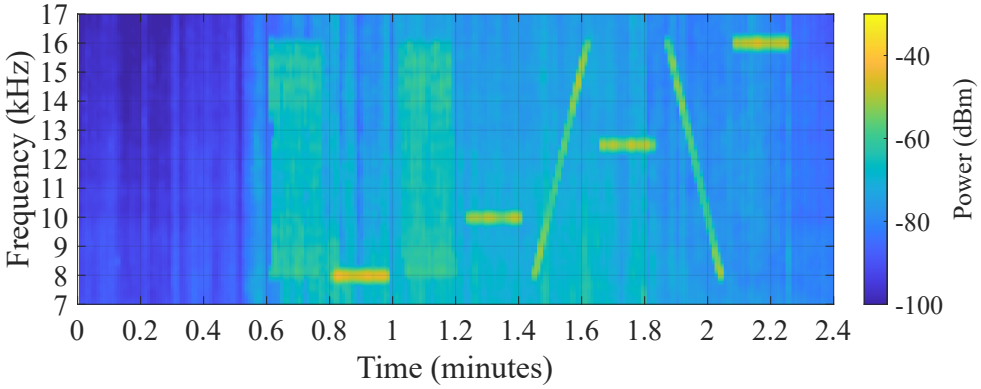

(b) AMAR B at high flow.

Figure 4.9: Spectrogram of received probing sequences.

In (4.31), $x(t)^*$ is the complex conjugate of the reference signal, τ is the lag, and $y(t)$ is the filtered received signal at time t. Because the signal is sampled at $F_s = 64$ kHz, the measured CIR tap delay spacing is 15.625 microseconds. Next, the set of measured CIRs are used in a parametric data-driven model to find the statistics of intrapaths power delay profile.

A parametric model can describe a channel within finite number of parameters needed to be predicted [135]. For fast fading channel we use statistical parametric model. Statistical characterization of intrapaths can determine properties of small-scale fading. Such a characterization requires a path-based probabilistic model of the channel using the statistical measurements of the channel. Here, we demonstrate path-based model of channel as equivalent to discrete-delay channel transfer function model presented in Section 4.1.2. The path p with N_p intrapaths can be defined by a discrete-delay model [136] as

$$H_p[f_k] = \sum_{i=1}^{N_p} h_{p,i} e^{-j2\pi f \tau_{p,i}}, \tag{4.32}$$

where $h_{p,i}$ and $\tau_{p,i}$ denote the intrapath i complex amplitude and delay respectively, and $f = f_0 + f_k$ is the discrete frequencies where f_k is the incremental frequency from 0 to 7999 Hz. We can write equivalently

$$H_p[f_k] = \sum_{i=1}^{N_p} c_{p,i} e^{-j2\pi f_k \tau_{p,i}} \tag{4.33}$$

where $c_{p,i} = h_{p,i} e^{-j2\pi f_0 \tau_{p,i}}$.

We use an equivalent discrete path based channel model of [56] as an alternative to the model in (4.33). A baseband discrete-delay equivalent for the transfer function of path p, with delay spacing of $\Delta\tau = T/K$, $T = 1$ second up-chirp tone and $K = 8000$ frequency steps can be expressed as

$$H_p[k] = \sum_{l=1}^{L} X_l e^{-j2\pi f_k l \Delta\tau}, \tag{4.34}$$

where X_l is the complex tap coefficient of equally spaced delays, l is the sample index, L is the total number of taps,

$$X_l = \frac{1}{K}\sum_{i=1}^{N_p} c_{p,i} e^{-j\pi(K-1)} \left(\frac{\tau_{p,i}}{T} - \frac{1}{K}\right) \cdot \frac{\sin\left(\pi K\left(\frac{\tau_{p,i}}{T} - \frac{l}{K}\right)\right)}{\sin(\pi(\frac{\tau_{p,i}}{T} - \frac{l}{K}))}, \qquad l = 0, ..., K-1, \tag{4.35}$$

Equation (4.34) represents the baseband model for the channel path p using equally spaced samples of complex coefficients [56]. Next, the statistical properties for the intrapaths are found.

Small-scale Analysis

To find the statistical properties for the distinct intrapath delays and gains, the measured complex tap coefficients are mapped into the physical path-based channel model defined in (4.34). Note that to obtain the CIR, the measured voltage is converted at the acoustic sound intensity level at the receiver in dBm re1μPa, which is subtracted from the transmit acoustic power, equal to 180 dBm re 1 μPa @ 1 m from the source. To eliminate background noise, and side lobes from the cross-correlation, a 20 dB threshold is used to discard taps whose magnitude is 20 dB less than the maximum magnitude.

Figure 4.10 superposes nine successive CIRs resulting from the processing of nine one-second LFM up chirps received at one AMAR B hydrophone on September 28, 2018, at 11 AM.

Delays locations of CIRs in Figure 4.10 suggest the existence of separate clusters of arrivals. To find the channel gain and delays for each cluster p, a k-mean algorithm [137] is used to classify intrapaths' delay and gain based on their separation. The initial number of dominant paths is estimated by the Bellhop nominal path analysis in Figure 4.1 and applied to the k-mean classifier.

Figure 4.11 shows the PSD of the identified cluster paths from the CIRs presented in Figure 4.10. The PSD of the channel describes the energy present in the channel as a function of discrete frequency.

A departure from flatness in Figure 4.11 can reveal time delay differences among the various signal frequency components in different clusters caused by scattering from the surface and bottom. The first cluster in Figure 4.11, resembles the direct path with the bottom bounce with minimum delay differences. The second and

third clusters in Figure 4.11, can be matched up with the second and third paths in Figure 4.1; the former has one bounce from the bottom, and the latter has one bounce from the surface.

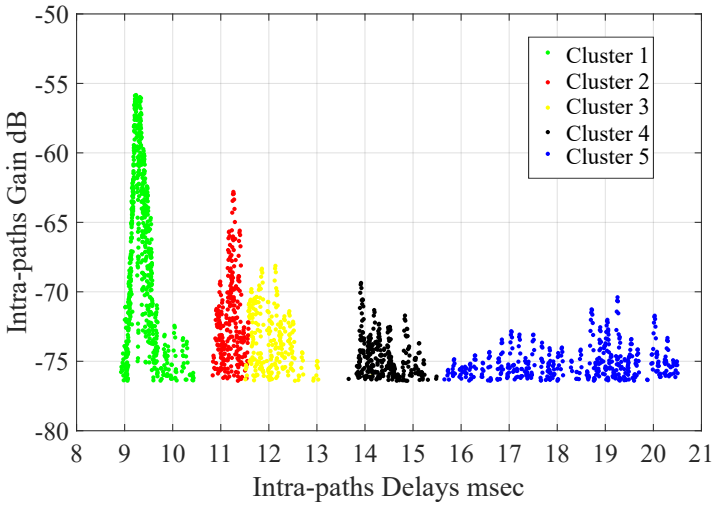

Figure 4.10: Nine channel impulse responses from the Grand Passage sea trial spanning a total period of nine seconds.

Statistical Characterization of Intrapaths

To find the statistical properties of the small-scale fading a maximum likelihood estimator (MLE) is used to fit the intrapath delays and gain samples to different distributions for each nine-second channel probe. The data analyzed in this section serve as an example, specifically for September 28, 2018 at 11 AM and is fit to twenty parametric distributions defined by Matlab [138]. The MLE determines and orders the fitted distributions with their parameters in increasing order of normalized mean square error (NMSE). The best fit distributions are depicted in Figure 4.12 for the intrapaths gain and delay. The corresponding NMSE value for the 3 best fit gain distribution for clusters 1, 2, and 3 are shown in Table 4.3.

As can be observed in Figure 4.12a, the intrapath gain for the first and the second clusters have a good fit to a parametric inverse Gaussian (IG) distribution. In fact, in [139], the IG distribution has been shown to describe shadowing phenomena in multipath fading channels. The scale parameters μ and shape parameters λ of IG distributions are shown in Tables 4.3a, and 4.3b.

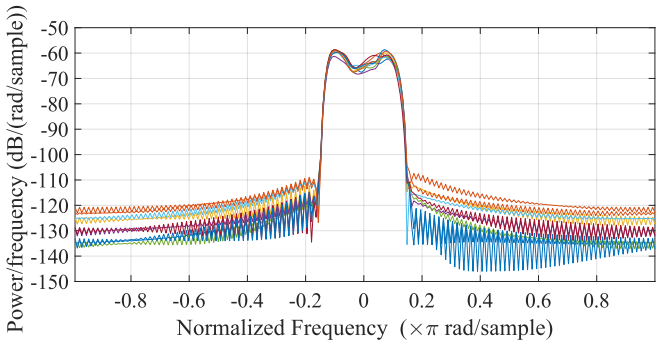

(a) First cluster

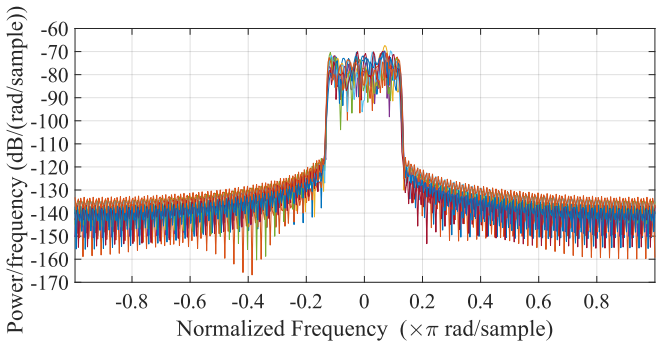

(b) Second cluster

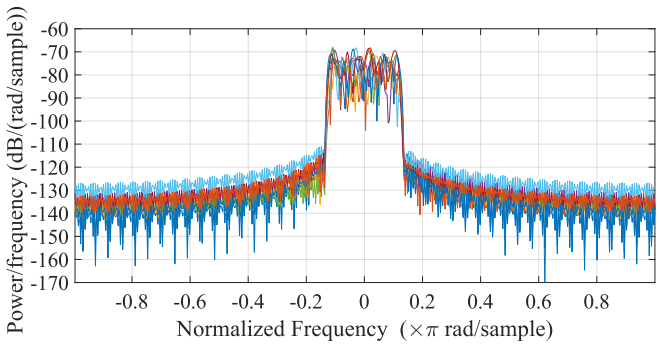

(c) Third cluster

Figure 4.11: PSD for clusters measured for 9 consecutive CIRs.

For the third cluster, the best fit for intrapath gain is described by Logistic distribution with the shape parameter and the scale parameter shown in Table 4.3c. Logistic fading has been proposed recently to model small-scale signal fading for none-line of sight cases in a tight and reflections-rich environment [140]. It should be noted that the fourth cluster fit represents a log-normal fading and the fifth cluster impacted by noise, and none of the distributions resulted in a good fit.

Similarly, the corresponding NMSE value for the delay of cluster 1, 2, and 3 are shown, respectively in Table 4.4.

For the intrapath delay, as can be observed in Figure 4.12b, the first and second clusters are fit to normal distributions with relatively small NMSE. The normal fit parameters for clusters one and two including mean μ and standard deviation (SD) σ are shown in Table 4.4a and 4.4b respectively. SD of intrapath delays is an important parameter that can indicate frequency selective fading severity.

Table 4.3: Intrapath gain best fit distribution parameters

(a) Cluster 1 intrapath gain

Name	Scale	Shape	NMSE
Inverse Gaussian	5.62e-04	1.83e-03	0.03
Birnbaum Saunders	4.92e-04	5.34e-01	0.03
Lognormal	-7.62e+00	5.19e-01	0.04

(b) Cluster 2 intrapath gain

Name	Scale	Shape	NMSE
Inverse Gaussian	6.04e-04	1.93e-03	0.06
Birnbaum Saunders	5.27e-04	5.39e-01	0.06
Rayleigh	3.3e-04	N/A	0.12

(c) Cluster 3 intrapath gain

Name	Scale	Shape	NMSE
Logistic	2.80e-04	6.41e-05	0.55
Exponential	3.04e-04	N/A	0.61
Inverse Gaussian	3.04e-04	2.09e-03	0.90

Figures 4.13a and 4.13b show different clusters intrapath delays mean and variance over a period of 34 days from September 22 to October 25, 2018, in Grand Passage, Bay of Fundy, Nova Scotia. A comparison of the tidal effects depicted in

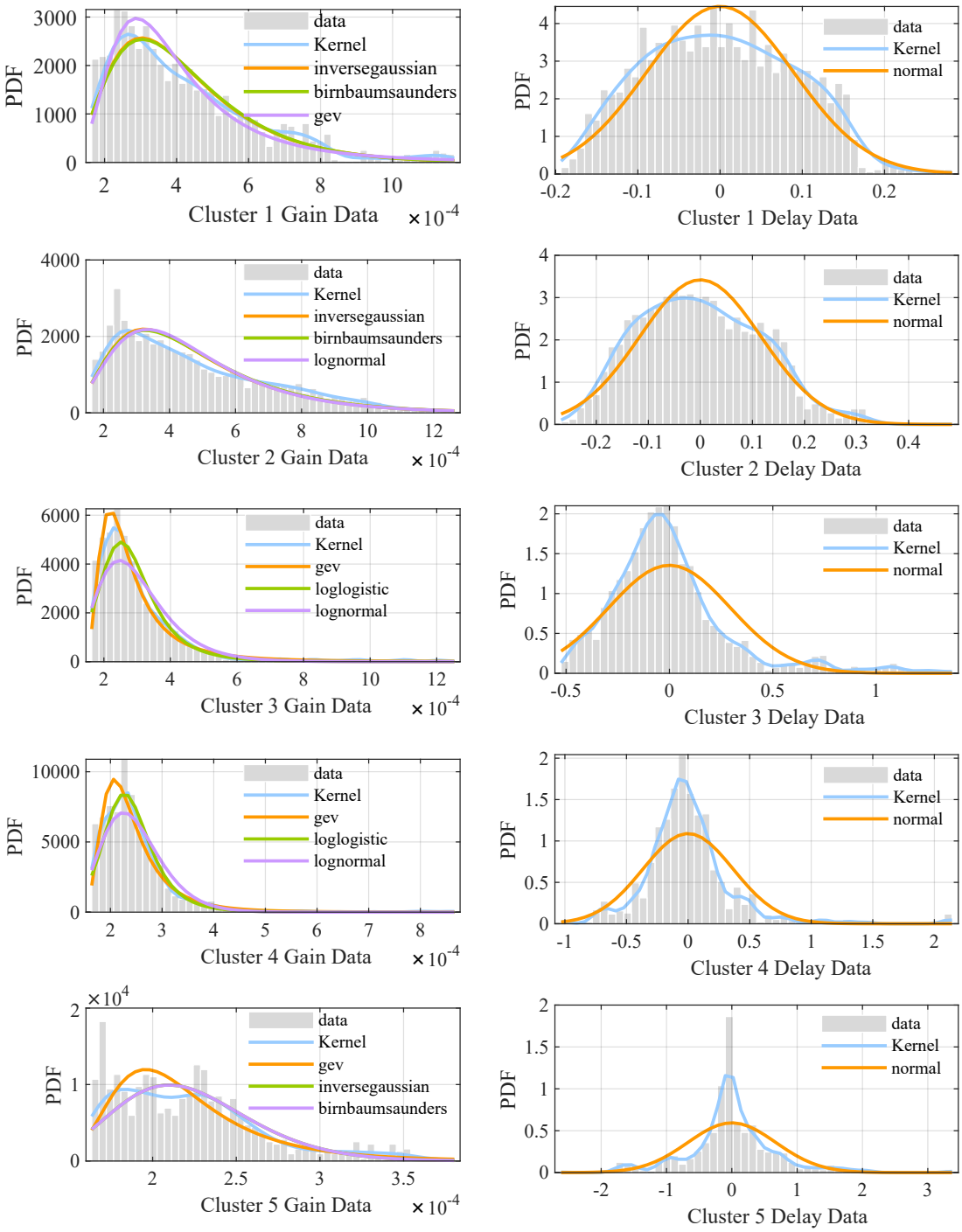

(a) Intrapath gain. (b) Intrapath delay.

Figure 4.12: Best PDF Fit.

Table 4.4: Intrapath delay best fit distribution parameters

(a) Cluster 1 intrapaths delays

Name	Mean	Standard deviation	NMSE
Normal	4.84e-16	8.95e-02	0.10

(b) Cluster 2 intrapaths delays

Name	Mean	Standard deviation	NMSE
Normal	8.72e-16	1.16e-01	0.05

(c) Cluster 3 intrapaths delays

Name	Mean	Standard deviation	NMSE
Normal	1.87e-16	2.94e-01	0.17

Figure 4.8 with the variations in the mean and variance of intrapaths delays suggests the existence of a correlation between them which can explain channel characteristics statistics variations in different tide phases. Next, we will channel large-scale characteristics.

Large-scale Analysis

Here, the acoustic channel characteristics are analyzed as a function of time, using measurements taken during 34 days sea trial. Accordingly, the channel large-scale gain, delay spread, and the Doppler variations are obtained. The channel gain in Figure 4.14 is obtained at AMAR B for a distance of 566 meters from the source. The channel gain represents the received signal power as a function of the transmit power, and is calculated by converting nine channel impulse response in the frequency domain, and applying (4.11). A periodic trend can be observed in the mean and variance of channel gain which will be studied in more detail in Section 4.4.

Next, the delay spread is analyzed using (4.13). The delay spread is calculated using the CIR produced using the LFM probes, and evaluated for the nine CIRs derived from probing sequences at each half hour. The results of a representative window of 34 days are shown in Figure 4.15. As can be seen, the delay spread resembles a periodic pattern similar to that of the gain.

The maximum Doppler shift is also measured for 8, 10, 12.5 and 16 kHz tones. The maximum Doppler shift is obtained by calculating the power spectral density

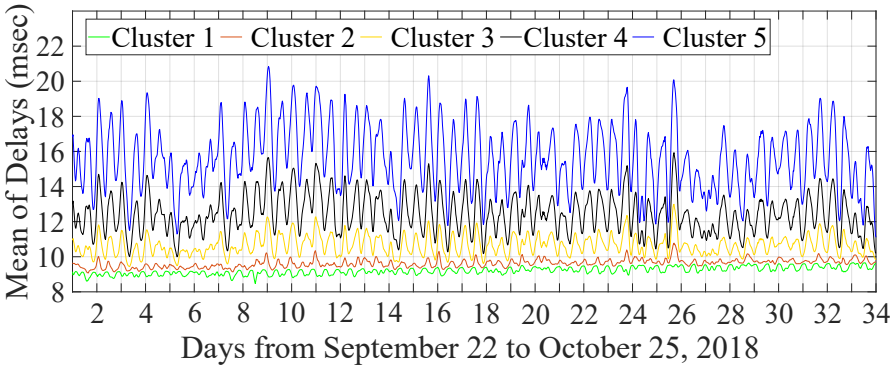

(a) Mean of clusters intrapaths delays.

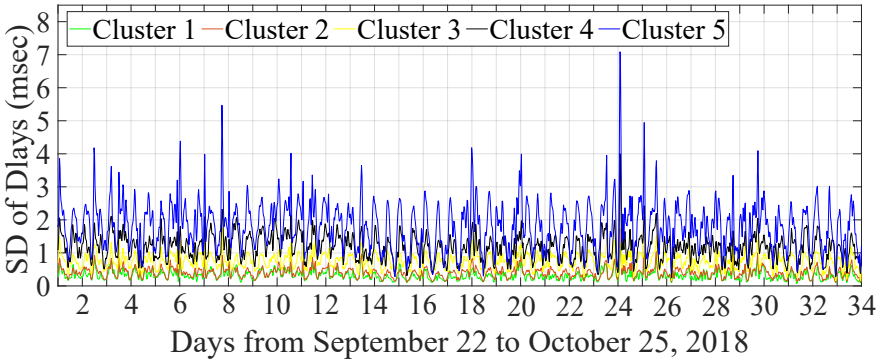

(b) Standard deviation of clusters intrapaths delays.

(PSD) of the received tones, and, in this work, it is defined as the frequency for which the spectral energy has dropped by 20 dB with respect to the peak energy at 0 Hz. Using the Doppler spread of the signal sampled every 30 minutes over all 34 days. The calculated Doppler shifts shown in Figure 4.16 have a periodic trend and, as expected, larger shifts occur at larger frequencies.

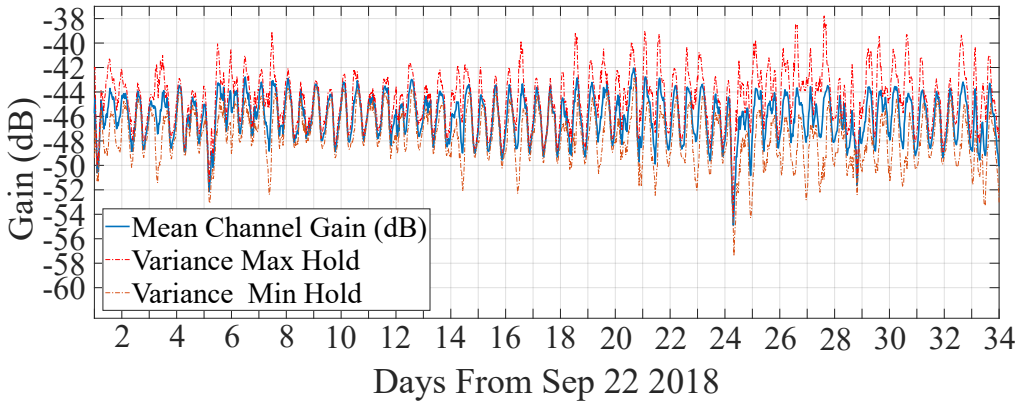

Figure 4.14: Large-scale gain variations over a window of 34 days in the 566-meter channel.

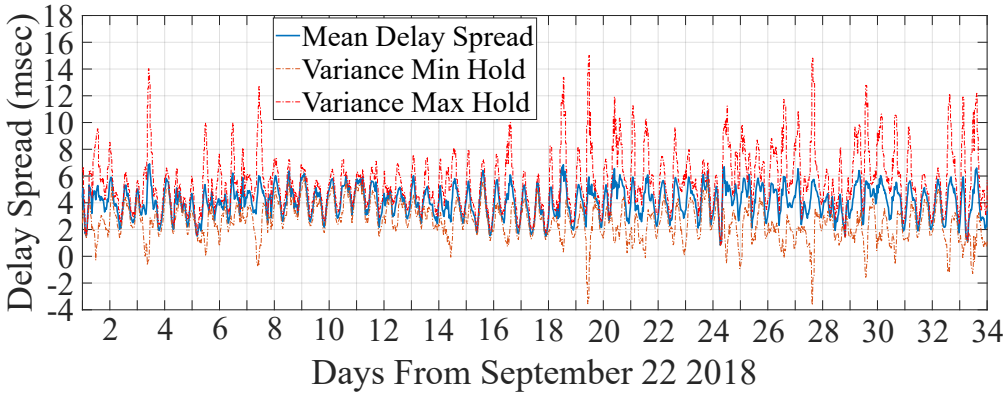

Figure 4.15: Large-scale delay spread over a window of 34 days in the 566-meter channel.

Next, the correlation between the channel characteristics and different channel tide phases will be analyzed.

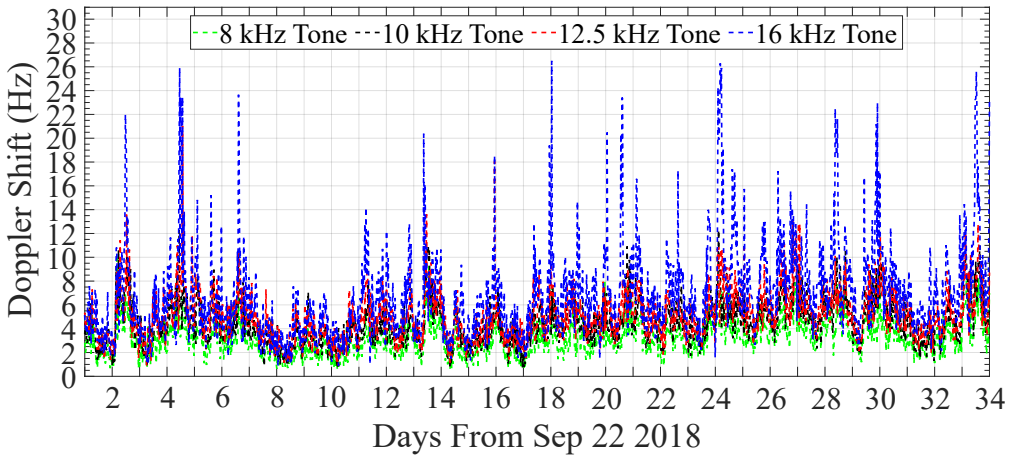

Figure 4.16: Maximum Doppler shift variation at a 20-dB threshold over a window of 34 days in the 566-meter channel.

4.4 Relationship to Tide Variations

Studying the correlation between the channel characteristics and physical environmental conditions of the ocean gives insightful context to predict channel variations. Our analysis shows a strong correlation between tidal currents and channel characteristics variation. Tide plays a key role in surface elevation variation in shallow environments. Tides are regular and predictable. Using harmonic analysis, the numerous different patterns in the tide can be broken down into a series of much simpler waves called tidal harmonics. Tidal harmonics have a very specific frequency relative to the movements of the Earth, Moon and Sun. However, the amplitude of each harmonic and its phase is unique to each location [141]. Here, Fourier transforms analysis is used to finding the dominant harmonic frequency. Specifically, a brute force search algorithm is used on the measured sea-level variations during the trial period at Grand Passage to find the fit expression.

$$\Delta h[n] = -0.0028 + 1.9929 \sin(2\pi \cdot 0.0402 \cdot n + 1.5936) \tag{4.36}$$

where n is the index of discrete time-series of tide height samples. Note that the sampling interval is 30 minutes which results in a tide period of $T = 12.43$ hours. Accordingly, 25 tide phases are defined with a residual lag of 3.9 minutes that is compensated by a shift every eight tide cycle. Figure 4.17 shows the Grand Passage

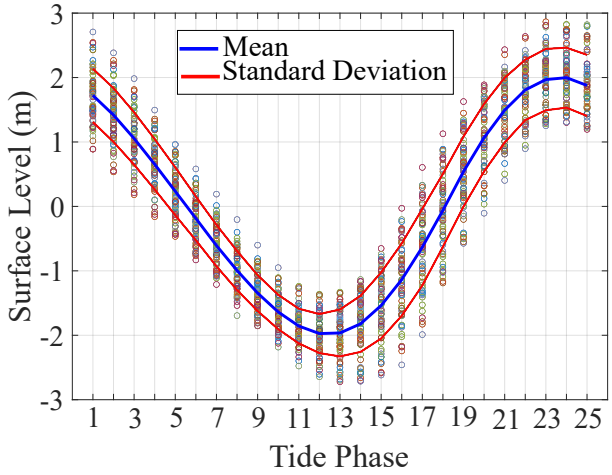

Figure 4.17: Surface level in different tide phases in Grand Passage Nova Scotia.

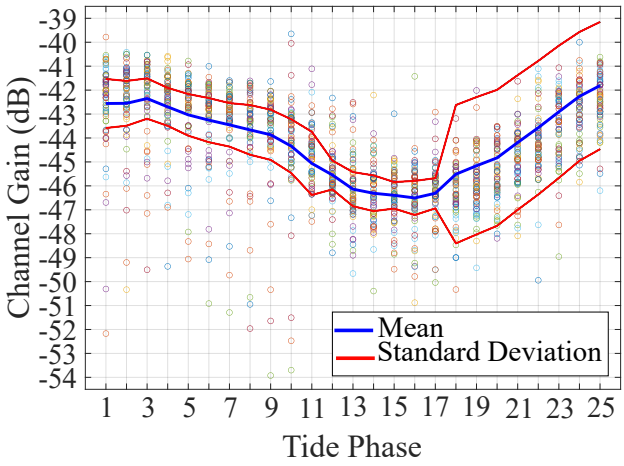

Figure 4.18: Channel gain at different tide phases in Grand Passage Nova Scotia.

water surface level at different tide phases during the 34-day sea trial.

The periodic trend in channel characteristics of Figures 4.14, 4.15 and 4.16 implies the existence of a correlation between the channel characteristics variations and tide phases. A Fourier analysis shows that a dominant harmonic with a tide period of $T = 12.43$ hours exists. Also, the channel characteristics variations can be represented by their corresponding tide phases, shown in Figures 4.18 ,4.19 and 4.20.

The approach taken in this work is based on modeling channel characteristics as a sinusoids plus a residual random noise component. Accordingly, the channel characteristics can be represented by

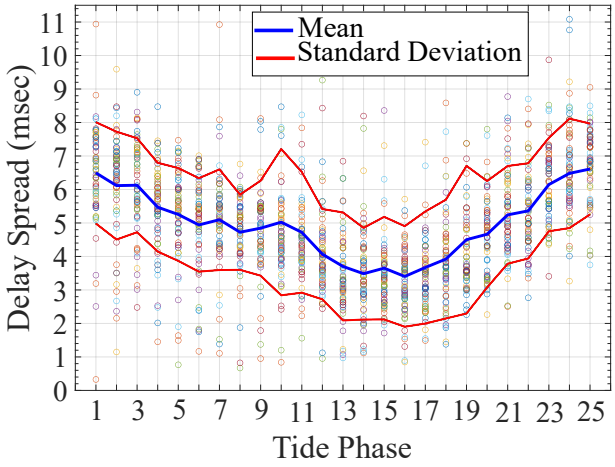

Figure 4.19: Channel delay spread at different tide phases in Grand Passage Nova Scotia.

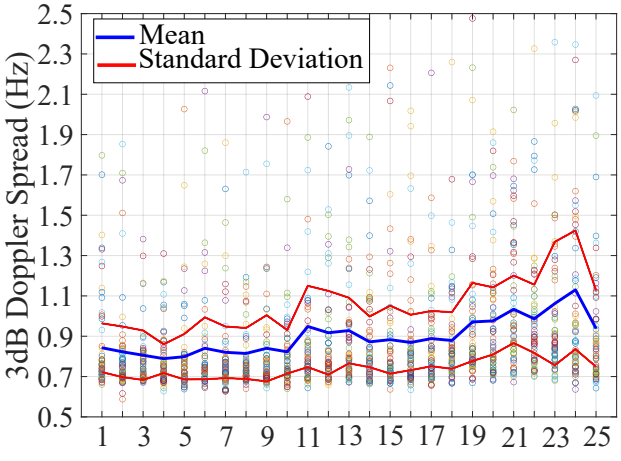

Figure 4.20: 16 kHz tone 3 dB Doppler spread at different tide phases.

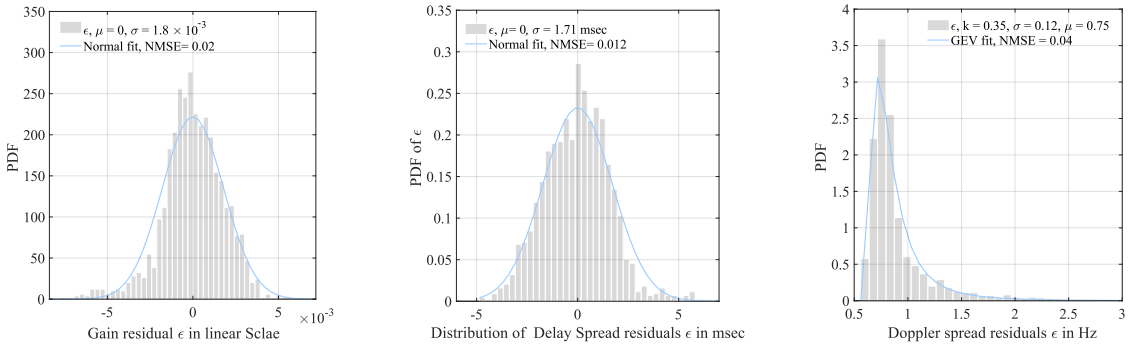

Figure 4.21: PDF of random residuals for linear scale Gain magnitude, Delay spread and Doppler spread, respectively.

$$y[n] = A + B\sin\left(2\pi \cdot 0.0402 \cdot n + D\right) + \epsilon[n] \tag{4.37}$$

with n being an integer index for discrete time series measurements at a 30-minute interval. The first two terms A and $B\sin\left(2\pi 0.0402 \cdot n + D\right)$ represent the relevant tide condition and a latent process $\epsilon[n]$ represents the contribution of noise imposed by unknown physical environmental effects. Accordingly the latent channel characteristics at each period of tide phase of ϕ can be represented by

$$y_\phi[nT] = C_\phi[(n-p)T] + \epsilon_\phi[nT], \tag{4.38}$$

where y is the channel characteristic sampled at tide periods of $T = 12.43$ hours at a tide phase of ϕ, n is the index of the tide period and C_ϕ is a slow varying tide phase dependant process with a memory p and ϵ_ϕ is a noise residual component.

The random noise ϵ_ϕ variable statistics for the channel characteristics can be determined using a parametric probabilistic models as shown in Figure 4.21. The random noise ϵ_ϕ was fit and it can be demonstrated that it follows a zero mean Gaussian distribution for channel gain and delay spread and follows Generalized Extreme Value (GEV) distribution for Doppler spread. As explained in [142] when the process noise follows a Gaussian process or a GEV process in [143] the latent process defined by (4.38) can be modelled as a Markov process. Defining a Markov chain process to predict channel characteristics in different tide phases will be discussed next in the next section.

4.5 Summary

In this Section, first, a channel model for a high-flow shallow environment is presented that takes into account tidal flow. Then, the impact of flow and surface elevation variations on channel characteristics statistics was evaluated using measurements collected from a 34-day sea trial conducted in Grand Passage, Nova Scotia. For this purpose, a probabilistic parametric model was developed by fitting the channel tap power delay profile derived from sparse channel measurement to a set of probability distributions. Finally, an statistical model supported by experimental measurements was used to demonstrate the existence of a correlation between the channel characteristics statistics and the surface elevation variations.

Chapter 5

Channel State Information Prediction

Various CSI acquisition methods have been proposed in recent years. For example to characterize the fast fading, in [13], acoustic channel prediction is explored to optimize an OFDM-based underwater acoustic (UWA) communication system. The authors investigate the possibility of utilizing the CSI at least one travel time ahead of transmission, and a Matching Pursuit (MP) algorithm is used to identify the path coefficients. The proposed adaptation requires a stable and low-latency feedback link from the receiver. In comparison, in [144] an adaptive channel prediction scheme is proposed that extrapolates the CSI from a block of training symbols to optimize the receiver. The authors exploit the sparse structure of the delay-Doppler representation of the channel to reduce the complexity. Similarly, in [61] a channel-aware adaptive modem is proposed to cope with the temporal slow variability of the channel behavior in terms of maximum delay spread and Doppler spread. The measured large-scale transmission loss is forwarded to the transmitter on a regular basis.

Using machine learning to predict CSI has attracted significant attention in recent years. In [145], predicting the UWA channel is explored in the frequency domain, which combines a convolutional neural network and a long short-term memory network (LSTM) to capture the temporal correlation and frequency correlation of the CSIs. The training set is updated every five minutes. Note that the storage of a large amount of channel data for different physical environmental conditions can be a challenging issue for deep neural network techniques running on remote underwater nodes.

Our sea trial data set analysis in Chapter 4 implies that the channel characteristics time series show significant transitions on a large time scale. The UWA channel characteristics statistics variations in different sea states has motivated this work to define a multi-layer discrete-time Markov process in which each layer corresponds to a distinctive sea state. Following in this chapter first, in Section 5.1, a multi-layer finite

state Markov model is explained; then, in Section 5.2, the channel characteristics between two fixed nodes are predicted using a model based on the Markov chain approach; then, in Section 5.2.2, it is demonstrated that how channel prediction from the fixed nodes can be incorporated into a stochastic model to track channel variation in a mobile node; finally, in Section 5.4 the BER performance of a mobile OFDM link is investigated in different tide and signal to noise ratio levels.

5.1 Discrete Time Markov Chain Model

Markov chain models make a flexible and efficient class of stochastic processes which have been used to precisely solve a broad range of applied problems.

The study of communications channel modeling as a finite-state Markov process emerged from a two-state Gilbert-Elliot channel [146], and extensions of Markov process with more than two states have also been developed for rapidly time varying channels [147].

For example, in [148], a latent Markov process is proposed and hourly variations of the channel signal-to-noise ratio (SNR) are predicted between two fixed nodes. The authors selected SNR as a figure of merit to quantify the channel communication quality, but, the small-scale statistics are not taken into consideration. Also, in [149], the fading process is modelled with a Hidden Markov Model (HMM) using direct parameter estimation from experimental data, in which the HMM output is fit to a Monte Carlo simulation of a Rayleigh fading process [40]; however, the UWA channel amplitude for each path delay does not always follow a Rayleigh fading process [150].

At the core, a stochastic process $Y = \{Y_n : n \geq 1\}$ is defined and relies on a finite number of states S; it is a Markov chain if for any $i, j \in S$ and $n \geq 1$ such that

$$P\{Y_{n+1} = j | Y_1, \cdots, Y_n\} = P\{Y_{n+1} = j | Y_n\} \tag{5.1}$$

The condition in (5.1), called the *Markov property*, stipulates that at any time n, the next state Y_{n+1} is conditionally independent of $Y_1, \cdots, Y_{n-1}$ given the present state Y_n [151]. The Markov property is a condition that is satisfied by the state of many stochastic phenomena. As described in Section 4.4, key channel characteristics can be expressed as discrete-time stochastic processes with their future values evolving from the current time observation, and only depend on the current state [152]. For

a discrete channel characteristic $y_\phi[nT]$ at tide phase ϕ, let $S = s^1, s^2, ..., s^k$ denote a finite set of states and S_{nT}, $n = 1, 2, ..$ be a constant Markov process. The channel states in each tide phase are created by binning all possible data values into K bins. Since it is assumed that the Markov process has a stationary transition property during $t = nT$, where $T = 12.43$ hours, the transition probability is independent of the tide phase index of n and can be written as

$$p_{i,j} = P(S_{(n+1)T} = s_j | S_{nT} = s_i), \tag{5.2}$$

for all $n = 1, 2, ..$ and $i, j \in 1, 2, ..., K$. Also, a $K \times K$ state transition probability matrix P_ϕ can be defined at each tide phase $\phi \in \{1, 2, ..., 25\}$ with element $p_{j,i}$, such that

$$P_\phi = \begin{bmatrix} p_{1,1} & p_{1,2} & \cdots & p_{1,K} \\ p_{2,1} & p_{2,2} & \cdots & p_{2,K} \\ \vdots & \vdots & \ddots & \vdots \\ p_{K,1} & p_{K,2} & \cdots & p_{K,K} \end{bmatrix} \tag{5.3}$$

A state transition probability matrix P_ϕ is a stochastic matrix [153] for which the sum of its element on each row is equal to 1, i.e.

$$\sum_{j=1}^{K} p_{i,j} = 1; \text{ where } i = 1, 2, .., K. \tag{5.4}$$

Note that $p_{i,i}$ is the probability to leave the state i and the conditional probability $p_{i,j}|p_{i,i}$ is the probability of selecting state j leaving the state i.

Considering the stationary transition property, the probability of being at state $S_{nT} = s_k$ at any time index nT without any information from the previous state is represented using a $K \times 1$ steady-state probability vector A_{nT} defined as

$$A_{nT} = [p_1, p_2, ..., p_K]. \tag{5.5}$$

The transition matrices have the chain property that the product of the previous transition matrices describes the transition at the next time step $(n+1)$. Specifically, the Markov chain at Step $(n+1)$ for each tide phase ϕ can be determined by finding the $(n+1)$-th step transition matrix $P_\phi^{n+1} = P_\phi^1 . P_\phi^2 \ldots P_\phi^n$. The $(n+1)$-th step transition matrix $P_\phi^{(n+1)}$ can otherwise be expressed using

$$P_{\phi}^{n+1} = \begin{bmatrix} P(S_{n+1} = s_1 | S_n = s_1) & \cdots & P(S_{n+1} = s_K | S_n = s_1) \\ \vdots & \ddots & \vdots \\ P(S_{n+1} = s_K | S_n = s_1) & \cdots & P(S_{n+1} = s_K | S_n = s_K) \end{bmatrix} \tag{5.6}$$

Figure 5.1 shows an $(n+1)$-step Markov process chain with 25 tide phases. If the channel state at step n and phase ϕ is known to be $S^n = s_l$, the channel state $S^{n+1} = s_m$ can be predicted by finding the maximum element of the l^{th} row in matrix P_{ϕ}^{n+1}. Next, the proposed Markov chain model is applied to predict channel characteristics one tide cycle ahead.

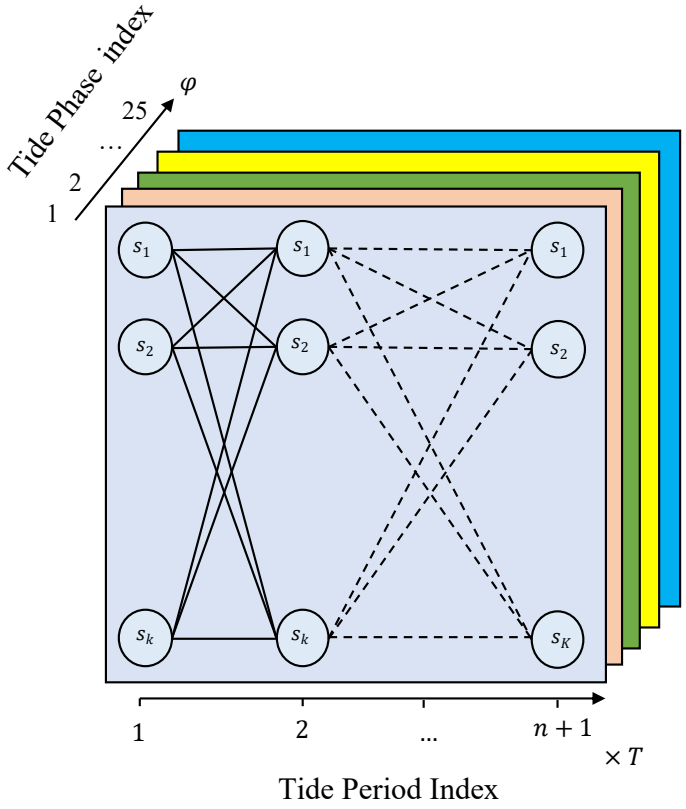

Figure 5.1: Illustration of the proposed Markov process chain. A Markov process chain is defined for each tide phase. Index $n+1$ refers to the next tide cycle.

5.2 CSI Acquisition in a Fixed Node Scenario

5.2.1 Predicting Channel Large-scale Characteristics

In this section, a Markov chain is applied to the channel large-scale characteristics data set, and the states determined directly from the data set acquired from channel sounding. The channel large-scale characteristics including the gain, delay and Doppler spread can be described at any time as being in one of the states $s_1, s_2, \cdots, s_k$. Each state represent a range of values that the random channel characteristics can take. The set of 1632 observations at an interval of 30 minutes are generated by concatenating time series observations of channel gain, delay and Doppler spread data during the 34 days. At each tide phase $\phi \in \{1, 2, \ldots 25\}$, $n = 64$ samples of channel gain, delay and Doppler spread are binned in K states. The intervals between the sampling period is one tide period T and the number of states which quantize the possible values of channel characteristics in K states are determined in such a way that the maximum error for the channel gain, delay and Doppler spread remain below 1 dB, 1 msec and 0.2 Hz respectively. Figures 5.2, 5.3 and 5.4 show the prediction of channel characteristics at step $n + 1 = 65$, which is the next tide cycle after the observation in the tide cycle $n = 64$.

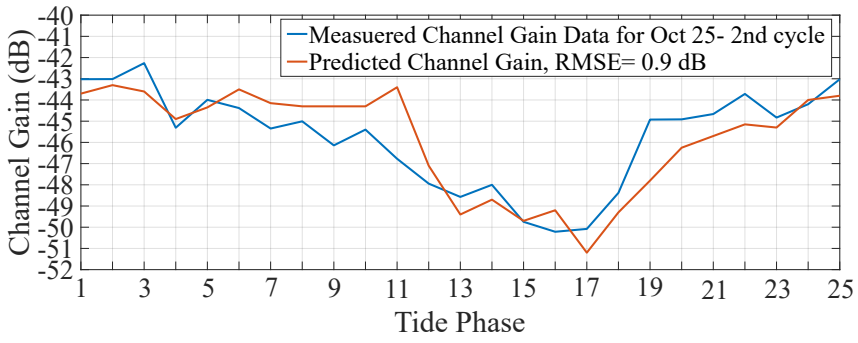

Figure 5.2: Predicted channel gain on Oct. 25, 2018.

The RMSEs reported in the figures for the predicted channel characteristics are within quantization size of each state, which indicates that the proposed Markov chain model can predict the channel characteristics precisely at one tide phase ahead.

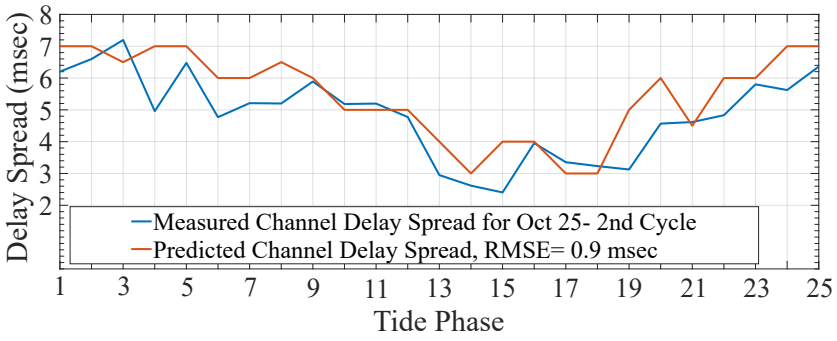

Figure 5.3: Predicted channel delay spread on Oct. 25, 2018.

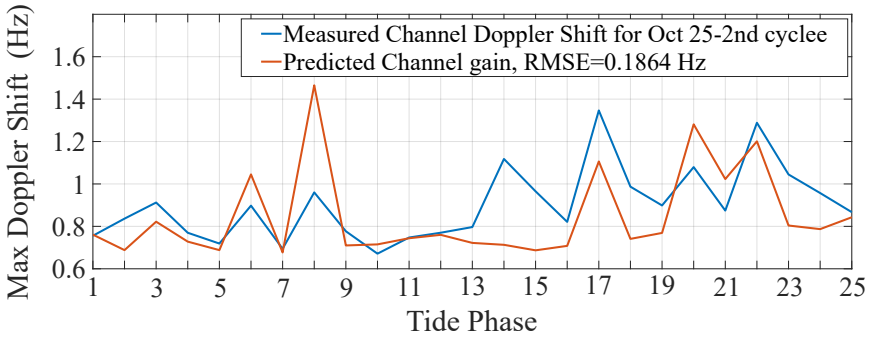

Figure 5.4: Predicted channel maximum Doppler shift at 16 kHz on Oct. 25, 2018.

5.2.2 Predicting Channel Small-scale Statistics

The SD of intrapath delays for cluster three $\sigma_{\delta_{p3}}$ is shown in Figure 5.5. The random variable $\sigma_{\delta_{p3}}$ takes values in a state space of S and can be represented by

$$\sigma_{\delta_{p3}}[n] = C[n] + \epsilon_{\sigma_{p_3}}[n] \tag{5.7}$$

where $C[n]$ is a sinusoidal with period of $T = 12.43$ Hours and $\epsilon_{\sigma_{p3}}$ is the process noise with zero mean Gaussian distribution as shown in Figure 5.5. It is equal to

$$C[n] = 1.1637 + 0.285\sin(2\pi n \times 0.0402 + 0.6802) \tag{5.8}$$

A Markov chain similar to what is presented in Section 5.1 is defined for $\sigma_{\delta_{p3}}$ in different tide phases. The model predicts the SD of intrapath delays for cluster three during the next tide cycle in different tide phases. The predictions of $\sigma_{\delta_{p3}}$ with RMSE of 0.14 msec are shown in Figure 5.5.

Predicting the SD of the intrapath delays is significant, because the result can be

incorporated in the analytical model described in Section 4.1.2. As such, ensembles of CIRs or equivalently channel frequency responses can be predicted, making channel tracking possible.

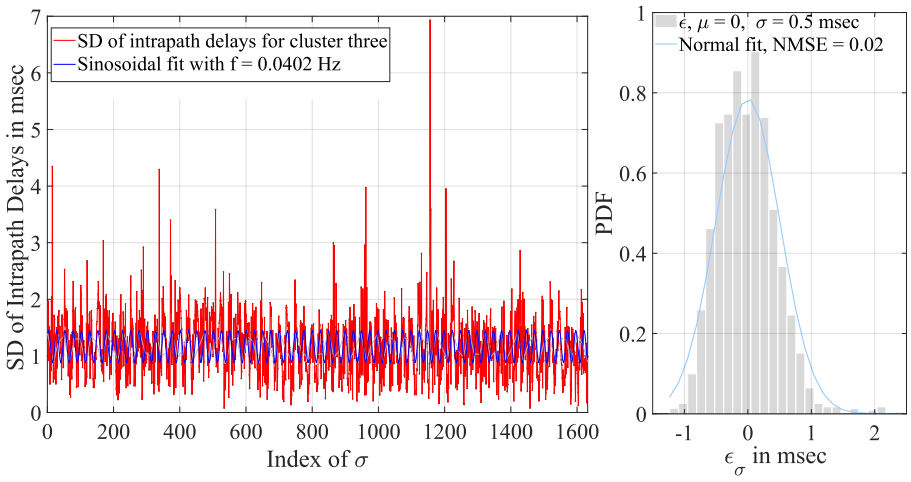

Figure 5.5: Standard deviations for the intrapath delays of Cluster 3 during 34 days, sampled at 30 minutes intervals. A sinusoidal is fit and the zero mean Gaussian distribution of the residual is shown on the right.

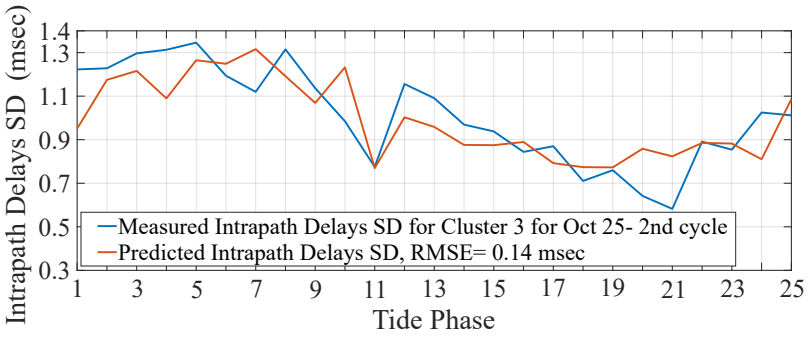

Figure 5.6: Prediction of the standard deviation for the third cluster intrapath delays on Oct. 25, 2018.

5.3 An Acoustic Channel Tracker to Estimate CSI in a Mobile Scenario

In this section a channel tracking simulator is provided that incorporates data driven statistics of the intrapaths delays into a stochastic model of acoustic channel. The channel tracking simulator is applied to a shallow water channel that is subject to high fluctuations due to tides and provides a realistic representation of the channel impulse

responses for a mobile scenario. The rest of this section is organised as follows: in Section 5.3.1, the acoustic channel model developed by Qarabaqi and Stojanovic [6] is enhanced to incorporate physical properties of a mobile channel in shallow waters. Then in Section 5.3.2, data driven intrapaths delays statistics are incorporated into a mobile channel simulator and CIRs are estimated.

5.3.1 A Stochastic Model for the Acoustic Channel

To enable a reliable and efficient underwater acoustic communication, it is important to design the communication stack to be adaptable to time varying channel conditions. Several models have been proposed to estimate UWACs, which are usually based on collected data from sea trials in a particular location [154] or stochastic model of physical environmental conditions. A stochastic model can generate ensembles of time varying channel by capturing slowly varying environmental effects such as effects of tides, temperature changes, and variable sound speed profiles.

In this section, the stochastic channel model described in [6] is used as the core of a channel tracking algorithm and is enhanced with physical environmental conditions such as tide, SSP and bathymetri as well as data-driven intrapath delays statistics to obtain channel impulse response variations in mobile conditions. Note that in Section 5.2.2, the channel small-scale statistics including standard deviation of intrapath delays predicted using Markov chain. Here, the intrapaths statistics are incorporated into a channel model to develop a channel tracking model.

5.3.2 Tracking the Channel for a Mobile AUV

AUVs used in marine geoscience typically move at speeds of up to 1–2 m/s, and can be influenced by tidal currents which can significantly affect their data transfer quality [155].

As shown in Section 4.2 channel intrapaths statistics including standard deviation of intrapath delays play an main role in small scale fading. Here, a channel tracking model estimates CIRs of an underwater acoustic link between a mobile AUV and a sink node by incorporating channel statistics received from a reference node.

In Figure 5.7 an AUV receives the CSI including the gain, the delay spread, the Doppler spread and the standard deviation of intrapaths delay from a reference

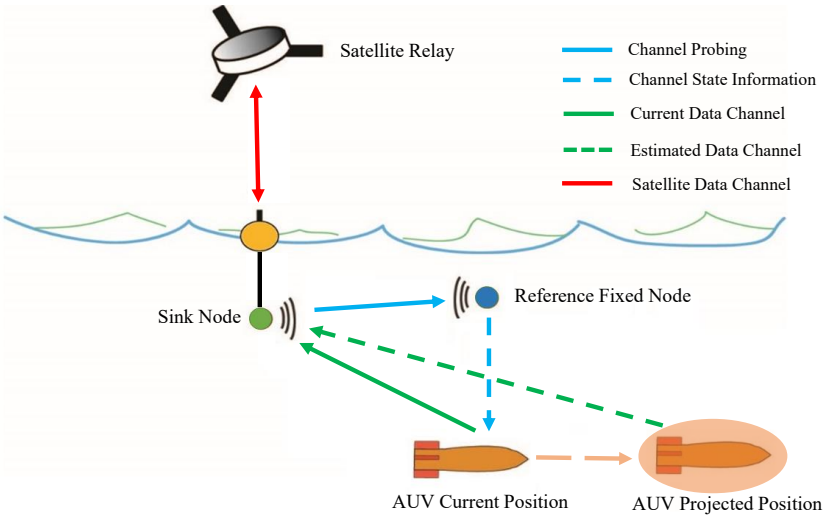

Figure 5.7: The acoustic channel between a sink node and a mobile AUV is estimated. The reference fixed node shares recorded CSI over a prolonged period with the AUV to enable channel tracking at the AUV.

fixed node. The channel tracking software also determines deterministic changes in vehicular speed, SSP, tides and bathymetry. The stochastic model of the channel generates ensemble of time varying CIRs as the AUV pursues its mission.

Channel Tracking Software

The basic time-invariant model of an acoustic channel is that of a multipath channel in which the signal energy attenuates with distance. Using the data driven model described in 4.3 large scale gain and delay can be approximated with h_p and τ_p at the reference point. However the linear speed of AUV deviates the actual path gain from the reference point, also random variations in path length induced by surface roughness adds an additional randomness. Here we used standard deviation of intrapaths delays at the reference point to model this additional variations and incorporated it into the analytical model introduced in Section 4.1.2.

Mobile Channel Tracking Simulation Results

Figure 5.8 shows 8 second CIRs derived from probing sequences on Sep 28 2018 at 11 AM in the Grand Passage sea trial. Standard deviation of intrapath delays of each path in Figure 5.8 is derived from the CIRs at the reference point and shared with the

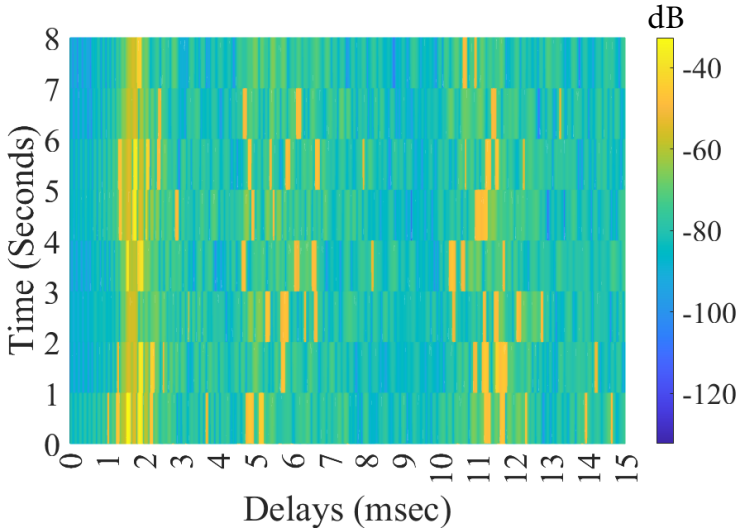

Figure 5.8: Measured 8 seconds CIRs for a reference fixed node, the channel length is 566 meters.

AUV. Standard deviation of intrapath delays captures the effect of surface elevation variation induced by tides and plays the main role in channel variations.

Figure 5.9 shows the estimated CIRs derived from channel tracking for an AUV with linear vehicular speed of 1 m/s shown in the scenario of Figure 5.7.

The linear variations of the delays in Figure 5.9 can be compared to the reference node in 5.8 and corresponds to the linear variations of the lengths of each path along the AUV route during 10 seconds channel realization.

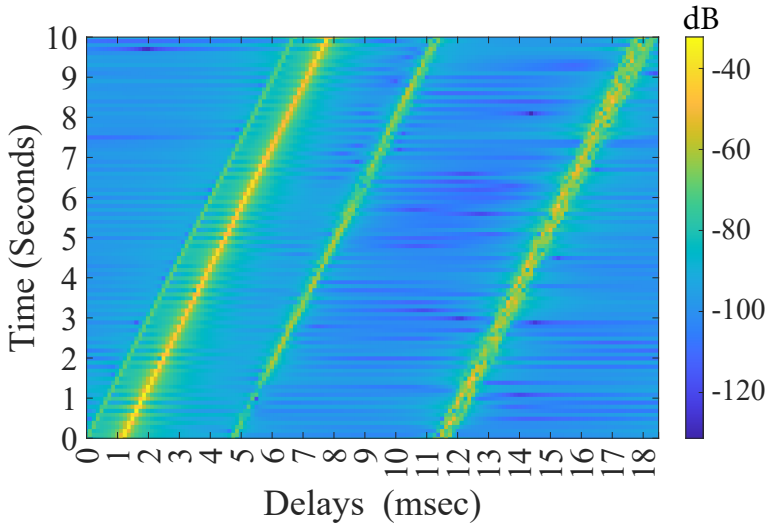

Figure 5.9: Simulated 10 Seconds CIRs for a AUV with a linear speed of 1 m/s.

5.4 Performance Evaluation of Acoustic Link in High Flow Environment

In this section, the BER performance of the time varying acoustic channel of Section 5.3.2 is investigated in different tide and signal to noise ratio levels. To approach this objective the channel information including channel gain, delay and Doppler spread are acquired using the stochastic model of 5.3.2 and used to simulate channel variation for a mobile AUV equipped with OFDM based communication system. The simulator resembles 24 hours variation of the channel in September 28 2018 in Grand Passage, Bay of Fundy, Nova Scotia.

Figure 5.10 demonstrates the flow and tide height variations in Grand Passage during September 28 2018.

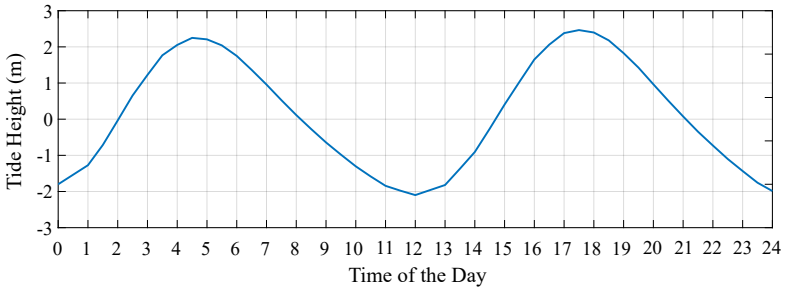

Figure 5.10: Flow and tide height variations during September 28 2018 in Grand Passage.

To evaluate the effect of channel variations on received OFDM signal BER, an OFDM signal with partial FFT demodulation (P-FFT) proposed in [156] is borrowed. P-FFT was shown to be effective in compensating for the channel variations. P-FFT divides the received OFDM block into sections that are shorter than the original OFDM block. If the sections are sufficiently short, the channel variations are expected to be negligible during each section. P-FFT is a good approach when the Doppler shift is not negligible. For this purpose 2000 random bits are generated and QPSK modulation is applied. The proposed OFDM system signal specification is summarized in Table 5.1.

Figure 5.11 show the generated OFDM symbols to be transmitted and applied to the channel. Its is assumed that the transmitter send packets every 30 minutes to be consistent with tide information. A time varying channel which simulates the high flow environment in grand passage during 24 hours in September 28 2018 is generated

Table 5.1: Transmitted OFDM Signal Specification

Parameter	**Value**
Sampling frequency	64 ksample/s
Frequency of lowest carrier	8 kHz
Bandwidth	8 kHz
Number of carriers	1024
Number of OFDM blocks to transmit	6
Duration of zero padding between OFDM blocks	45 msec
Number of pilot carriers	120

for the AUV with linear vehicular speed of 1 m/s. The channel is simulated in 30 minutes intervals to capture the effect of flow on channel variation over 24 hours. To reduce the complexity, only the first three paths for which the amplitude is higher than 1/20 of the first path are considered. The generated OFDM symbol is applied to the channel for SNRs ranging from 1 dB to 30 dB.

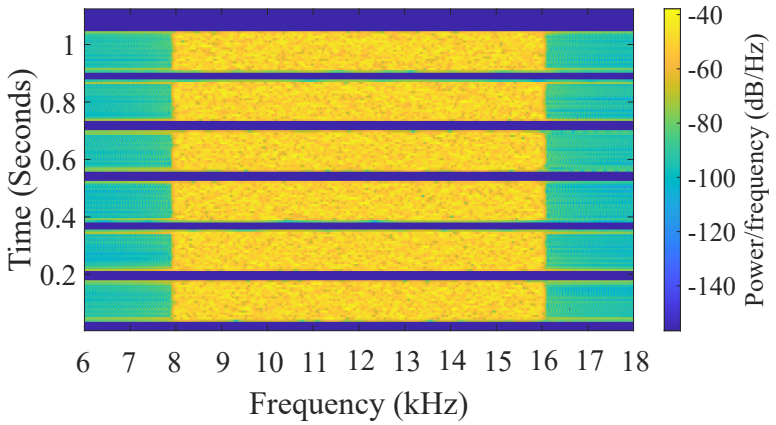

Figure 5.11: Six OFDM symbols are transmitted.

Figure 5.12 shows the BER variations of the received OFDM signal during 24 hours. Comparing the BER variation of Figure 5.12 with the flow variations of Figure 5.10 suggests the existence of a correlation between high BER and high flow conditions.

It can also be inferred that in the scenario of shallow channels increasing the SNR can mitigate the effect of flow and improve the BER to some extends but after a certain point increasing the SNR doesn't seem to be an effective factor. This can be explained by the effect fading imposed on the received signal due to mutipaths.

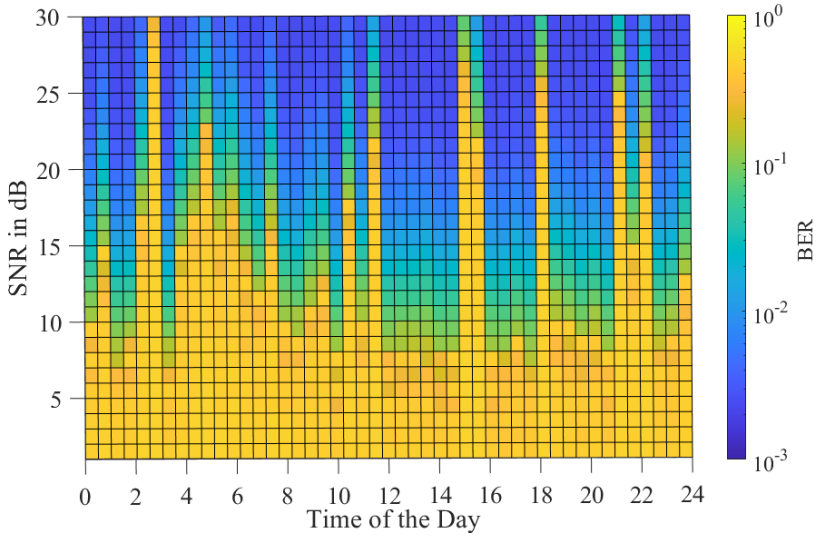

Figure 5.12: BER of the received OFDM symbols during 24 hours in September 28 2018 for SNRs of 1 dB to 30 dB.

5.5 Summary

In this Section, first, a novel multi-layer Markov process was defined to predict the channel characteristics in different tide phases. Each layer of the proposed Markov chain predicts the channel gain, delay, Doppler spread, and intrapaths statistics in one tide phase. The proposed Markov model utilizes context awareness and tracks the deterministic physical environmental conditions to define different states for channel characteristics at intervals of 30 minutes. Considering the dynamic range of channel characteristics in different tide phases, it was demonstrated that the proposed Markov chain model could produce predictions relatively close to the measured values with root mean square errors of 90% of the quantization size of the measurements. Then a channel tracking simulator is presented that incorporates data-driven statistics of the intrapaths delays into a stochastic model of the acoustic channel. The channel tracking simulator is applied to a shallow water channel subject to high fluctuations due to tides. The presented channel simulator provides a realistic representation of the channel impulse responses. The BER performance of generated OFDM signal in the simulated time-varying acoustic channel is investigated in different tide and signal-to-noise ratio levels. Comparing the BER variation of the received OFDM signal with the tide variations suggests the existence of a correlation between the

high BER and the high flow conditions.

Chapter 6

Conclusion

This thesis investigates the design aspects of a cross-layer service that utilizes channel state information to adapt the underwater acoustic network communication stack, including the physical layer, the media access control, and the routing layer to the channel time varying conditions.

To approach this goal, in Chapter 3, a multihop relaying network architecture is defined; it uses an enhanced energy-efficient flooding routing in the control phase and a multihop channel aware relaying for data forwarding. It is demonstrated that in the proposed scenario, by incorporating the channel information in relay selection, the number of hops and the number of retransmission are reduced, which leads to %29 energy savings in the proposed scenario. Further in this chapter, to enable the multihop relaying, a channel-aware MAC scheme is proposed to maximize channel allocations while avoiding collision and maintaining connectivity within the multihop relaying network. It is shown that the proposed MAC scheme has comparable channel utilization performance to the greedy MAC scheme. Still, it achieved a smaller standard deviation in the number of allocated channels to nodes and maintained fairness in resource allocations.

In Chapter 4, the impact of key physical environmental conditions on the channel characteristics is analyzed. For this purpose, 1632 wave files from 34 days sea trial in Grand Passage Nova Scotia were used to derive a set of channel impulse responses for a 566-meter channel in 30 minutes intervals. The channel characteristics include the gain, delay, Doppler spread, and standard deviation of intrapath delays derived during the sea trial period. The theoretical model and experimental channel measurements demonstrate the existence of a correlation between the channel characteristics statistics and the surface elevation variations, particularly in high flow shallow environments. Here, a probabilistic parametric model is used to characterize

the statistical properties of channel taps during different different tide phases by fitting the channel tap power delay profile derived from sparse channel measurement to a set of parametric probability distributions.

In Chapter 5, it is demonstrated that the state of the physical conditions can be exploited to define a multi-layer Markov chain model. Indeed, the proposed multi-layer channel state information prediction scheme is to predict the channel characteristics accurately with a root mean square error of 0.9 dB for the gain, 0.9 msec for the delay spread, 0.18 Hz for the Doppler spread, and 0.14 msec for the standard deviation of intrapath delays. Further, the data-driven channel characteristics and intrapath statistics is incorporated into an analytical model of the channel to give a more realistic representation of the channel's time varying impulse response. Finally, the BER performance of an OFDM link is evaluated between a fixed transmitter and a mobile AUV for 24 hours and at different SNR levels. The BER performance estimation can be used by AUVs, which are operated in a time varying environment, to adjust their physical layer parameters and transmission schedules according to the channel conditions.

In future work, to enable an adaptive network, it is recommended that the channel state prediction algorithm and channel tracking software be implemented on real-time embedded platforms such that remote nodes can estimate the communication link quality under different physical environmental conditions. For this purpose, the handshaking mechanism between the nodes should be defined to demonstrate the MAC spectral efficiency and the routing layer energy efficiency. Finally, a demonstration of the physical layer adaptation in realistic settings will confirm the optimization algorithm in realistic time varying environments.

Bibliography

[1] M. Stojanovic, *High-Speed Underwater Acoustic Communications*, pp. 1–35, Springer US, Boston, MA, 2002.

[2] W. Kuperman and P. Roux, *Underwater Acoustics*, pp. 149–204, Springer New York, New York, NY, 2007.

[3] I. F. Akyildiz, P. Wang, and Z. Sun, "Realizing underwater communication through magnetic induction," *IEEE Communications Magazine*, vol. 53, no. 11, pp. 42–48, 2015.

[4] I. F. Akyildiz, D. Pompili, and T. Melodia, "Underwater acoustic sensor networks: research challenges," *Ad Hoc Networks*, vol. 3, no. 3, pp. 257–279, 2005.

[5] R. Radosevic, A.and Ahmed, T. M. Duman, J. G. Proakis, and M. Stojanovic, "Adaptive OFDM Modulation for Underwater Acoustic Communications: Design Considerations and Experimental Results," *IEEE Journal of Oceanic Engineering*, vol. 39, no. 2, pp. 357–370, 2014.

[6] P. Qarabaqi and M. Stojanovic, "Statistical characterization and computationally efficient modeling of a class of underwater acoustic communication channels," *IEEE Journal of Oceanic Engineering*, vol. 38, no. 4, pp. 701–717, Oct 2013.

[7] A. Goldsmith, *Wireless Communications*, Cambridge University Press, New York, NY, USA, 2005.

[8] M. Stojanovic and P-P J. Beaujean, *Acoustic Communication*, pp. 359–386, Springer International Publishing, Cham, 2016.

[9] D. Tse and P. Viswanath, *Fundamentals of Wireless Communication*, Cambridge University Press, USA, 2005.

[10] M. Stojanovic and J. Preisig, "Underwater acoustic communication channels: Propagation models and statistical characterization," *IEEE Communications Magazine*, vol. 47, no. 1, pp. 84–89, January 2009.

[11] T. S. Rappaport, *Wireless communications: Principles and practice*, Prentice Hall, 1996.

[12] H. Ghannadrezaii and J. Bousquet, "Maximizing network coverage in a multichannel short-range underwater acoustic sensor network," *Computer Networks*, vol. 160, pp. 1 – 10, 2019.

[13] A. Radosevic, R. Ahmed, T. M. Duman, J. G. Proakis, and M. Stojanovic, "Adaptive ofdm modulation for underwater acoustic communications: Design considerations and experimental results," *IEEE Journal of Oceanic Engineering*, vol. 39, no. 2, pp. 357–370, 2014.

[14] E. Liou, C. Kao, C. Chang, and C. Huang Y. Lin, "Internet of Underwater Things: Challenges and Routing Protocols," in *2018 IEEE International Conference on Applied System Invention (ICASI)*, April 2018, pp. 1171–1174.

[15] T. Melodia D. Pompili and I. F. Akyildiz, "Three-dimensional and two-dimensional deployment analysis for underwater acoustic sensor networks," *Ad Hoc Netw.*, vol. 7, no. 4, pp. 778–790, June 2009.

[16] Y. M. Aval, K. Sarah, and M. Stojanovic, "On the Achievable Rate of a Class of Acoustic Channels and Practical Power Allocation Strategies for OFDM Systems," *IEEE Journal of Oceanic Engineering*, vol. 40, no. 4, pp. 785–795, 2015.

[17] E. Demirors, G. Sklivanitis, T. Melodia, S. N. Batalama, and D. A. Pados, "Software-defined underwater acoustic networks: toward a high-rate real-time reconfigurable modem," *IEEE Communications Magazine*, vol. 53, no. 11, pp. 64–71, 2015.

[18] V. Gazis, E. Patouni, N. Alonistioti, and L. Merakos, "A Survey of Dynamically Adaptable Protocol Stacks," *IEEE Communications Surveys Tutorials*, vol. 12, no. 1, pp. 3–23, First 2010.

[19] W. Quan, N. Cheng, M. Qin, H. Zhang, H. A. Chan, and X. Shen, "Adaptive Transmission Control for Software Defined Vehicular Networks," *IEEE Wireless Communications Letters*, vol. 8, no. 3, pp. 653–656, 2019.

[20] A. M. Jaradat, J. M. Hamamreh, and H. Arslan, "Modulation options for ofdm-based waveforms: Classification, comparison, and future directions," *IEEE Access*, vol. 7, pp. 17263–17278, 2019.

[21] S. Dang, J. P. Coon, and G. Chen, "Adaptive OFDM With Index Modulation for Two-Hop Relay-Assisted Networks," *IEEE Transactions on Wireless Communications*, vol. 17, no. 3, pp. 1923–1936, 2018.

[22] S. Jiang, "State-of-the-Art Medium Access Control (MAC) Protocols for Underwater Acoustic Networks: A Survey Based on a MAC Reference Model," *IEEE Communications Surveys Tutorials*, vol. 20, no. 1, pp. 96–131, Firstquarter 2018.

[23] M. Chitre, "A high-frequency Warm Shallow Water Acoustic Communications Channel Model and Measurements," *The Journal of the Acoustical Society of America*, vol. 122, no. 5, pp. 2580–2586, 2007.

[24] V. Di Valerio, F. Lo Presti, C. Petrioli, L. Picari, D. Spaccini, and S. Basagni, "Carma: Channel-aware reinforcement learning-based multi-path adaptive routing for underwater wireless sensor networks," *IEEE Journal on Selected Areas in Communications*, vol. 37, no. 11, pp. 2634–2647, 2019.

[25] H. Tran-Dang and D-S Kim, "Channel-aware cooperative routing in underwater acoustic sensor networks," *Journal of Communications and Networks*, vol. 21, no. 1, pp. 33–44, 2019.

[26] K. Pelekanakis, R. Petroccia, Y. Fountzoulas, D. Green, S. Fioravanti, J. Alves, S. Blouin, and S. Pecknold, "A simulation study for long-range underwater acoustic networks in the high north," *IEEE Journal of Oceanic Engineering*, vol. 44, no. 4, pp. 850–864, 2019.

[27] S. Basagni, C. Petrioli, R. Petroccia, and D. Spaccini, "Channel-aware routing for underwater wireless networks," in *2012 Oceans - Yeosu*, 2012, pp. 1–9.

[28] M. Shiwen, "Chapter 8 - fundamentals of communication networks," in *Cognitive Radio Communications and Networks*, Alexander M. Wyglinski, Maziar Nekovee, and Y. Thomas Hou, Eds., pp. 201–234. Academic Press, Oxford, 2010.

[29] Z. Zhou, B. Yao, R. Xing, L. Shu, and S. Bu, "E-carp: An energy efficient routing protocol for uwsns in the internet of underwater things," *IEEE Sensors Journal*, vol. 16, no. 11, pp. 4072–4082, 2016.

[30] B. Diao, Y. Xu, Z. An, F. Wang, and C. Li, "Improving both energy and time efficiency of depth-based routing for underwater sensor networks," *Int. J. Distrib. Sen. Netw.*, vol. 2015, jan 2015.

[31] T.S. Rappaport, *Wireless Communications, Principle and Practices*, Prentice Hall, New Jersey, 2002.

[32] Z-Y. Zhang and L-F. Lai, "A novel ofdm transmission scheme with length-adaptive cyclic prefix," *Journal of Zhejiang University-SCIENCE A*, vol. 5, no. 11, pp. 1336–1342, Nov 2004.

[33] F. H. Fisher and V. P. Simmons, "Sound absorption in sea water," *The Journal of the Acoustical Society of America*, vol. 62, no. 3, pp. 558–564, 1977.

[34] F-B. Jensen, W-A. Kuperman, M-B. Porter, and H. Schmidt, *Computational Ocean Acoustics*, Springer Publishing Company, Incorporated, 2nd edition, 2011.

[35] V. Sparrow, K. Poulain, and R. Romond, "The effective sound speed approximation and its implications for en-route propagation," *The Journal of the Acoustical Society of America*, vol. 135, no. 4, pp. 2381–2381, 2014.

[36] R. J. Urick, *Principles of Underwater Sound*, McGraw-Hill New York, [rev. ed.]. edition, 1975.

[37] M. Miron-Morin, *Quantification of the Oceanographic Contributors to Time-Variance in the Underwater Acoustic Channel during the DALCOMMS1 Experiment*, PhD dissertation, Department of Oceanography Dalhousie Univeristy, 2018.

[38] P. Qarabaqi and M. Stojanovic, "Modeling the large scale transmission loss in underwater acoustic channels," in *2011 49th Annual Allerton Conference on Communication, Control, and Computing (Allerton)*, 2011, pp. 445–452.

[39] H. Medwin and C-S. Clay, "Chapter 2 - sound propagation," in *Fundamentals of Acoustical Oceanography*, H. Medwin and C. S. Clay, Eds., Applications of Modern Acoustics, pp. 17 – 69. Academic Press, San Diego, 1998.

[40] W. C. Jakes, *Mobile Radio Systems*, pp. 159–159, Wiley, 1974.

[41] I. Kochanska and J. H. Schmidt, "Estimation of coherence bandwidth for underwater acoustic communication channel," in *2018 Joint Conference - Acoustics*, 2018, pp. 1–5.

[42] R. J. C. Bultitude, "Estimating frequency correlation functions from propagation measurements on fading radio channels: a critical review," *IEEE Journal on Selected Areas in Communications*, vol. 20, no. 6, pp. 1133–1143, 2002.

[43] S. Coatelan and A. Glavieux, "Design and test of a multicarrier transmission system on the shallow water acoustic channel," in *Proceedings of OCEANS'94*, 1994, vol. 3, pp. III/472–III/477 vol.3.

[44] J. A. Rice M. Stojanovic, J. G. Proarkis and M. D. Green, "Spread spectrum underwater acoustic telemetry," in *OCEANS'98. Conference Proceedings*, Sep. 1998, vol. 2, pp. 650–654 vol.2.

[45] R. Fan, C. McGoldrick, and M. Gerla, "An sdn architecture for under water search and surveillance," in *2017 13th Annual Conference on Wireless On-demand Network Systems and Services (WONS)*, 2017, pp. 96–99.

[46] E. Isufi, H. Dol, and G. Leus, "Advanced Flooding-Based Routing Protocols for Underwater Sensor Networks," *EURASIP Journal on Advances in Signal Processing*, vol. 2016, no. 1, pp. 52, 2016.

[47] J. Schiller, *Mobile Communications*, Addison-Wesley Longman Publishing Co., Inc., USA, 1999.

[48] W. B. Yang and T. C. Yang, "High frequency fhfsk underwater acoustic communications: The environmental effect and signal processing," *AIP Conference Proceedings*, vol. 728, no. 1, pp. 106–113, 2004.

[49] M. Stojanovic, J.A. Catipovic, and J.G. Proakis, "Phase-coherent digital communications for underwater acoustic channels," *IEEE Journal of Oceanic Engineering*, vol. 19, no. 1, pp. 100–111, 1994.

[50] K. Pelekanakis and M. Chitre, "A channel-estimate-based decision feedback equalizer robust under impulsive noise," in *2014 Underwater Communications and Networking (UComms)*, 2014, pp. 1–5.

[51] L. Freitag, M. Johnson, and M. Stojanovic, "Efficient equalizer update algorithms for acoustic communication channels of varying complexity," in *Oceans '97. MTS/IEEE Conference Proceedings*, 1997, vol. 1, pp. 580–585 vol.1.

[52] J. Wen, S-H. Lee, G-R. Lee, and J-T. Chang, "Timing and delay spread estimation scheme in ofdm systems," *IEEE Transactions on Consumer Electronics*, vol. 54, no. 2, pp. 316–320, 2008.

[53] B. Li, J. Huang, S. Zhou, K. Ball, M. Stojanovic, L. Freitag, and P. Willett, "MIMO-OFDM for High-Rate Underwater Acoustic Communications," *IEEE Journal of Oceanic Engineering*, vol. 34, no. 4, pp. 634–644, 2009.

[54] W. Li and J. C. Preisig, "Estimation of rapidly time-varying sparse channels," *IEEE Journal of Oceanic Engineering*, vol. 32, no. 4, pp. 927–939, 2007.

[55] Y. Zhang, R. Venkatesan, O. A. Dobre, and C. Li, "Efficient Estimation and Prediction for Sparse Time-Varying Underwater Acoustic Channels," *IEEE Journal of Oceanic Engineering*, vol. 45, no. 3, pp. 1112–1125, 2020.

[56] A. Tadayon and M. Stojanovic, "Low-complexity superresolution frequency offset estimation for high data rate acoustic ofdm systems," *IEEE Journal of Oceanic Engineering*, vol. 44, no. 4, pp. 932–942, 2019.

[57] J. M. Jornet, M. Stojanovic, and M. Zorzi, "On joint frequency and power allocation in a cross-layer protocol for underwater acoustic networks," *IEEE Journal of Oceanic Engineering*, vol. 35, no. 4, pp. 936–947, 2010.

[58] P. Ceballos Carrascosa and M. Stojanovic, "Adaptive channel estimation and data detection for underwater acoustic mimo–ofdm systems," *IEEE Journal of Oceanic Engineering*, vol. 35, no. 3, pp. 635–646, 2010.

[59] H. S. Dol, P. Casari, T. van der Zwan, and R. Otnes, "Software-defined underwater acoustic modems: Historical review and the nilus approach," *IEEE Journal of Oceanic Engineering*, vol. 42, no. 3, pp. 722–737, July 2017.

[60] F. Berning, T. Radtke, S. Rautenberg, M. Motz, and I. Nissen, "A realization of the software defined radio concept in an underwater communication modem," in *2014 Underwater Communications and Networking (UComms)*, Sep. 2014, pp. 1–5.

[61] S. Mangione, G. E. Galioto, D. Croce, I. Tinnirello, and C. Petrioli, "A channel-aware adaptive modem for underwater acoustic communications," *IEEE Access*, vol. 9, pp. 76340–76353, 2021.

[62] J. Potter, J. Alves, D. Green, G. Zappa, I. Nissen, and K. McCoy, "The JANUS Underwater Communications Standard," in *2014 Underwater Communications and Networking (UComms)*, Sep. 2014, pp. 1–4.

[63] J. Alves, T. Furfaro, K. LePage, K. Pelekanakis A. Munafò, R. Petroccia, and G. Zappa, "Moving janus forward: A look into the future of underwater communications interoperability," in *OCEANS 2016 MTS/IEEE Monterey*, Sep. 2016, pp. 1–6.

[64] D. Green, "Establishing A Standard For Underwater Digital Acoustic Communications and Networks," in *Proceedings of the 10th International Conference on Underwater Networks & Systems*, New York, NY, USA, 2015, WUWNET '15, pp. 20:1–20:5, ACM.

[65] L. Zhiqiang, X. Yan, and G. B. Giannakis, "Space-time-frequency coded OFDM over frequency-selective fading channels," *IEEE Transactions on Signal Processing*, vol. 50, no. 10, pp. 2465–2476, 2002.

[66] Y. M. Aval and M. Stojanovic, "A method for differentially coherent multichannel processing of acoustic OFDM signals," in *2012 IEEE 7th Sensor Array and Multichannel Signal Processing Workshop (SAM)*, 2012, pp. 73–76.

[67] K. Pelekanakis, R. Petroccia, Y. Fountzoulas, D. Green, S. Fioravanti, J. Alves, S. Blouin, and S. Pecknold, "A simulation study for long-range underwater acoustic networks in the high north," *IEEE Journal of Oceanic Engineering*, vol. 44, no. 4, pp. 850–864, Oct 2019.

[68] S. Basagni, C. Petrioli, R. Petroccia, and M. Stojanovic, "Choosing the packet size in multi-hop underwater networks," in *OCEANS'10 IEEE SYDNEY*, May 2010, pp. 1–9.

[69] E. M. Sozer, M. Stojanovic, and J. G. Proakis, "Underwater Acoustic Networks," *IEEE Journal of Oceanic Engineering*, vol. 25, no. 1, pp. 72–83, Jan 2000.

[70] Y. Li, Y. Zhang, H. Zhou, and T. Jiang, "To Relay or Not to Relay: Open Distance and Optimal Deployment for Linear Underwater Acoustic Networks," *IEEE Transactions on Communications*, vol. 66, no. 9, pp. 3797–3808, 2018.

[71] M. K. Park and V. Rodoplu, "Uwan-mac: An energy-efficient mac protocol for underwater acoustic wireless sensor networks," *IEEE Journal of Oceanic Engineering*, vol. 32, no. 3, pp. 710–720, 2007.

[72] K. Chen, M. Ma, E. Cheng, F. Yuan, and W. Su, "A survey on mac protocols for underwater wireless sensor networks," *IEEE Communications Surveys and Tutorials*, vol. 16, no. 3, pp. 1433–1447, 2014.

[73] P. Mandal and S. De, "New reservation multiaccess protocols for underwater wireless ad hoc sensor networks," *IEEE Journal of Oceanic Engineering*, vol. 40, no. 2, pp. 277–291, 2015.

[74] K. Chen, M. Ma, E. Cheng, F. Yuan, and W. Su, "A survey on mac protocols for underwater wireless sensor networks," *IEEE Communications Surveys and Tutorials*, vol. 16, no. 3, pp. 1433–1447, 2014.

[75] N. Chirdchoo, W.-S. Soh, and K. C. Chua, "Aloha-based mac protocols with collision avoidance for underwater acoustic networks," in *IEEE INFOCOM 2007 - 26th IEEE International Conference on Computer Communications*, 2007, pp. 2271–2275.

[76] W. Huang, M. Liu, and S. Zhang, "Sfama-mm: A slotted fama based mac protocol for multi-hop underwater acoustic networks with a multiple reception mechanism," in *2018 37th Chinese Control Conference (CCC)*, 2018, pp. 7315–7321.

[77] L. Qian, Senlin Zhang, M. Liu, and Q. Zhang, "A maca-based power control mac protocol for underwater wireless sensor networks," in *2016 IEEE/OES China Ocean Acoustics (COA)*, 2016, pp. 1–8.

[78] W. Lin, D. Li, J. Chen, T. Sun, and T. Wang, "A Wave-like Amendment-based Time-division Medium Access Slot Allocation Mechanism for Underwater Acoustic Sensor Networks," in *2009 International Conference on Cyber-Enabled Distributed Computing and Knowledge Discovery*, 2009, pp. 369–374.

[79] J. Mao, S. Chen, Y. Liu, J. Yu, and Y. Xu, "LT-MAC: A location-based TDMA MAC Protocol for Small-scale Underwater Sensor Networks," in *2015 IEEE International Conference on Cyber Technology in Automation, Control, and Intelligent Systems (CYBER)*, 2015, pp. 1275–1280.

[80] N. Morozs, P. Mitchell, and Y. V. Zakharov, "TDA-MAC: TDMA Without Clock Synchronization in Underwater Acoustic Networks," *IEEE Access*, vol. 6, pp. 1091–1108, 2018.

[81] T. Melodia, H. Kulhandjian, L-C. Kuo, and E. Demirors, *Advances in Underwater Acoustic Networking*, chapter 23, pp. 804–852, John Wiley and Sons, Ltd, 2013.

[82] M. Rahmati, R. Petroccia, and D. Pompili, "In-Network Collaboration for CDMA-Based Reliable Underwater Acoustic Communications," *IEEE Journal of Oceanic Engineering*, vol. 44, no. 4, pp. 881–894, 2019.

[83] H. Doukkali, S. Houcke, and L. Nuaymi, "A Cross Layer Approach with CSMA/CA based Protocol and CDMA Transmission for Underwater Acoustic Networks," in *2007 IEEE 18th International Symposium on Personal, Indoor and Mobile Radio Communications*, 2007, pp. 1–5.

[84] Y. Su, R. Fan, Z. Jin, and X. Fu, "Design of an OFDMA-Based MAC Protocol for an Underwater Glider Network With Motion Prediction," *IEEE Access*, vol. 6, pp. 62655–62663, 2018.

[85] E. M. Sozer, M. Stojanovic, and J. G. Proakis, "Underwater acoustic networks," *IEEE Journal of Oceanic Engineering*, vol. 25, no. 1, pp. 72–83, 2000.

[86] R. Petroccia S. Basagni, C. Petrioli and D. Spaccini, "Channel Replay-Based Performance Evaluation of Protocols for Underwater Routing," in *2014 Oceans - St. John's*, Sept 2014, pp. 1–7.

[87] Y. Su, Z. Zhou, Z. Jin, and Q. Yang, "A Joint Relay Selection and Power Allocation MAC Protocol for Underwater Acoustic Sensor Network," *IEEE Access*, vol. 8, pp. 65197–65210, 2020.

[88] R. Petroccia S. Basagni, P. Chiara and D. Spaccini, "CARP: A Channel-Aware Routing Protocol for Underwater Acoustic Wireless Networks," *Ad Hoc Networks*, vol. 34, pp. 92–104, 2015.

[89] M. Zhang and W. Cai, "Energy-efficient depth based probabilistic routing within 2-hop neighborhood for underwater sensor networks," *IEEE Sensors Letters*, vol. 4, no. 6, pp. 1–4, 2020.

[90] W. Yu, Y. Chen, L. Wan, X. Zhang, P. Zhu, and X. Xu, "An Energy Optimization Clustering Scheme for Multi-Hop Underwater Acoustic Cooperative Sensor Networks," *IEEE Access*, vol. 8, pp. 89171–89184, 2020.

[91] S. Basagni, V. Di Valerio, P. Gjanci, and C. Petrioli, "Finding marlin: Exploiting multi-modal communications for reliable and low-latency underwater networking," in *IEEE INFOCOM 2017 - IEEE Conference on Computer Communications*, May 2017, pp. 1–9.

[92] Y. Su, R. Fan, X. Fu, and Z. Jin, "DQELR: An Adaptive Deep Q-Network-Based Energy- and Latency-Aware Routing Protocol Design for Underwater Acoustic Sensor Networks," *IEEE Access*, vol. 7, pp. 9091–9104, 2019.

[93] A. Viterbi, "Convolutional Codes and Their Performance in Communication Systems," *IEEE Transactions on Communication Technology*, vol. 19, no. 5, pp. 751–772, October 1971.

[94] J. Heidemann, , J. Wills, and A. Syed, "Research challenges and applications for underwater sensor networking," in *IEEE WCNC 2006.*, April 2006, vol. 1, pp. 228–235.

[95] R. W. L. Coutinho, A. Boukerche, L. F. M. Vieira, and A. A. F. Loureiro, "Geographic and Opportunistic Routing for Underwater Sensor Networks," *IEEE Transactions on Computers*, vol. 65, no. 2, pp. 548–561, Feb 2016.

[96] M. E. Renda F. Librino and P. Santi, "Evaluating Multi-Hop Beaconing Forwarding Strategies for IEEE 802.11p Vehicular Networks," in *2013 IEEE Vehicular Networking Conference*, Dec 2013, pp. 31–38.

[97] M. Stojanovic J. M. Jornet and M. Zorzi, "Focused Beam Routing Protocol for Underwater Acoustic Networks," in *Proceedings of the Third ACM International Workshop on Underwater Networks*, New York, NY, USA, 2008, WuWNeT '08, pp. 75–82, ACM.

[98] S. Basagni, C. Petrioli, R. Petroccia, and M. Stojanovic, "Choosing the packet size in multi-hop underwater networks," in *OCEANS'10 IEEE SYDNEY*, 2010, pp. 1–9.

[99] S. Yun, Y. Yi, J. Shin, and D. Y. Eun, "Optimal csma: A survey," in *2012 IEEE International Conference on Communication Systems (ICCS)*, Nov 2012, pp. 199–204.

[100] N. Syed, P. Meher, and A. P. Vinod, "Efficient cross-correlation algorithm and architecture for robust synchronization in frame-based communication systems," *Circuits, Systems, and Signal Processing*, vol. 37, no. 6, pp. 2548–2573, Jun 2018.

[101] W. Wang and X. Liu, "List-coloring Based Channel Allocation for Open-spectrum Wireless Networks," in *VTC-2005-Fall. 2005 IEEE 62nd Vehicular Technology Conference, 2005.*, Sept 2005, vol. 1, pp. 690–694.

[102] A. A. Syed, W. Ye, and J. Heidemann, "T-Lohi: A New Class of MAC Protocols for Underwater Acoustic Sensor Networks," in *IEEE INFOCOM 2008 - The 27th Conference on Computer Communications*, April 2008, pp. 789–797.

[103] A. A. Syed, J. Heidemann, and W. Ye, "Tones for real: Managing multipath in underwater acoustic wakeup," in *2010 7th Annual IEEE Communications Society Conference on Sensor, Mesh and Ad Hoc Communications and Networks (SECON)*, June 2010, pp. 1–3.

[104] Y-C. Tseng S-L. Wu, C-Y. Lin and J-L. Sheu, "A new multi-channel mac protocol with on-demand channel assignment for multi-hop mobile ad hoc networks," in *Proceedings International Symposium on Parallel Architectures, Algorithms and Networks. I-SPAN 2000*, 2000, pp. 232–237.

[105] T. Chen, H. Zhang, G. M. Maggio, and I. Chlamtac, "CogMesh: A Cluster-Based Cognitive Radio Network," in *2007 2nd IEEE International Symposium on New Frontiers in Dynamic Spectrum Access Networks*, April 2007, pp. 168–178.

[106] W. B. Yang and T. C. Yang, "High-frequency channel characterization for M-ary frequency-shift-keying underwater acoustic communications," *The Journal of the Acoustical Society of America*, vol. 120, no. 5, pp. 2615–2626, 2006.

[107] X. Cheng, L. Yang, and X. Cheng, "Cognitive spectrum access for underwater acoustic communications," in *Cooperative OFDM Underwater Acoustic Communications*. 2016, pp. 13–16, Springer International Publishing.

[108] A. Song Y. Zhou and F. Tong, "Underwater acoustic channel characteristics and communication performance at 85 kHz," *The Journal of the Acoustical Society of America*, vol. 142, no. 4, pp. EL350–EL355, 2017.

[109] P. A. van Walree, F. Socheleau, R. Otnes, and T. Jenserud, "The Watermark Benchmark for Underwater Acoustic Modulation Schemes," *IEEE Journal of Oceanic Engineering*, vol. 42, no. 4, pp. 1007–1018, Oct 2017.

[110] S. Zhou B. Li, M. Stojanovic, L. Freitag, and P. Willett, "Multicarrier Communication Over Underwater Acoustic Channels With Nonuniform Doppler Shifts," *IEEE Journal of Oceanic Engineering*, vol. 33, no. 2, pp. 198–209, April 2008.

[111] C. Cordeiro and K. Challapali, "C-MAC: A Cognitive MAC Protocol for Multi-Channel Wireless Networks," in *2007 2nd IEEE International Symposium on New Frontiers in Dynamic Spectrum Access Networks*, April 2007, pp. 147–157.

[112] Z. Zhou, Z. Peng, J. H. Cui, and Z. Jiang, "Handling Triple Hidden Terminal Problems for Multichannel MAC in Long-Delay Underwater Sensor Networks," *IEEE Transactions on Mobile Computing*, vol. 11, no. 1, pp. 139–154, Jan 2012.

[113] L. Cao and H. Zheng, "Distributed Rule-Regulated Spectrum Sharing," *IEEE Journal on Selected Areas in Communications*, vol. 26, no. 1, pp. 130–145, Jan 2008.

[114] D. M. Carmen, "A Topology Reorganization Scheme for Reliable Communication in Underwater Wireless Sensor Networks Affected by Shadow Zones," *Sensors*, vol. 9, no. 11, pp. 8684–8708, 2009.

[115] C-F. Cheang Q. Wang, H-N. Dai and H. Wang, "Link Connectivity and Coverage of Underwater Cognitive Acoustic Networks under Spectrum Constraint," *Sensors*, vol. 17, no. 12, 2017.

[116] G. Zhang and S. Feng, "Subcarrier allocation algorithms based on graph-coloring in Cognitive Radio NC-OFDM system," in *2010 3rd International Conference on Computer Science and Information Technology*, July 2010, vol. 2, pp. 535–540.

[117] J. Huang, S. Zhou, C. R. Berger, and P. Willett, "Progressive Inter-Carrier Interference Equalization for OFDM Transmission Over Time-Varying Underwater Acoustic Channels," *IEEE Journal of Selected Topics in Signal Processing*, vol. 5, no. 8, pp. 1524–1536, 2011.

[118] Ba. Li, S. Zhou, M. Stojanovic, L. Freitag, and P. Willett, "Multicarrier communication over underwater acoustic channels with nonuniform doppler shifts," *IEEE Journal of Oceanic Engineering*, vol. 33, no. 2, pp. 198–209, 2008.

[119] G.D. Egbert and S.Y. Erofeeva, "Efficient inverse modeling of barotropic ocean tides," *Journal of Atmospheric and Oceanic Technology*, vol. 19, no. 2, pp. 183–204, 2002.

[120] E. A. Karjadi, M. Badiey, J. T. Kirby, and C. Bayindir, "The Effects of Surface Gravity Waves on High-Frequency Acoustic Propagation in Shallow Water," *IEEE Journal of Oceanic Engineering*, vol. 37, no. 1, pp. 112–121, 2012.

[121] M. Wimbush, C. S. Cox, and A. J. Clarke, ," in *Ocean waves*. 2022/3/30/ 2021, McGraw-Hill Education.

[122] M.S. Longuet-Higgins, "On the Statistical Distribution of the Heights of Sea Waves," *Journal of Marine Research*, vol. 11, no. 2, pp. 245–266, 1952.

[123] E. Baktash, M. J. Dehghani, M. R. Farjadi, and M. R. Karimi, "Shallow Water Acoustic Channel Modeling Based on Analytical Second Order Statistics for Moving Transmitter/Receiver," *IEEE Transactions on Signal Processing*, vol. 63, no. 10, pp. 2533–2545, 2015.

[124] S. O. Rice, "Reflection of Electromagnetic Waves from Slightly Rough Surfaces," *Communications on Pure and Applied Mathematics*, vol. 4, no. 2-3, pp. 351–378, 1951.

[125] E. Y. Harper and F. M. Labianca, "Perturbation Theory for Scattering of Sound From a Point Source by a Moving Rough Surface in the Presence of Refraction," *The Journal of the Acoustical Society of America*, vol. 57, no. 5, pp. 1044–1051, 1975.

[126] E. I. Thorsos, "The Validity of the Kirchhoff Approximation for Rough Surface Scattering Using a Gaussian Roughness Spectrum," *The Journal of the Acoustical Society of America*, vol. 83, no. 1, pp. 78–92, 1988.

[127] J-A. Holzer and C. Sung, "Scattering of Electromagnetic Waves from a Rough Surface. II," *Journal of Applied Physics*, vol. 49, no. 3, pp. 1002–1011, 1978.

[128] I. Nissen and Kochańska , "Stationary Underwater Channel Experiment: Acoustic Measurements and Characteristics in the Bornholm Area for Model Validations," *HYDROACOUSTICS*, 2016.

[129] C.W. Helstrom, "Distribution of the envelope of a sum of random sine waves and Gaussian noise," *IEEE Transactions on Aerospace and Electronic Systems*, vol. 35, no. 2, pp. 594–601, 1999.

[130] J. Kim, I. Koh, and Y. Lee, "Short-term Fading Model for Signals Reflected by Ocean Surfaces in Underwater Acoustic Communication," *IET Communications*, vol. 9, no. 9, pp. 1147–1153, 2015.

[131] D. Lemons and P. Langevin, *An introduction to stochastic processes in physics*, John Hopkins University Press, 2002.

[132] D. F. McCammon and S. T. McDaniel, *Rough Surface Scattering and the Kirchhoff Approximation*, pp. 51–55, Springer US, Boston, MA, 1987.

[133] M. Werman and D. Keren, "A bayesian method for fitting parametric and nonparametric models to noisy data," *IEEE Transactions on Pattern Analysis and Machine Intelligence*, vol. 23, no. 5, pp. 528–534, 2001.

[134] S.B Martin, J. MacDonald, C.C. Wilson, Z. Wallot-Beale, H. Ghannadrezaii, D.R. Barclay, J.F. Bouquet, E.E. Maxner, C.B. Lawrence, and L. Muzi, "How does and sound travel in high-energy environments? effectiveness of acoustic monitoring systems and turbine audibility assessment:," *2018 OERA Grand Passage Acoustic Monitoring Final Report.*, vol. Version 1.1, no. Document 02243, 2020.

[135] S. Theodoridis, "Chapter 3 - learning in parametric modeling: Basic concepts and directions," in *Machine Learning (Second Edition)*, S. Theodoridis, Ed., pp. 67–120. Academic Press, second edition edition, 2020.

[136] K. Pahlavan and P. Krishnamurthy, *Networking Fundamentals: Wide, Local and Personal Area Communications*, Wiley, 2009.

[137] T. Kanungo, D.M. Mount, N.S. Netanyahu, C.D. Piatko, R. Silverman, and A.Y. Wu, "An efficient k-means clustering algorithm: analysis and implementation," *IEEE Transactions on Pattern Analysis and Machine Intelligence*, vol. 24, no. 7, pp. 881–892, 2002.

[138] Mathworks, "Create probability distribution object," 2022 (accessed April 29, 2022), https://www.mathworks.com/help/stats/makedist.html.

[139] I. Trigui, A. Laourine, S. Affes, and A. Stephenne, "The inverse gaussian distribution in wireless channels: Second-order statistics and channel capacity," *IEEE Transactions on Communications*, vol. 60, no. 11, pp. 3167–3173, 2012.

[140] J. Blumenstein, A. Prokes, A. Chandra, T. Mikulasek, R. Marsalek, T. Zemen, and C. Mecklenbräuker, "In-vehicle channel measurement, characterization, and spatial consistency comparison of 30–11 GHz and 55–65 GHz frequency bands," *IEEE Transactions on Vehicular Technology*, vol. 66, no. 5, pp. 3526–3537, 2017.

[141] National Oceanography Centre Marine Data Products, ," in *An Introduction to Tidal Numerical Modelling*, 2017.

[142] F. Lindgren, H. Rue, and J. Lindstram, "An Explicit Link Between Gaussian Fields and Gaussian Markov Random Fields: The Stochastic Partial Differential Equation Approach," *Journal of the Royal Statistical Society: Series B (Statistical Methodology)*, vol. 73, no. 4, pp. 423–498, 2011.

[143] B. Rajagopalan, P. Van Dusen, and C. Bracken, "A Nonstationary Hidden Markov Model with Generalized Extreme Value Distributions to Model Streamflow Extremes," in *AGU Fall Meeting Abstracts*, Dec. 2018, vol. 2018, pp. NH31B–0980.

[144] Y. Zhang, R. Venkatesan, O. A. Dobre, and C. Li, "Efficient Estimation and Prediction for Sparse Time-Varying Underwater Acoustic Channels," *IEEE Journal of Oceanic Engineering*, vol. 45, no. 3, pp. 1112–1125, 2020.

[145] L. Liu, L. Cai, L. Ma, and G. Qiao, "Channel State Information Prediction for Adaptive Underwater Acoustic Downlink OFDMA System: Deep Neural Networks Based Approach," *IEEE Transactions on Vehicular Technology*, vol. 70, no. 9, pp. 9063–9076, 2021.

[146] E. N. Gilbert, "Capacity of a burst-noise channel," *The Bell System Technical Journal*, vol. 39, no. 5, pp. 1253–1265, 1960.

[147] S. W. Hong and N. Moayeri, "Finite-state Markov channel-a useful model for radio communication channels," *IEEE Transactions on Vehicular Technology*, vol. 44, no. 1, pp. 163–171, 1995.

[148] W. Sun and Z. Wang, "Modeling and prediction of large-scale temporal variation in underwater acoustic channels," in *OCEANS 2016 - Shanghai*, April 2016, pp. 1–6.

[149] W. Turin and R. Van Nobelen, "Hidden Markov modeling of fading channels," in *VTC '98. 48th IEEE Vehicular Technology Conference. Pathway to Global Wireless Revolution (Cat. No.98CH36151)*, 1998, vol. 2, pp. 1234–1238 vol.2.

[150] H. Kulhandjian and T Melodia, *Modeling Underwater Acoustic Channels in Short-Range Shallow Water Environments*, WUWNET '14. Association for Computing Machinery, New York, NY, USA, 2014.

[151] R Serfozo, *Basics of applied stochastic processes*, Springer Science & Business Media, 2009.

[152] F. Pignieri, F. De Rango, F. Veltri, and S. Marano, "Markovian approach to model underwater acoustic channel: Techniques comparison," in *MILCOM 2008 - 2008 IEEE Military Communications Conference*, 2008, pp. 1–7.

[153] S. M. Ross, *Stochastic processes*, John Wiley and Sons, 1996.

[154] A. Dobbin and J. F. Bousquet, "Reliable acoustic link using non-coherent turbo-coded frequency shift keying," in *WUWNET'17 Proceedings of the International Conference on Underwater Networks & Systems*, New York, NY, USA, 2017, pp. 6:1–6:2, ACM.

[155] R. B. Wynn, V. Huvenne, T. P. Le Bas, B. J. Murton, D. P. Connelly, B. J. Bett, H. A. Ruhl, Morris K. J., J. Peakall, D. R. Parsons, Sumner E. J., Darby S. E., Dorrell R. M., and J. E. Hunt, "Autonomous underwater vehicles (auvs): Their past, present and future contributions to the advancement of marine geoscience," *Marine Geology*, vol. 352, pp. 451–468, 2014, 50th Anniversary Special Issue.

[156] Y. M. Aval and M. Stojanovic, "Differentially coherent multichannel detection of acoustic ofdm signals," *IEEE Journal of Oceanic Engineering*, vol. 40, no. 2, pp. 251–268, 2015.